

AMPLITUDE-PRESERVING MIGRATION AND ITS APPLICATION TO IMAGING  
OF A BSR IN MARINE MULTICHANNEL SEISMIC REFLECTION DATA

Dissertation

zur Erlangung des Doktorgrades  
der Mathematisch-Naturwissenschaftlichen Fakultät  
der Christian-Albrechts-Universität  
zu Kiel

vorgelegt von  
Abd Haris

Kiel 2002

Referent: Prof. Dr. Ernst Flueh  
Korreferent: Prof. Dr. Wolfgang Rabbel  
Tag der mündlichen Prüfung: 17.12.2002  
Zum Druck genehmigt: Kiel, den

Der Dekan



## ABSTRACT

Amplitude-Preserving (AP) migration method has been developed to obtain structural image and to estimate angle-dependent reflectivity information from surface seismic reflection data, which is the basis to perform Amplitude Versus Angle (AVA) analysis. The strategy of the AP migration method is based on combining a Common Focus Point (CFP) technique for removing wave field propagation effects and an application of a weight function for preserving amplitudes during the migration process.

In most currently existing migration programs, the seismic modeling and the seismic migration are compiled in hard link and thus designed in one package. As a consequence, the focusing operators are unique and depend on which modeling algorithm is employed. In view of the flexibility in accommodating any kind of focusing operators (single-valued or multi-valued operators), which can be obtained from the existing modeling algorithms (e.g., finite difference, ray-tracing, etc.), the AP migration is designed as a separate program from modeling algorithms by requiring migration operators in the form of seismograms as so-called seismogram operators. Thus, no explicit traveltimes information is required. All required quantities (e.g., traveltimes, amplitude, phase and angle) for the amplitude preserving weight function are estimated directly from seismogram operators. With regards to the realistic modeling, the Nichols' method so-called the band limited Green's function, which computes traveltimes, amplitude and phase, has been chosen and modified to generate multi-valued focusing operators. The modeling method works in the seismic frequency range rather than in a high frequency approximation. A few number of frequencies in the seismic frequency band are propagated outward from the source location in polar coordinates.

First applications to simple models are used to verify the developed method and to visualize its subsequent steps and performance. Migration examples on the Marmousi model demonstrate its potential to image the complex model. The flexibility of the migration method further permits an expansion of the application field for special data acquisition and configuration, e.g., ocean bottom hydrophones, which cannot be incorporated in the standard processing schemes. As an application to a real data set, the AP migration is applied to marine MCS reflection data collected across the continental margin offshore

Oregon (line OR89-02). These data reveal hydrate distribution through the presence of bottom simulating reflectors (BSRs). BSRs, which are commonly interpreted as proof for the boundary surface between hydrate-bearing sediment and the gas-bearing sediment located beneath, are imaged to recover angle-dependent reflectivity gathers as well as structural image. Furthermore, angle-dependent reflectivity gathers are used to examine the local BSR AVA response by performing AVA inversion to provide the primary and the secondary AVA attributes as well as AVA modeling.

## ZUSAMMENFASSUNG

Eine amplitudenerhaltende (Amplitude Preserving, AP) Migrationsmethode wurde entwickelt, um Informationen ueber die Untergrundstruktur und die winkelabhaengige Reflektivitaet aus seismischen Reflexionsdaten zu erhalten. Diese bilden die Grundlage der Amplitude Versus Angle (AVA) Analyse. Die Strategie der AP Migration beruht auf einer Kombination der Common Focus Point (CFP) Technik zur Entfernung von Effekten der Wellenfeldausbreitung und der Anwendung einer Gewichtsfunktion, um die Amplituden waehrend der Migration zu erhalten.

In den meisten gegenwaertig existierenden Migrationsprogrammen sind die seismische Modellierung und die Migration fest miteinander verknuepft und deshalb in einem Programmpaket zusammengefasst. Als Konsequenz gibt es nur einen Abbildungsoperator, der von der Wahl des Modellierungsalgorithmus abhaengt. In Hinblick auf eine flexible Anpassung verschiedener Abbildungsoperatoren (ein- oder mehrwertige Operatoren), welche von existierenden Modellierungsalgorithmen erzeugt werden koennen (z.B. Finite Differenzen, Ray-tracing etc.), ist die AP Migration ein eigenstaendiges Programm, das unabhaengig vom Modellierungsalgorithmus ist und die Migrationsoperatoren in Form von Seismogrammen als sogenannte Seismogrammoperatoren benoetigt. Daher wird keine explizite Laufzeiteninformation benoetigt. Alle notwendigen Werte (z.B. Laufzeit, Amplitude, Phase und Winkel) fuer die amplitudenerhaltende Gewichtsfunktion werden direkt vom Seismogrammoperator bestimmt. Im Hinblick auf eine realistische Modellierung wurde die Nichols Methode, die sogenannte bandlimitierte Green's Funktion, zur Berechnung der Laufzeit, Amplitude und Phase ausgewaehlt und zur Erzeugung von Abbildungsoperators mit Mehrfacheinsaetzen modifiziert. Die Modellierungsmethode arbeitet im seismischen Frequenzbereich in Gegensatz zur Hochfrequenzapproximation. Von der Quellposition wird eine Wellenfartsetzung in Polarkoordinaten fuer wenige diskrete Frequenzen aus dem seismischen frequenzbereich durchgefuehrt

Zunaechst werden Anwendungen auf einfache Modelle vorgestellt, um die entwickelte Methode zu verifizieren und die reale Umsetzung zu visualisieren. Das Abbildungspotential fuer komplexe Modelle wird am Beispiel des Marmousi-Modells demonstriert. Weiterhin erlaubt die Flexibilitaet der Migrationsmethode eine Ausdehnung des Anwendungsbere-

ichs auf spezielle Akquisitionskonfigurationen wie z.B. Ozeanboden-Hydrophone, die nicht in herkömmliche Processingroutinen implementiert werden können. Ein mariner MCS-Reflexionsdatensatz, dessen Daten über dem Kontinentalrand vor der Küste Oregons (Profil OR89-02) gewonnen wurden, dient als Beispiel für eine Anwendung auf Realdaten. Die Analyse der entlang des Profils registrierten bodensimulierenden Reflektoren (BSRs), die als Grenzfläche zwischen Gashydrat und Gas enthaltendem Sediment interpretiert werden, ermöglicht Aussagen über die Hydratverteilung in der Region. Mit der vorgestellten Methode werden die BSRs abgebildet, um sowohl winkelabhängige Reflektivitätswerte zu bestimmen als auch ein strukturelles Bild des Untergrundes zu erhalten. Die erhaltenen winkelabhängigen Reflektivitäten dienen der Untersuchung des lokalen AVA-Verhaltens am BSR mittels einer AVA-Inversion, aus der sich primäre und sekundäre AVA-Attribute und eine AVA-Modellierung ergeben.

# Contents

<b>1</b>	<b>Introduction</b>	<b>1</b>
1.1	The Seismic Method . . . . .	1
1.2	Bottom Simulating Reflector (BSR) . . . . .	2
1.3	Amplitude-Preserving Prestack Depth Migration . . . . .	3
1.4	Outline . . . . .	6
<b>2</b>	<b>Modeling of Focusing Operators Using Band-Limited Green's Function</b>	<b>8</b>
2.1	Introduction . . . . .	8
2.2	A Parametric Model of the Green's Function . . . . .	9
2.3	Single-Arrival Model . . . . .	10
2.3.1	Non-Dispersive Single-Arrival Model . . . . .	10
2.3.2	Dispersive Single-Arrival Model . . . . .	11
2.4	Multi-Arrivals Model . . . . .	12
2.4.1	Arrival Identification . . . . .	13
2.4.2	Arrival Estimation . . . . .	15
2.5	Numerical Examples . . . . .	16
2.5.1	Focusing Operator in a Constant Velocity Model . . . . .	17
2.5.2	Focusing Operator in a Two-Layer Velocity Model with a Horizontal Reflector . . . . .	19
2.5.3	Focusing Operator in a Two-Layer Velocity Model With a Dipping Reflector . . . . .	21
2.5.4	Focusing Operator in Blob Velocity Model . . . . .	23
<b>3</b>	<b>CFP - Amplitude-Preserving Prestack Depth Migration</b>	<b>27</b>



3.1	Introduction . . . . .	27
3.2	Prestack Migration in Terms of Double Focusing . . . . .	29
3.3	Equal Traveltime Principle . . . . .	30
3.4	Forward Model of Primary Reflections . . . . .	31
3.5	Principle of Amplitude-Preserving Migration . . . . .	34
3.5.1	First Focusing Step . . . . .	35
3.5.2	Second Focusing Step . . . . .	36
3.5.3	Amplitude-Preserving Weight Functions . . . . .	37
3.6	General Scheme of the AP Migration . . . . .	39
<b>4</b>	<b>Application of the AP Migration to Synthetic Data</b>	<b>42</b>
4.1	Introduction . . . . .	42
4.2	Marine MCS Synthetic Data . . . . .	43
4.2.1	Velocity Model . . . . .	43
4.2.2	Focusing Operator . . . . .	45
4.2.3	First Focusing Step . . . . .	46
4.2.4	Second Focusing Step . . . . .	47
4.2.4.1	Bifocal Version . . . . .	47
4.2.4.2	Angle-Dependent Reflectivity . . . . .	48
4.2.4.3	Confocal Version . . . . .	53
4.3	Effect of Wavelet Frequency on the Migrated Image . . . . .	53
4.4	OBH Synthetic Data . . . . .	58
4.4.1	Velocity Model . . . . .	59
4.4.2	Migrated OBH Synthetic Data . . . . .	60
4.5	Marmousi Synthetic Data . . . . .	65
4.5.1	Migrated Marmousi Synthetic Data . . . . .	68
<b>5</b>	<b>Application of the AP Migration to Real Seismic Data</b>	<b>77</b>
5.1	Introduction . . . . .	77
5.2	Oregon Seismic Line OR89-02 . . . . .	78
5.2.1	Preprocessing . . . . .	79

5.3	Migration Results . . . . .	80
5.3.1	Structural Image . . . . .	81
5.3.2	Comparison to Other Migration Methods . . . . .	84
5.3.3	Angle-Dependent Reflectivity Gathers . . . . .	87
5.4	AVA Attributes . . . . .	93
5.5	AVA Modeling . . . . .	97
<b>6</b>	<b>Conclusions and Perspectives</b>	<b>107</b>
6.1	Strategy of the AP Migration . . . . .	107
6.2	Focusing Operator . . . . .	109
6.3	Problems and Limitations . . . . .	110
6.4	Application of the AP Migration . . . . .	112
6.5	Recommendation for Future Research . . . . .	112
<b>A</b>	<b>The Fourier Transform</b>	<b>118</b>
<b>B</b>	<b>The Ricker Wavelet</b>	<b>120</b>
<b>C</b>	<b>Processing of Complex Seismic Trace</b>	<b>122</b>
C.1	The Quadrature Trace . . . . .	123
C.2	Cross-correlation . . . . .	123
<b>D</b>	<b>Radon Transform</b>	<b>125</b>

# Chapter 1

## Introduction

### 1.1 The Seismic Method

Throughout the development of hydrocarbon exploration, the seismic method is still regarded as the most powerful method in searching for economic deposits of oil, gas or minerals, as well as for engineering and scientific studies. In hydrocarbon exploration, seismic investigations are applied at or near the Earth's or the sea's surface to measure the physical properties of the subsurface and to detect variations in those properties, which are usually indicative of changes in lithology (Kessinger, 2002).

In general, seismic exploration may be divided into three main steps (Yilmaz, 1992). The first step comprises seismic data acquisition. This step involves the generation of seismic waves and their subsequent detection after passing through or reflecting off the region of interest. The most frequently practiced form of seismic acquisition is the reflection seismic survey. In this step, the seismic data is gathered, either on land or at sea. The second step is seismic data processing, which leads to the desired image of the subsurface. The last step is interpretation, which is performed to recognize plausible geological patterns in the seismic image.

This research is mainly focused on the second step of the seismic method, particularly the imaging process that is essential for the interpretation step. Marine multi-channel seismic (MCS) reflection data, which indicate the presence of Bottom Simulating Reflectors (BSRs), are imaged in connection with amplitude versus angle (AVA) analysis. To perform an accurate AVA analysis, the amplitude-preserving (AP) migration method is developed to image the BSR in terms of angle-dependent reflectivity and structural image as well.

## 1.2 Bottom Simulating Reflector (BSR)

BSRs are seismic reflections that approximately mimic the seafloor, cut across reflections of stratigraphic origin and are characterized by a negative polarity indicating its origin from a decrease in acoustic impedance (Trehu et al., 1999). Furthermore, the BSR is generally interpreted as proof of a boundary surface between hydrate-bearing sediments and gas-bearing sediments located beneath them. The BSR marks the base of the gas hydrate stability zone and more or less coincides with its depth as predicted from the geothermal gradient. The BSR is especially common along the slope of subduction zone accretionary prisms. Information on the nature of the hydrate and the BSR from deep-sea drilling is very limited and much of the available information as to the origin of the BSR has come from seismic reflection data. Therefore, most information must be inferred remotely from seismic reflection data (Hyndman and Davis, 1992; Shipley et al., 1979).

The results of the previous investigations (Hyndman and Davis, 1992; Shipley et al., 1979), based mainly on amplitude versus offset (AVO) responses and synthetic modeling, indicate that the BSR generally appears to be characterized by negative reflection coefficients. Ecker (2001), based on two-dimension at  $P$  and  $S$  impedance contrast inversion, shows that the BSR appears to be characterized by a negative  $P$ -impedance contrast and a mostly positive  $S$ -impedance contrast. Local investigations of the BSR reflection character and amplitudes show that the BSR is underlain by many small structural layers, which contribute laterally to significant tuning effects. In areas without tuning, the BSR is characterized by a strong increase in amplitude with increasing offset, while the other areas exhibit more constant amplitudes with offset. In contrast, Yuan et al. (1994) conclude that the AVO behavior of the hydrate is found not to be useful as was earlier thought for characterizing the BSR. This is because Poisson's ratio change below the BSR due to gas is likely to be very small in high porosity unconsolidated sediments. Moreover, no reliable S-wave velocity information for sediments containing hydrate or gas is available.

Most previous work employed only standard seismic data processing and performed AVO analysis on unmigrated records, which is often hindered by the effects of common-depth-point smear, incorrectly specified geometrical spreading loss, and source/receiver directivity (Gray, 1997). Moreover, the correct amplitude information is lost during the processing

step. In this research, the BSR of MCS reflection data is imaged using the developed AP migration to recover angle-dependent reflection coefficients, which are important for AVA analysis.

### **1.3 Amplitude-Preserving Prestack Depth Migration**

Over the years the seismic processing techniques have broadened. Advanced seismic processing techniques are designed not only to extract structural images but also lithological information from seismic surface data (de Bruin et al., 1990). One of these techniques is amplitude-preserving (AP) prestack depth migration, which provides a key feature to seismic reservoir characterization.

Seismic modeling and seismic migration are intimately related. Seismic modeling defines the wave propagation from sources to receivers, generating focusing operators. Seismic migration attempts to undo the wave propagation effects to produce an image of the subsurface. In conventional seismic migration programs, the seismic modeling and the seismic migration are compiled in hard link and thus designed in one package. As a consequence, the focusing operators are unique and depend on which modeling algorithm is employed. In view of the flexibility in accommodating any kind of focusing operators (single-valued or multi-valued operators), a new method, the so-called AP migration is developed. This AP migration method is designed as a separate program from modeling algorithm. In its implementation, the AP migration directly uses the focusing operator in the form of seismograms, which can be obtained from the existing modeling algorithms (e.g., finite difference, ray-tracing, etc.). Thus, no explicit traveltimes information is required.

The difference of this new method to conventional migration methods is illustrated in the schematic flow of Figure 1.1. In this new method, the seismic modeling and the seismic migration, are compiled in soft link using SEG-Y I/O files. It is generally agreed that conventional methods effectively handle the focusing operators, which usually only need explicit traveltimes information. However, they are limited to fixed modeling algorithms. One of the advantages of the developed method is that one can use the appropriate modeling algorithm with respect to the knowledge of the macro model. When a very accurate velocity model is available, the modeling algorithm that calculates the full Green's function (e.g.,

finite difference) is appropriate, however, when only an approximate model is available it may be better to use the modeling algorithm that uses an asymptotic solution to the wave equation (e.g., ray tracing).

The strategy of the new migration scheme is based on the Delft approach (Berkhout, 1982; Berkhout, 1997a; Berkhout, 1997b) in removing wave field propagation effects. The migration process is formulated based on the Common Focus Point (CFP) technique. The difference between the CFP algorithm and conventional migration techniques (e.g., Kirchhoff migration) lies in the removal of the propagation effects, which is split into two consecutive focusing steps: focusing in detection and focusing in emission. The splitting of the removal process provides some advantages that not only creates significantly new insight in the seismic imaging process, but also it particularly allows the generation of intermediate output that opens new possibilities in seismic data analysis and seismic data processing. Moreover, the intermediate output reveal important information on errors in the underlying macro velocity model. In addition, the intermediate output provide band-limited information on the angle-dependent reflection property of the related grid-points in the subsurface.

The CFP technique is extended by applying the weight function to preserve correct amplitudes during the migration process. Since the AP migration directly uses the focusing operators in the form of seismograms, the parameters of the weight function (i.e., traveltimes, amplitude, phase and angle) are estimated from the seismogram operator itself. As a result, the AP migration not only produces a structural image but also recovers angle-dependent reflectivity information.

There are several methods for generating the focusing operators; the fast technique is the finite difference solution to the Eikonal equation (van Trier and Symes, 1991; Vidale, 1988). Its classical version only computes first arrival traveltimes. Later arrivals, which may contain important information, are not considered. Moreover, amplitudes are not handled at all. The most commonly used method in the imaging is the ray-tracing method (Červény and Soares, 1992). This technique computes correct traveltimes and amplitudes based on a high frequency approximation to the wave equation. However, it is only a good approximation to the solution in the seismic bandwidth if the slowness model is smooth on a scale that is long compared to the seismic wavelength. Rabbel (1987) gives estimates of the regimes

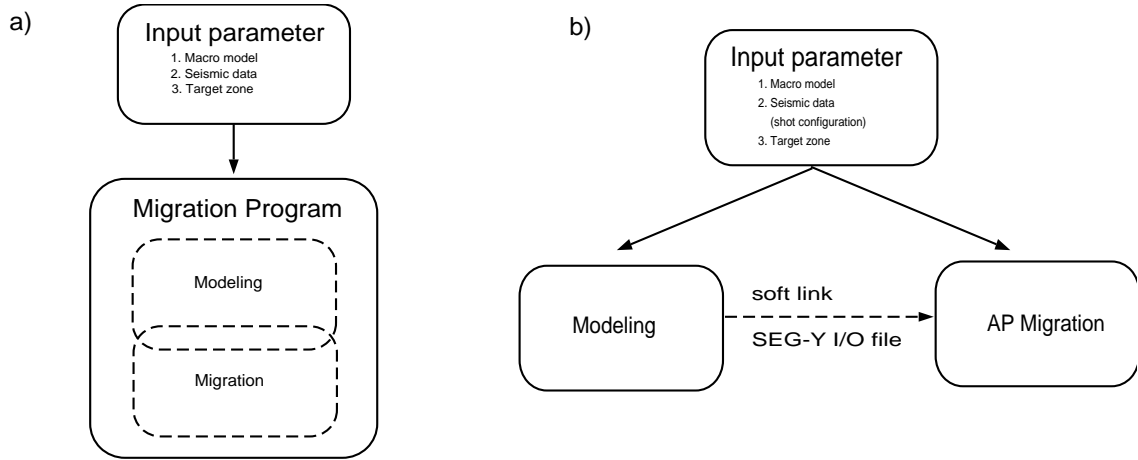


**Figure 1.1.** The comparison between schematic flow of conventional migration a) and the AP migration method b).

of the validity of this scheme. The finite difference modeling is commonly regarded as the most accurate method, which provides correct amplitudes and traveltimes within a certain frequency range. But this method is very slow and cost intensive.

In this work, the Nichols' method, also termed "band limited Green's function" (Nichols, 1994), which computes traveltimes, amplitude and phase, is chosen. The method is modified to calculate multi-valued focusing operators by using the parametric representation of the Green's function that is calculated in the same frequency band as the seismic data.

To summarize the aforementioned aspects, the following objectives are addressed:

- *to develop the amplitude-preserving (AP) prestack depth migration method, which is independent of the form of the focusing operators and is able to recover angle-dependent reflectivity and also to produce a structural image.*
- *to modify the band limited Green's function for generating multi-valued focusing operators.*
- *to apply the developed AP migration method for imaging bottom simulating reflectors (BSR) in connection with AVA analysis.*
- *to analyze the AVA behavior of the (hydrate) BSR using primary ( $R_p$ ) and secondary (Gradient) AVA attributes as well as AVA modeling.*

## 1.4 Outline

After having introduced the seismic methods, and given an overview of the BSR and the AP migration method in Chapter 1, Chapter 2 deals with the modeling of the focusing operator using the band limited Green's function method. Parameterization of the Green's function in terms of traveltimes, amplitude and phase information, which is the basic concept of the band limited Green's function method, is explained. The numerical examples range from simple to complex models and validate the modeling algorithm.

The theory of the CFP algorithm, which is the basic concept for developing the AP migration method, is described in Chapter 3. The description involves the prestack migration in terms of double focusing, the principle of equal traveltimes, and the forward model of primary reflections. The principle of the AP migration includes a generic integral form for a prestack imaging, the implementation of the CFP technique, and the compensation of geometrical spreading effects and wavelet phase shift to preserve amplitude and phase information during the migration process. The schematic flow of the AP migration is drawn in the end of this chapter.

Chapter 4 presents the application of the AP migration method to synthetic data. Near-surface (MCS = Multi Channel Seismic) and sea-bottom (OBH = Ocean Bottom Hydrophone) synthetic data are prepared to evaluate the performance of the AP migration method. The result of each subsequent step of the imaging process at one grid-point in the subsurface using simple generic model is displayed to analyze the sequence steps of the AP migration. To demonstrate the potential of the AP migration in complex media, the Marmousi model is migrated using a variety of input parameters such as: with and without compensation to geometrical spreading effects, the use of an approximate velocity model and the use of sparse-shot geometries. As a comparison to another migration method, the Marmousi data set is migrated using the standard Kirchhoff migration.

The application of the AP imaging to the seismic data collected across the continental margin offshore Oregon is presented in Chapter 5. Marine multi channel seismic reflection data of line OR89-02, which indicate the presence of a BSR, are imaged in terms of angle-dependent reflectivity as well as structural image. The migrated angle-dependent reflectivity gathers at several locations along the profile are displayed to analyze the local



AVA BSR response. Furthermore, in order to compare the migrated image of the AP migration to other migration methods, the data set is migrated using two commercial software packages; Kirchhoff migration and the finite difference migration. AVA inversion, based on the migrated angle-dependent reflectivity gathers, is performed to produce a primary and a secondary AVA attribute. AVA modeling is also conducted to estimate the possible physical characteristic of the subsurface.

Finally, the conclusions and perspectives including recommendations for further research are presented in Chapter 6.

## Chapter 2

# Modeling of Focusing Operators Using Band-Limited Green's Function

### 2.1 Introduction

Prestack seismic imaging aims at obtaining an estimate of the reflectivity information in the subsurface from a seismic investigation accomplished at the surface. The basic requirement for this process is the ability to remove the propagation effects from the seismic measurements. In this work, these propagation effects are quantified in terms of one-way wave field propagators in the macro model (Berkhout, 1982). Consequently, the removal of the propagation effects is accomplished by applying the inverse of these wave field propagators to the seismic data. These inverse propagators are approximated by forward modeling to generate the focusing operator. Modeling of the focusing operator requires the calculation of characteristic quantities of seismic waves such as traveltimes, amplitudes, and phase information.

A wide variety of methods is available to generate the focusing operator. The most common techniques are those based on the finite difference solution to the Eikonal equation and those based on ray tracing. All of these methods solve a high frequency approximation to the wave equation. They only provide a good approximation to the solution in the seismic bandwidth if the slowness model is smooth on a scale that is long compared to the seismic wavelength. Some algorithms have a limitation, particularly when they are used to compute multi-arrivals. Some implementations compute only the first arrivals like the classical finite difference solution to the Eikonal equation (van Trier and Symes, 1991; Vidale, 1988).

Although they calculate the first arrivals efficiently, they do not model the later arrivals. If the first arrivals contain little energy, the solution obtained will be a poor approximation to the full Green's function (Nichols, 1994). Ray tracing is based on the concept that seismic energy of infinitely high frequency follows a trajectory determined by the ray tracing equations. The method explicitly calculates the rays and then uses the coordinate frame to calculate the traveltimes, amplitudes, and phases. Multi-arrivals can be introduced as long as there are enough rays to be traced. However, care must be taken to allow rays to penetrate in the complete subsurface.

In principle, the developed AP migration method is independent of modeling programs as described in Chapter 1. The AP migration method requires only the focusing operators in the form of seismograms. This means that the focusing operators may be constructed using the existing modeling programs. However, based on the availability and the flexibility of the algorithm, the Nichols' method, the so-called band-limited Green's function is modified to calculate multi-valued traveltimes, amplitudes and phases. This algorithm requires the estimation of the Green's function for every subsurface (source and receiver) location and every frequency. The Green's function is parameterized by traveltimes, amplitudes and phases at each point, which are calculated in the seismic frequency range.

This chapter theoretically discusses the basic concept of the Nichols' method including its general scheme in estimating traveltimes, amplitudes and phase information. For more thorough treatments, see Nichols (1994). The numerical examples of the focusing operator ranging from simple to complex models are given in the final sections (2.5.1 to 2.5.4).

## **2.2 A Parametric Model of the Green's Function**

The calculation of a wide band Green's function for a medium, which contains lateral and vertical velocity variations, should be carried out at every surface location and every frequency. This may be prohibitively expensive and requires a large storage. A parametric form of Green's function will overcome the problems associated with the use of the full Green's function. The following is the parametric form of the Green's function that describes the Green's function in terms of impulsive arrivals in the time domain:

$$G(x_1, x_2, \omega) = A(x_1, x_2)e^{-i\omega\tau(x_1, x_2)} \quad (2.1)$$

Here,  $A$  is the amplitude of the arrival and  $\tau$  is the traveltime. The advantage of this parameterization is that these quantities may be used directly in time modeling schemes and thus reduce the use of memory by storing three real valued coefficients for each Green's function instead of a complex number for each of several hundred frequencies.

### 2.3 Single-Arrival Model

Parameterization of the Green's function in terms of traveltime, amplitude and phase can be modeled in any arrival model. A single-arrival model is the simplest model, but is only valid for a very smooth velocity field. Multi-arrivals models will give a good approximation for a complex velocity field.

#### 2.3.1 Non-Dispersive Single-Arrival Model

The Green's function for non-dispersive arrivals from each source location,  $s$ , to the subsurface location,  $x$ , can be represented by the following equation:

$$G(s, x, \omega) = A(s, x)e^{i\phi_0(s, x)}e^{i\omega\tau(s, x)} \quad (2.2)$$

Equation (2.2) shows that the total phase at any frequency is represented by  $\omega\tau(s, x) + \phi_0(s, x)$ . The linear interpolation of the unwrapped phase will exactly recover the phase for all frequencies if the Green's functions match to this model. In this case, the amplitude is constant for all frequencies. In addition, if only one non-dispersed arrival is known for the given velocity field, then only simple interpolation of two frequencies is needed. The Green's function at this location can be completely calculated using the amplitude and unwrapped phase information. Based on the amplitude,  $A(s, x, \omega)$ , and unwrapped phase,  $\zeta(s, x, \omega)$ , at two frequencies  $\omega_1$  and  $\omega_2$  it can be obtained:

$$\begin{aligned} A(s, x) &= (A(s, x, \omega_1) + A(s, x, \omega_2))/2 \\ \tau(s, x) &= (\zeta(s, x, \omega_2) - \zeta(s, x, \omega_1))/(\omega_2 - \omega_1) \end{aligned} \quad (2.3)$$

$$\phi_0(s, x) = \zeta(s, x, \omega_1) - \omega_1 \tau(s, x)$$

Equation (2.3) will be more simple with only one frequency if all arrivals are assumed to be zero phase.

$$\begin{aligned} A(s, x) &= A(s, x, \omega_1) \\ \tau(s, x) &= \zeta(s, x, \omega_1)/\omega_1 \end{aligned} \quad (2.4)$$

Many asymptotic schemes assume that phase is a linear function of frequency for all frequencies (from zero to very large frequencies). As a consequence, if this is not true, the asymptotic methods may give solutions that are inappropriate for the seismic bandwidth. However, this is different in this case, where the simple interpolation of two frequencies in the seismic frequency band only assumes that phase is a linear function in between two frequencies.

### 2.3.2 Dispersive Single-Arrival Model

For the dispersive single-arrival model, the phase will not be a linear function of frequency and the amplitude will not be constant. Two approaches are used to classify the dispersion; intrinsic and geometric dispersion. The intrinsic dispersion is a particular model of the constant-Q medium that can be modeled by using a complex frequency-dependent velocity in the wave field extrapolation (Nichols, 1994). The geometric dispersion is caused by heterogeneities in the velocity model. For a model with a strong velocity variation, the single dispersed arrival model will only be valid if the heterogeneity is large enough to cause dispersion.

It is possible to approximate the amplitude and phase functions with piecewise linear functions for light dispersion. For this case, the Green's function can be calculated at sparse frequencies, thereafter for each pair of frequencies the amplitude and phase are determined by using a linear interpolation. In this model the amplitude and phase are assumed to be linear functions of frequency over some bandwidth  $\omega_0 \leq \omega \leq \omega_1$ . In addition, the Green's function can be modeled by an initial amplitude and phase along with their gradients based on two Green's functions at frequencies  $\omega_0$  and  $\omega_1$ .

$$\begin{aligned}
A_0(x, z, \omega) &= A(x, z, \omega_0) \\
\delta A(x, z, \omega) &= (A(x, z, \omega_1) - A(x, z, \omega_0))/(\omega_1 - \omega_0) \\
\phi_0(x, z, \omega) &= \phi(x, z, \omega_0) \\
\delta \phi(x, z, \omega) &= (\phi(x, z, \omega_1) - \phi(x, z, \omega_0))/(\omega_1 - \omega_0)
\end{aligned} \tag{2.5}$$

For any frequency in between  $\omega_0$  and  $\omega_1$ , the Green's function can be calculated using:

$$\begin{aligned}
G(x, z, \omega) &= A(x, z, \omega)e^{i\phi(x, z, \omega)} \\
A(x, z, \omega) &= A_0(x, z) + \delta A(x, z)(\omega - \omega_0) \\
\phi(x, z, \omega) &= \phi_0(x, z) + \delta \phi(x, z)(\omega - \omega_0)
\end{aligned} \tag{2.6}$$

For an arrival with a constant phase shift (as expected for waves that pass through a focus) the amplitude varies as a function of frequency and may be modeled using piecewise linear functions. For strong intrinsic dispersion, however, the phase will not be well approximated by a piecewise-linear function. In this case higher order interpolation could be used, e.g., linear interpolation in amplitude and quadratic interpolation in phase.

## 2.4 Multi-Arrivals Model

In media with laterally and vertically velocity variations several arrivals from different paths between source and receiver are observed. Hence more than one arrival exists at a single location. In this case, the phase is no longer a linear function of frequency. Suppose the two arrivals with amplitudes  $A_1$ ,  $A_2$  and traveltimes  $\tau_1$  and  $\tau_2$  are seen in the same location, then

$$P(\omega) = A_1 e^{i\omega\tau_1} + A_2 e^{i\omega\tau_2} \tag{2.7}$$

Equation (2.7) expresses a linear superposition of the two arrivals. The phase of the combined wave field will not be a linear superposition of the two phases.

$$\begin{aligned}
P(\omega) &= A_1 \cos(\omega\tau_1) + A_2 \cos(\omega\tau_2) + i(A_1 \sin(\omega\tau_1) + A_2 \sin(\omega\tau_2)) \\
\phi(\omega) &= \arctan \left[ \frac{A_1 \sin(\omega\tau_1) + A_2 \sin(\omega\tau_2)}{A_1 \cos(\omega\tau_1) + A_2 \cos(\omega\tau_2)} \right]
\end{aligned} \tag{2.8}$$

In order to fit an  $n$ -arrival model to the calculated mono-frequency Green's functions, the amplitudes,  $A_i$ , phases,  $\phi_i$ , and traveltimes,  $\tau_i$ , should be obtained such that the calculated Green's function,  $P(\omega)$ , is predicted correctly for all modeled frequencies, then

$$\sum_{i=1}^n A_i e^{i\phi_i} e^{i\omega\tau_i} = P(\omega) \tag{2.9}$$

#### 2.4.1 Arrival Identification

Arrival identification can be performed by simply transforming the data from the frequency domain to the time domain.

$$P(t) = \int_{-\infty}^{\infty} P(\omega) e^{-i\omega t} d\omega \tag{2.10}$$

This integral is replaced by a discrete form because the Green's function is calculated for sparse frequencies in the set of frequencies,  $\omega_k = k\delta\omega$  ;  $kl \leq k \leq kh$ . Equation (2.10) then becomes:

$$P(t) = \sum_{k=kl}^{kh} P(\omega_k) e^{-ik\delta\omega t} \delta\omega \tag{2.11}$$

Equation (2.11) introduces a replication of Green's functions in time as a consequence of the sampling of the frequency ( $\omega$ ).

$$\begin{aligned}
P(t + n2\pi/\delta\omega) &= \sum_{k=kl}^{kh} P(\omega_k) e^{-ik\delta\omega(t+n2\pi/\delta\omega)} \\
&= \sum_{k=kl}^{kh} P(\omega_k) e^{-ik\delta\omega t} e^{ikn2\pi} \\
&= P(t)
\end{aligned} \tag{2.12}$$

The arrival identification will be unproblematic if the different aliases are non-overlapping, but if the arrival is not distinct, the arrival identification will be more difficult because

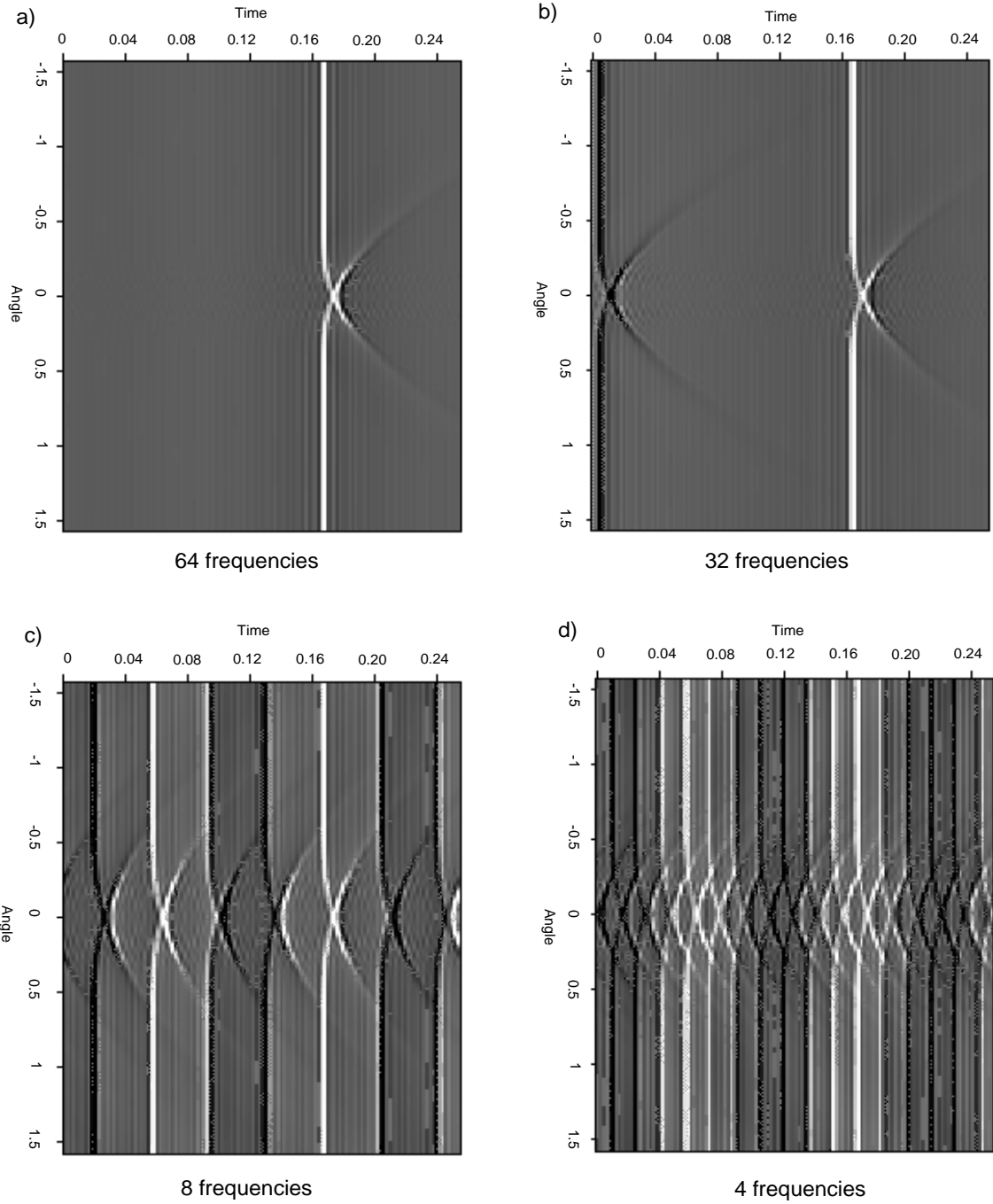


**Figure 2.1.** Replication of the Green's function in time using a sparse frequency sampling based on the blob model. The Green's function is calculated using 64 a), 32 b), 8 c) and 4 d) frequencies (Nichols 1994).



the correct Green's function is contaminated by aliasing. Nichols (1994) demonstrated the replication of the Green's function in time, which is shown in Figure 2.1, using a sparse frequency sampling. The Green's function is plotted in the angle/time domain for a fixed radius. Each panel consists of 128 time samples, so the correct band limited Green's function is obtained by using 64 frequencies. The Green's function calculation using 32 and 8 frequencies still provides separable arrivals, however, when 4 frequencies are used all arrivals are overlapping.

### 2.4.2 Arrival Estimation

The parameterization of the Green's function in terms of one or more arrivals can be done by choosing the arrival based on the amount of energy in each arrival. For a single-valued operator, the maximum energy arrival will be the best possible estimate that is in the form of a single set of three parameters (amplitude, travelttime, and phase). To choose the maximum energy arrivals, the data are transformed to the time domain to calculate the energy as a function of time. The energy function will be replicated in time due to the sparse sampling in frequency. Since the calculated mono-frequency Green's are outgoing waves on a polar grid, then the travelttime at the next radius must be greater than the previous travelttime. Moreover, the travelttime difference must be less than the radius increment divided by the maximum velocity. Thereby, the correct maximum energy travelttime can be chosen.

For generating a multi-valued operator, the arrival identification step at each radius is modified by picking the number of arrivals based on the energy function. The multi-arrival identification is carried out by defining a lower and an upper boundary of the time window based on the minimum and maximum travelttime at the previous radius. The data in the time window are then transformed to the time domain using the Fourier transform. Thereafter, all arrivals are sequentially sorted based on their energy from maximum to minimum. To avoid the contamination by aliases, the replication interval due to sampling in frequency must be greater than the window size. For example, the length of the time window is chosen to be half the replication interval.

In principle, the band limited Green's function algorithm provides a travelttime solution in a user-defined frequency band. A small number of frequencies in the seismic frequency

band are extrapolated outward from the source location using a paraxial one-wave equation in polar coordinates. At each radius, a parametric approximation to the wave field is estimated as follows (after Nichols, 1994):

- Calculating the Green's functions for a sparse frequency sampling at the new radius.
- Choosing a time window centered on the traveltimes from the previous radius.
- Calculating a sampled time domain representation in the window by Fourier transform.
- Sorting all arrivals sequentially (from maximum to minimum energy)
- Picking the multi-arrivals from the sorted arrivals.
- Finding the traveltime of the multi-arrivals based on the energy function using a quadratic fit.
- Calculating the amplitude and phase at each picked traveltime.

To resolve separate peaks in the energy function, the sampling used for the time window must be fine enough and it is related to the bandwidth over which the Green's functions have been calculated. Since the window typically consists of only a few time samples, the use of a slow Fourier transform is reasonable.

## 2.5 Numerical Examples

This section presents the results of the modeling algorithm, which are illustrated with numerical examples to describe the subsequent steps in constructing the  $x - t$  focusing operator. Note that the modeling program produces traveltime, amplitude, and phase in separate panels instead of the full waveform operator. This means that an extra processing step after band-limited Green's function computation is needed. This step builds the full waveform operator in  $x - t$  domain by employing convolution between the panel series (traveltime, amplitude, and phase) and a wavelet. In this study, a zero phase Ricker wavelet (see Appendix B), which is easy to implement, is used to construct the focusing operator. The models used in this study only contain velocity contrasts. The density is assumed to be constant throughout the models.

The extra processing step is immediately carried out after the modeling program produced traveltimes, amplitudes, and phases. The modeling program and the full-waveform operator construction program are performed simultaneously in parallel processing with the output as a seismogram operator in SEG-Y format. In the main migration scheme, this operator will be directly sent to the AP migration program.

As described in the previous section, the parametric approximation to the wave field is estimated by extrapolating a number of frequencies outward from the source location in polar coordinates. Therefore, in order to obtain stable results, special attention should be paid to the input parameter of the modeling program. One of these parameters is the number of frequencies to use in the estimation of Green's function. The influence of this parameter is illustrated in Figure 2.1. Another parameter is the number of radius increments for the polar grid. The other parameter is the number of angles for the polar grid. In practical applications, the last two parameters can be automatically defined by determining the desired output-grid (e.g., receiver spacing). Both parameters are very sensitive, particularly for handling a complex velocity model. In principle, the algorithm needs a fine output-grid to avoid introducing an artifact while transforming back to rectangular coordinates.

Four velocity models ranging from simple to complex are used to demonstrate how well the modeling method performs. The first model is a constant velocity model, which is a standard to test whether the method computes correct traveltime, amplitude, and phase. The second model is a two-layer velocity model with a horizontal reflector (interface). This model is used to test the method in handling the transition between layers correctly. The third model is a two-layer velocity model with a dipping reflector. The fourth model contains a local velocity variation, a so-called "blob" velocity, which is used to see if the modeling program produces a triplicating wavefront.

### 2.5.1 Focusing Operator in a Constant Velocity Model

The simple model, a constant velocity medium, is used to test whether the method computes correct traveltimes, amplitudes, and phases. The velocity is 2000 m/s throughout the model. The size of the model ranges from 0 m to 8000 m in the horizontal direction and from 0 m to 5000 m in the depth direction. The velocity model is shown in Figure 2.2a. The calculated

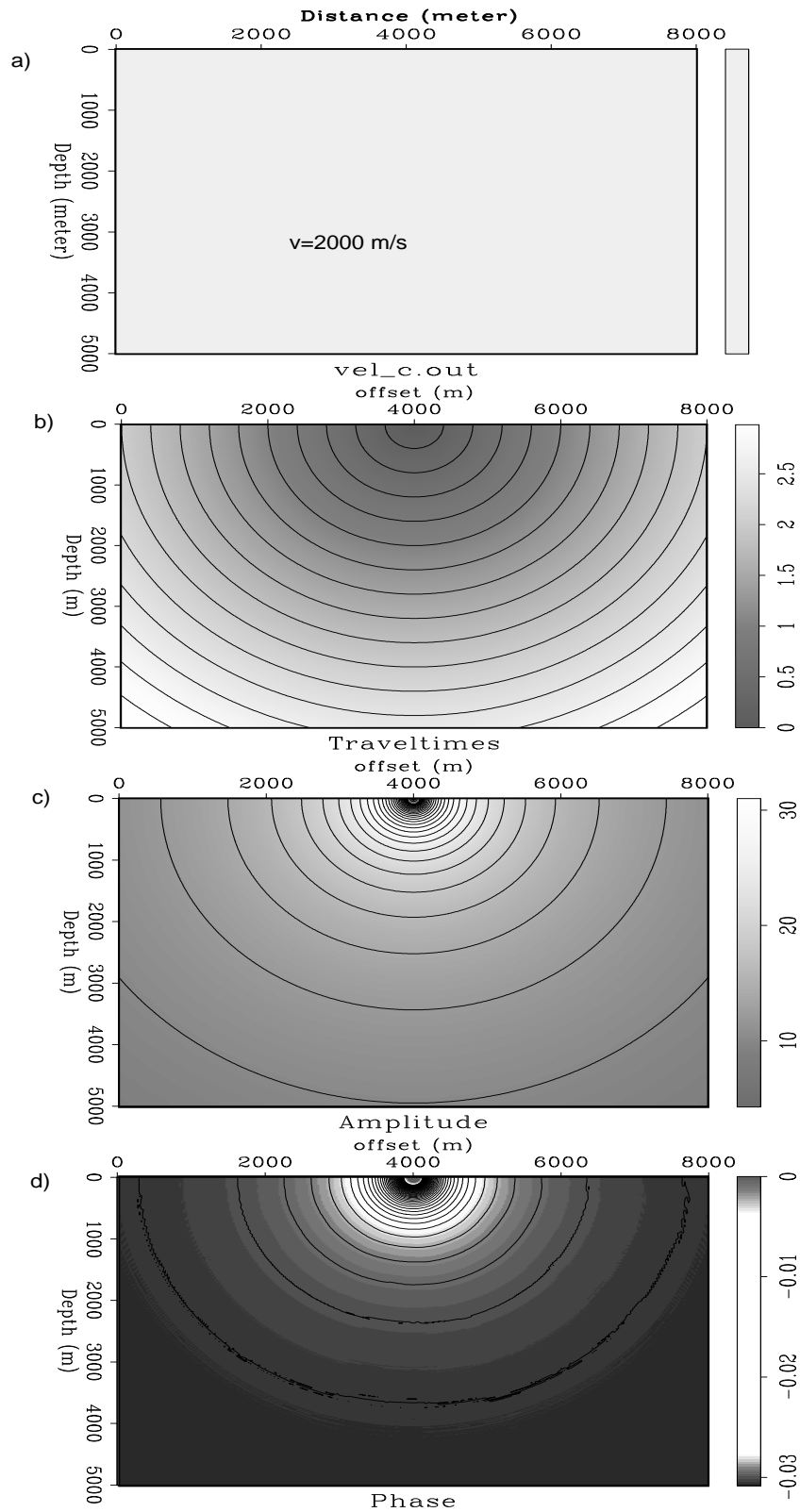


**Figure 2.2.** Forward modeling using a constant velocity model a), for which traveltimes b), amplitudes c), and phases d) are calculated using the band-limited Green's function.

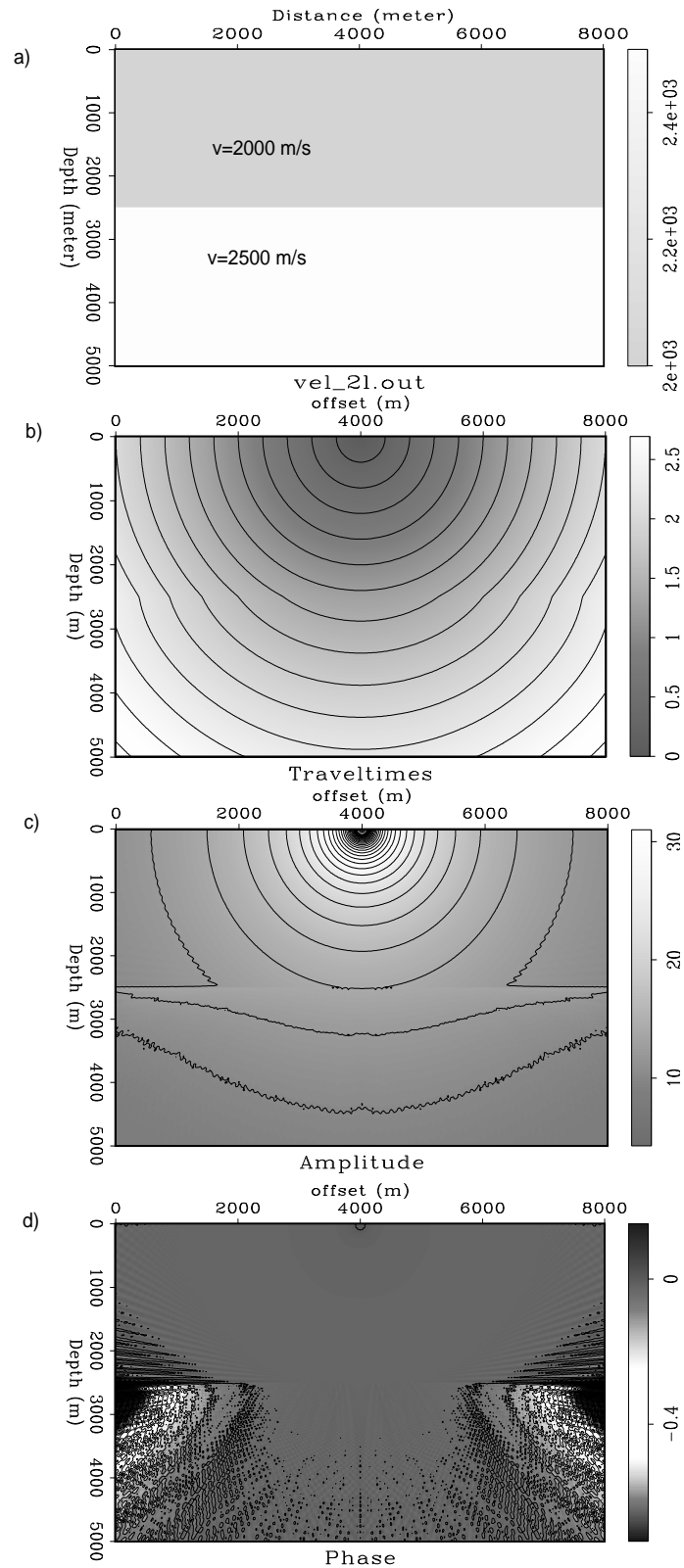
wave field (traveltime, amplitude, and phase) is mapped onto the output-grid spacing of  $x=25$  m and  $z=25$  m. The wave field is propagated throughout the subsurface from the source, which is located at the surface ( $x=4000$  m,  $z=0$  m).

Figure 2.2 shows the traveltimes, amplitudes, and phases calculated for a constant velocity model. Traveltimes, amplitudes, and phases are calculated at every point in the subsurface and the solution is an estimate of the Green's function in the seismic frequency band. Since the velocity model is constant, the wave field propagation produces a smooth wavefront, and no changes or triplicating in the wavefront is observed. Therefore, the resulting operator is single-valued. The seismogram operator is then generated by convolving the three modeling outputs (traveltimes, amplitudes, and phases) with a Ricker wavelet of 25 Hertz. The seismogram operator, which is the response of a one-way propagation from the source at the surface to a subsurface grid-point at a depth of 2500 m, is presented in Figure 2.6a. It can be noticed that the aperture of the focusing operator is symmetric, which is a consequence of the constant velocity model.

### 2.5.2 Focusing Operator in a Two-Layer Velocity Model with a Horizontal Reflector

To see whether the transitions between layers are modeled correctly, a two-layer velocity model with horizontal reflector is used. The propagation velocity of the layers increases with increasing depth. The model has a rigid boundary between two velocity layers. The size of the model ranges from 0 m to 8000 m in the horizontal direction, and from 0 m to 5000 m in the depth direction. The propagation velocities for the layers are 2000 m/s and 2500 m/s for the first and the second layer, respectively. The boundary between the layers lies at a depth of 2500 m. The output-grid spacing of this model is  $x=25$  m and  $z=25$  m. The model is illustrated in Figure 2.3a. The wave field is propagated from the source at the surface ( $x=4000$  m,  $z=0$  m) throughout the subsurface.

The map of traveltimes, amplitudes, and phases, which are computed by the band limited Green's function for a two-layer velocity model with horizontal reflector, are shown in Figure 2.3. This model produces the changes of the wavefront that occur along the interface. This can be seen in the traveltimes, amplitudes, and phases maps. There are variations in the



**Figure 2.3.** Forward modeling using a two-layer velocity model (a) with a horizontal reflector in which traveltimes b), amplitudes c), and phases d) are calculated using the band-limited Green's function.

traveltimes starting at a depth of 2500 m when the wave fields pass through the interface. The wave field propagation becomes faster in the second layer as the velocity increases. The dramatic changes are clearly seen in the amplitude and phase maps. The amplitude map shows the difference of the pattern of the amplitude decay between the first and the second layer. Note that even for a dramatic variation, the method is able to provide reasonable results. This is evidence that there are no restrictions on the smoothness of the model. This is one of the advantages of the use of the band-limited Green's function, which is based on frequency band approximation rather than high frequency approximation (e.g., ray tracing based method).

The focusing operator is generated with the same procedure as the previous model by convolving all three modeling outputs (traveltimes, amplitudes, and phases) with the Ricker wavelet of 25 Hertz. The seismogram operator, which represents the response of downward propagation from source to subsurface grid-point at depth of 2500 m, is given in Figure 2.6b. Again, the aperture of the focusing operator is symmetric, since the reflector is horizontal.

### 2.5.3 Focusing Operator in a Two-Layer Velocity Model With a Dipping Reflector

The third model is a two-layer velocity model with a dipping reflector. The size of the model ranges from 0 m to 8000 m in the horizontal direction, and from 0 m to 5000 m in the depth direction. The dip-angle of the reflector is about 10 degrees with respect to the surface. The model has also a rigid boundary between two velocity layers. The velocity above the reflector is 2000 m/s and below the reflector is 2500 m/s. The output-grid spacing of this model is  $x=25$  m and  $z=25$  m. The velocity model is shown in Figure 2.4a. This model is used to see the transition between layers that occur in the dipping reflector. The shooting configuration is the same as the previous model, the source is positioned at the surface ( $x=4000$  m,  $z=0$  m) and is propagated throughout the subsurface.

The traveltimes, amplitude, and phase maps for this model are shown in Figure 2.4. This model produces changes in the wavefront when the wave fields pass through the velocity change that occurs along the interface following the dip of the reflector. The variation, which is shown in the traveltimes map, is also observed in the amplitudes and phases maps.

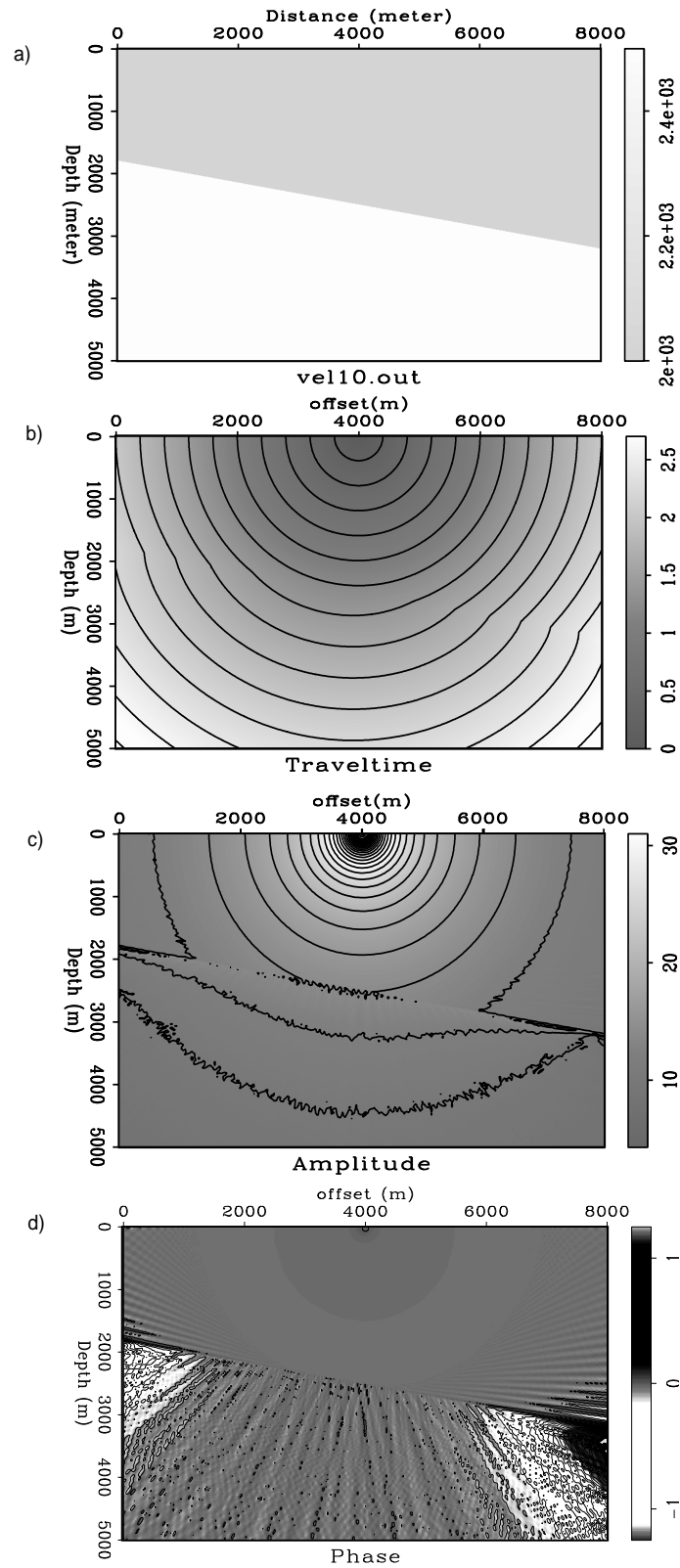


**Figure 2.4.** Forward modeling based on a two-layer velocity model with a dipping reflector a), for which traveltimes b), amplitudes c), and phases d) are calculated using the band-limited Green's function.



The traveltime map looks as smooth as Figure 2.3b, the traveltime map of the horizontal reflector. However, the amplitude map, especially in the second layer, shows rough contour compared to Figure 2.3c, since the grid, which is used for polar coordinates, follows the output-grid spacing ( $x=25$  m and  $z=25$  m). In order to get a stable result, particularly for either a dipping reflector or complex model, the grid for polar coordinates must be fine enough (e.g., half of the output-grid spacing). The example of a complex model (i.e., blob velocity model) using a fine grid is shown in the next section.

The same procedures as the first and the second model are performed to construct the seismogram operator. The synthetic seismogram, which is the response of downward propagation from the source location at the surface ( $x=4000$  m,  $z=0$  m) to the subsurface grid-point at a depth of 2500 m, is displayed in Figure 2.6c. Because of the dipping reflector the aperture of the focusing operator of this model is not symmetric.

#### 2.5.4 Focusing Operator in Blob Velocity Model

The last model contains a low velocity zone at  $x=4000$  m and  $z=1500$  m. The low velocity zone has a circular shape with radius of 1000 m and the velocity is varied from 1500 m/s (in the center of the focus) to 2000 m/s. The background velocity throughout the model is 2000 m/s. This model is called a "blob" velocity model. The dimension of the model again ranges from 0 m to 8000 m in the horizontal direction and from 0 m to 5000 m in the depth direction. The model is shown in Figure 2.5a. Due to the large velocity contrast around the focus, the model produces multi-arrivals. For this model, a finer output-grid ( $x=12.5$  m,  $z=10$  m) is applied. The wave field is again propagated throughout the subsurface from the source at the surface ( $x=4000$  m,  $z=0$  m).

The maps of traveltimes, amplitudes, and phases for the velocity blob are presented in Figure 2.5. Note that traveltimes, amplitudes and phases are obtained at every grid-point in the subsurface even when the model contains a caustic. This model produces a triplicating wavefront. The wavefront passes through a caustic starting at a depth of 1500 m as shown in the traveltime map. After the caustic, there are three arrivals to the wavefront. In many locations the last arrival is the highest energy arrival. In the phases map it can be seen that a large phase change occurs in the regions where a later arrival exists.

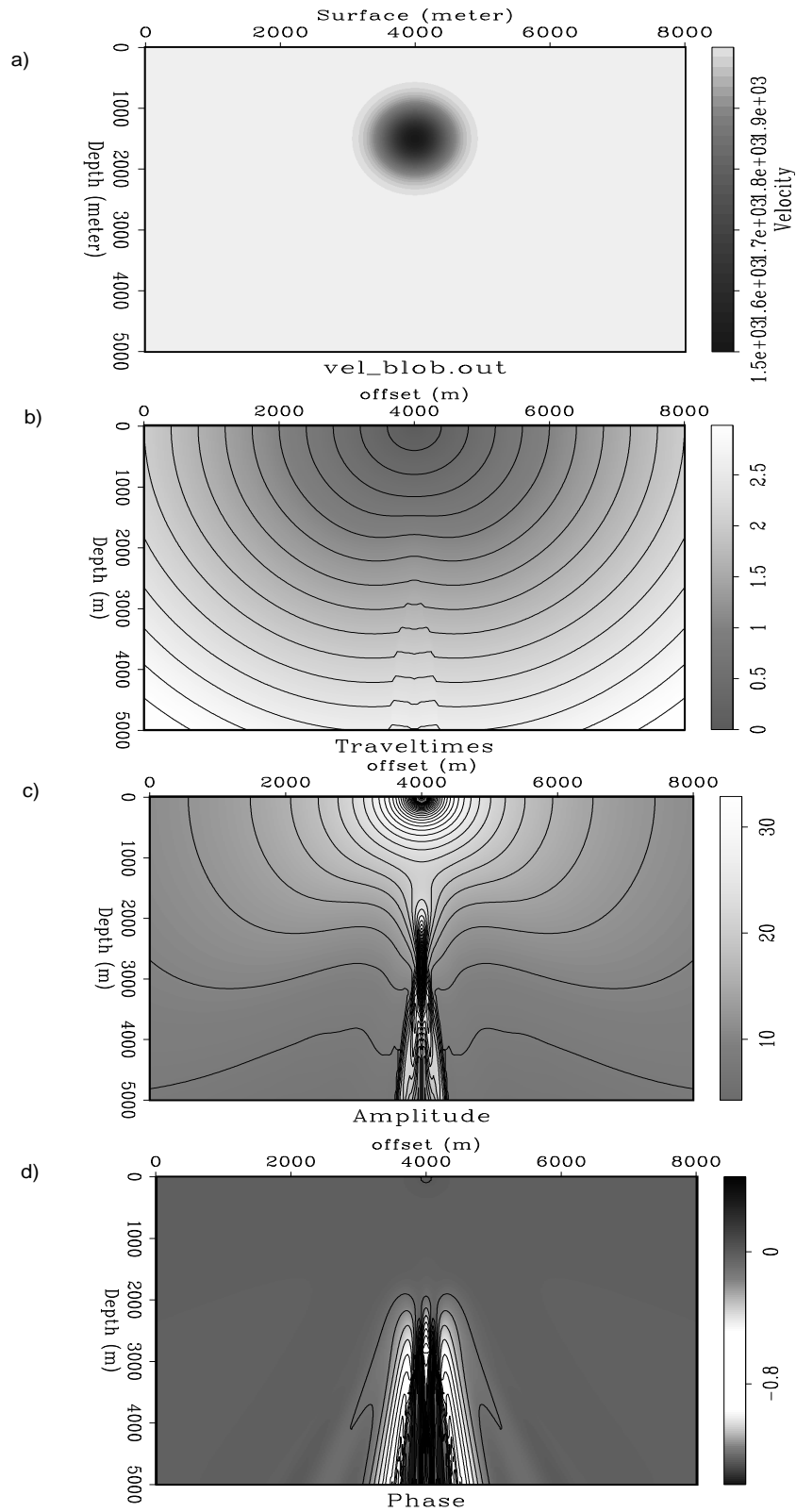


**Figure 2.5.** Forward modeling of a blob velocity model a), which produces traveltimes b), amplitudes c), and phases d) using the band-limited Green's function.

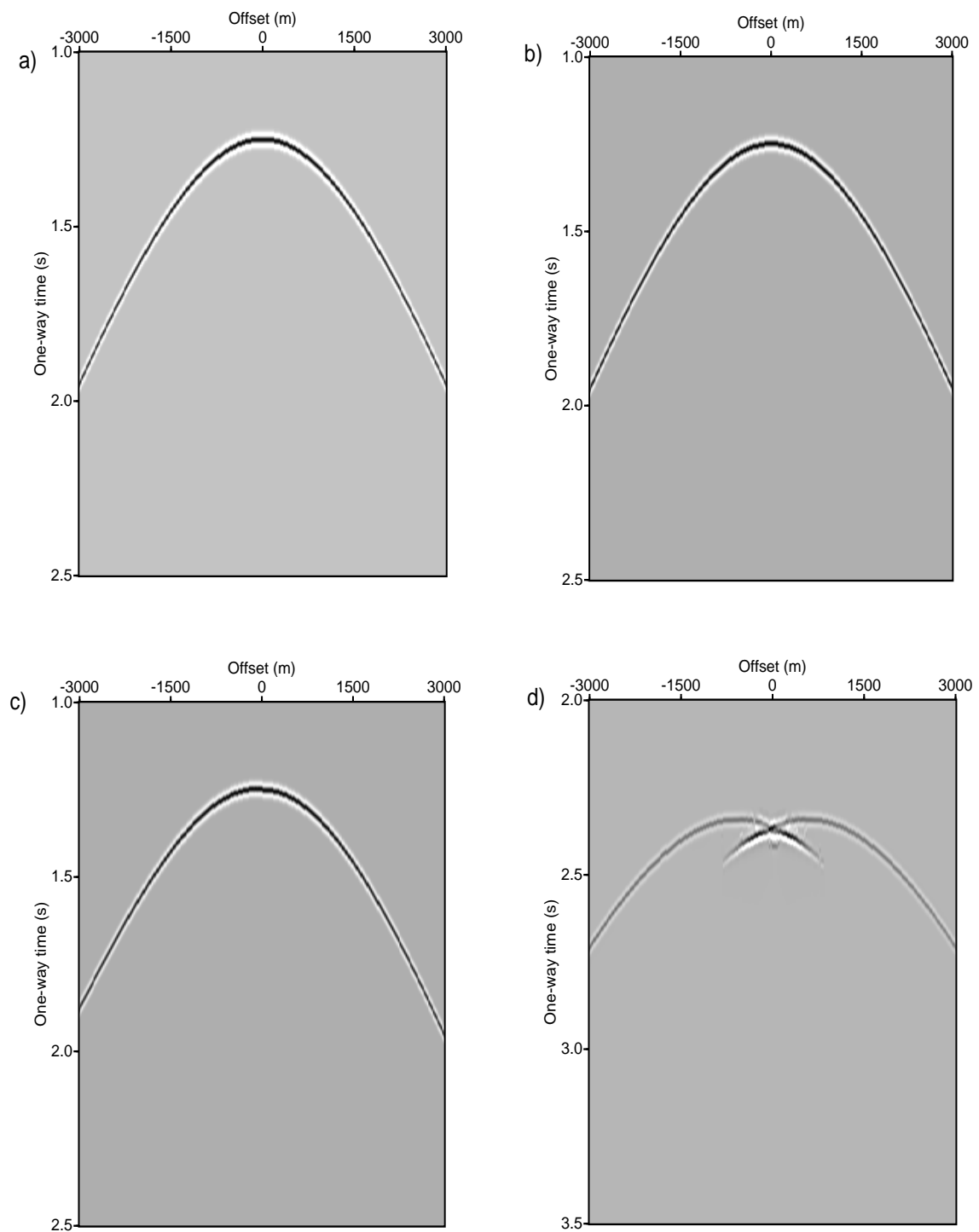


**Figure 2.6.** Focusing operators of a constant velocity model a), a two-layer velocity model with horizontal reflector b), a two-layer velocity model with a dipping reflector c), and a blob velocity model d), are constructed by convolving the modeling output with a Ricker wavelet of 25 Hertz.

Extra processing is also carried out by convolving the three outputs (traveltimes, amplitudes, and phases) and the Ricker wavelet of 25 Hertz to build the full waveform focusing operator. The focusing operator, which is a response of one-way propagation from the source to the grid-point at a depth of 4500 m, is shown in Figure 2.6d. The figure shows multi-valued operator.

## Chapter 3

# CFP - Amplitude-Preserving Prestack Depth Migration

### 3.1 Introduction

Ideally, seismic data processing should preserve amplitude information, however, this is not always the case. Often seismic data processing is only designed to remove noise and to restore lost amplitude information by applying a scaling factor. In reflection seismics, migration is an important processing technique to estimate an image of the subsurface. In its development, the migration technique improves its ability to preserve the amplitude of reflections, which are important in subsequent Amplitude Versus Angle (AVA) analysis. This technique has become an interesting topic in the last few decades. The enormous number of references indicate the importance of and demand for this topic.

Instead of citing many references, the interested reader is referred to a few approaches that are recognized as fundamental for basic principles and for some widely used modern specialisations. The first is the Delft approach (Berkhout, 1997a; Berkhout, 1997b; Berkhout, 1992; de Bruin et al., 1990), which was pioneered by Berkhout (1982) and developed by colleagues at Delft University. The second is the Center for Wave Phenomena approach (Hanitzsch et al., 1994; Hubral et al., 1991; Hubral, 2001), which was introduced by Bleistein et al. (1987) and developed at the Colorado School of Mines, then modified by Hubral and colleagues at the University of Karlsruhe. The third is the least-squares approach, which was introduced by Tarantola (1984) and developed internationally by many workers (LeBras and Clayton, 1988). The comparison of these three approaches shows that none of

the methods is in every aspect superior to the others. These methods differ significantly in their derivations, as well as their implementation and applicability (Gray, 1997).

In this work, an Amplitude-preserving (AP) prestack depth migration method is developed in order to obtain an image of the subsurface and to estimate angle-dependent reflectivity information, which is a key feature to seismic reservoir characterization. The strategy of the migration scheme is based on combining the Delft approach (Berkhout, 1997a; Berkhout, 1997b) for removing wave field propagation effects and the application of a weight function for preserving amplitudes during the migration process. The migration process is formulated based on the Common Focus Point (CFP) technique. This technique is basically a migration concept: by extrapolating the acoustic energy into the subsurface, the propagation effects are removed, and only the reflectivity information of the chosen grid-point remains. The difference of CFP migration in comparison to conventional migration is the fact that the removal of the propagation effects is split in two separate steps. It particularly allows the generation of intermediate output that open new possibilities in seismic data analysis and seismic data processing. The intermediate output reveal important information on errors in the underlying macro velocity model. In addition, by using the intermediate output the migration scheme produces not only the structural images but also the angle-dependent reflection properties of the related grid-points in the subsurface.

The AP migration method is designed as a separate program from modeling algorithms by requiring migration operators in the form of seismograms as so-called seismogram operators. Thus, it may be implemented using any kind of focusing operators (e.g., single-valued, multi-valued) obtained from the existing modeling algorithm. All required quantities for amplitude-preserving migration are estimated from the seismogram operators.

According to the modeling algorithm, which is applied to construct the focusing operator (i.e., the band limited Green's function), the AP migration is a special implementation of the migration technique where the amplitude of the migrated depth image corresponds to the reflection coefficients of the reflector under consideration (lossless, 2-dimension acoustic, 2-dimension geometrical spreading compensation and phase correction).

This chapter presents the basic concept of the CFP theory and its implementation in connection with amplitude preservation as well as the general scheme of the AP migration

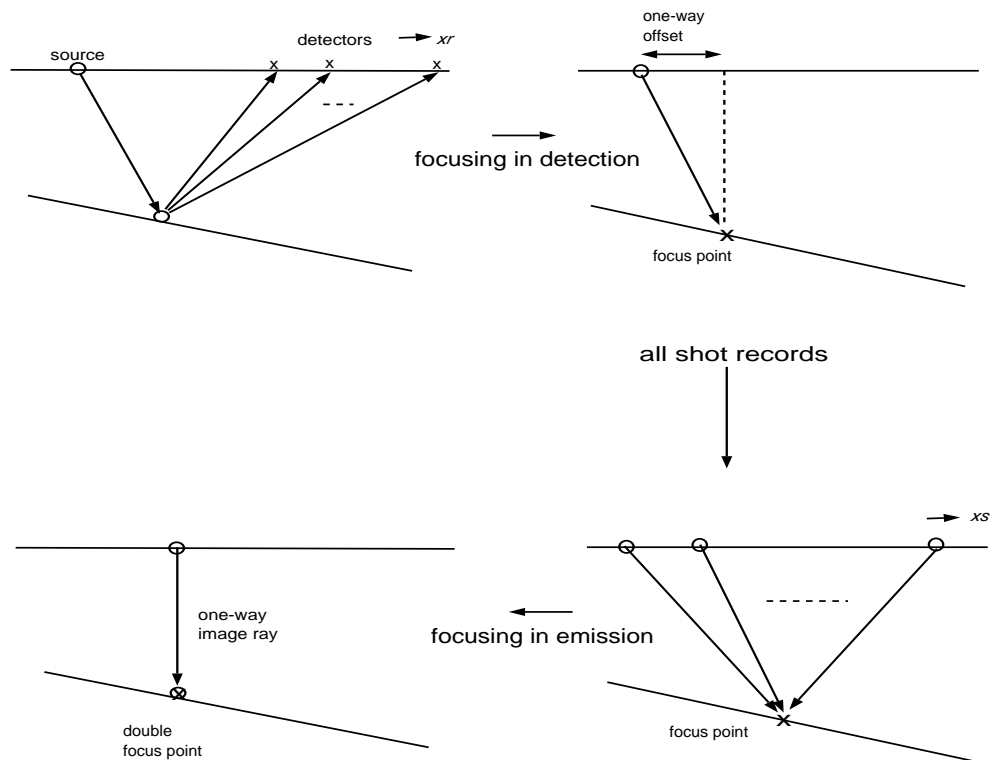


**Figure 3.1.** The CFP technique. Focusing in detection; each shot record is transformed to one event of the focus-point response. Focusing in emission; all events in the focus-point response are aligned to the one-way image time, followed by weighted superposition (Berkhout 1997a).

method.

### 3.2 Prestack Migration in Terms of Double Focusing

Prestack migration aims at estimating the reflectivity information at each depth level by removing the propagation effects from the prestack data set. The CFP technique, which was proposed by Berkhout (1992) based on the areal shot record theory, describes the removal process of the propagation effects in terms of double focusing concept (i.e., focusing in emission and focusing in detection). The double focusing concept is performed sequentially in which its order may be interchanged. The illustration of the CFP algorithm is given in Figure 3.1 (Berkhout, 1997a).

The first removal process is focusing in detection. This process synthesizes focused

receiver arrays in which they "sense" the response of single subsurface grid-point. The synthesis process transforms all available shot records into Common Focus Point (CFP) gathers. Each trace in the CFP gather is the result of the inverse extrapolation of a shot record, which is situated at the source position. This process illustrates that all receivers are moved to the grid-point while the shots are still at the surface. In terms of double focusing concept, the CFP gather can therefore be regarded as the output of half migration (Berkhout, 1997b).

The second removal process is focusing in emission. Similar to focusing in detection, focusing in emission synthesizes focused source arrays in such a way that they "illuminate" a single subsurface grid-point. The synthesis process transforms the CFP gathers into the prestack migration result. The migrated section may be interpreted as the output of a virtual physical experiment in which the response of a focused source array is measured by a focused receiver array. If the measurement is situated in the same grid-point, the migration process is called confocal version. This version introduces angle-averaged reflectivity information.

Conversely, if the measurement of a focused source array by a focused receiver array is performed in the different grid-point, the migration process is called bifocal version. The bifocal version provides angle-dependent reflectivity information of the selected grid-point within local seismic bandwidth. The angle-dependent reflectivity information is estimated by considering the number of grid-points around the selected focus point, e.g., along the reflector, and is followed by a local linear Radon transformation (see Appendix D). A detailed discussion on the CFP theory is presented in Berkhout (1997a) and Berkhout (1997b).

### 3.3 Equal Traveltime Principle

As the output of the first removal step, the properties of the CFP gather are essential for detecting errors in the velocity model. For a correct focusing operator, the focused receiver array response of a selected grid-point in the CFP gather will show identical traveltimes as the focusing operator. The equal traveltime curvature between the focusing operator and the CFP gather is a consequence of one single step of the double focusing algorithm, which



removes the one-way propagation effects from the recorded data set. This property is called the equal traveltimes principle (Berkhout, 1997a).

The CFP gather plays a significant role in understanding the updating of the macro velocity model. If the macro velocity model is not correct, then the focusing operator will also be wrong. As a consequence, the traveltimes of the CFP gather will not be identical to the traveltimes of the focusing operator. Wrong information is then selected from the CFP gather. By calculating the differential time shift between the CFP gather and the focusing operator, the focusing operator updating can be performed by choosing the intercept time exactly in the middle of the error of the focusing operator and the error of the CFP gather. Based on the comparison of the focusing operator and the related CFP gather, the CFP algorithm can be integrated with traveltimes analysis for velocity estimation. This process is called the inversion method.

### 3.4 Forward Model of Primary Reflections

The seismic experiment can be described mathematically and physically using a forward model. The clear way to illustrate a forward model is the WRW model in which all modeling steps can be written in terms of matrices (Berkhout, 1982). In principle, the WRW model describes the process of the downgoing source wave field from the surface to a particular depth, the reflection at that depth, and the upgoing propagation from the reflector to the recording surface. van Barneveld (1998) and Berkhout (1997a) derived the relationship between the detected data  $\vec{P}(z_0)$  and the downgoing source wavefield  $\vec{S}^+(z_0)$ .

Figure 3.2 shows the WRW model with a downgoing source wave field  $\vec{S}^+(z_0)$  as the input of the schematic representation (after van Barneveld, 1998). Source matrix  $\vec{S}^+(z_0)$  contains the downgoing source wave field at surface  $z_0$  for all source positions. As a conventional notation, the positive  $z$ -direction, denoted with a "+", is pointing into the subsurface, whereas the negative  $z$ -direction, denoted with a "-", is pointing into the surface.

In addition, the calculation of the downgoing wave field at a depth level of  $z_m$  is performed by applying a downward extrapolation matrix  $W^+(z_m, z_0)$  as follows:

$$\vec{P}^+(z_m) = W^+(z_m, z_0)\vec{S}^+(z_0) \quad (3.1)$$

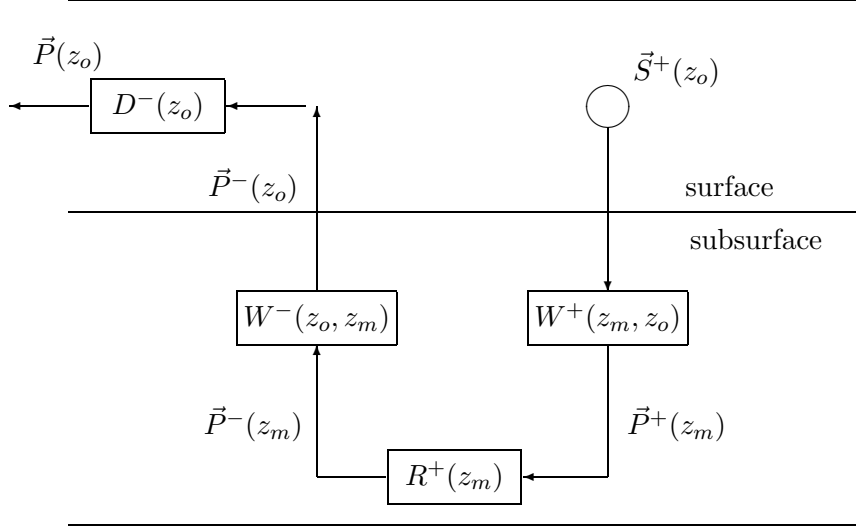


**Figure 3.2.** The WRW model describes the wave field propagation from source to receiver (after Barneveld 1998).

The physical condition of the subsurface governs the extrapolation matrix  $W^+(z_m, z_0)$ . If the downgoing wave field propagation hits an interface at a depth level of  $z_m$ , the part of its energy will be reflected, then

$$\vec{P}^-(z_m) = \mathbf{R}^+(z_m)\vec{P}^+(z_m) \quad (3.2)$$

$\mathbf{R}^+(z_m)$  represents the reflection operator at a depth level of  $z_m$ . By considering the deeper interface below  $z_m$ , equation (3.2) becomes

$$\begin{aligned} \vec{P}^-(z_m) &= \sum_{n=m}^M W^-(z_m, z_n)\mathbf{R}^+(z_n)W^+(z_n, z_m)\vec{P}^+(z_m) \\ &= \mathbf{X}(z_m, z_m)\vec{P}^+(z_m) \end{aligned} \quad (3.3)$$

The reflection response from a depth level of  $z_m$ , which is assumed as a deepest level, is represented by  $\mathbf{X}(z_m, z_m)$ . Generally  $\mathbf{X}(z_m, z_m)$  is formulated as a summation of reflection response of each interface.

$$\begin{aligned}
\vec{\mathbf{X}}(z_m, z_m) &= \sum_{n=m}^M W^-(z_m, z_n) \mathbf{R}^+(z_n) W^+(z_n, z_m) \\
&= \mathbf{R}^+(z_m) + \sum_{n=m+1}^M W^-(z_m, z_n) \mathbf{R}^+(z_n) W^+(z_n, z_m)
\end{aligned} \tag{3.4}$$

Equation (3.4) indicates that the reflection response will become  $\mathbf{R}^+(z_m)$  in case that there is no interface below a depth level of  $z_m$ . Thereafter, the reflected wave field is now propagated from the reflector to the surface by the propagation matrix  $W^-(z_0, z_m)$  resulting in

$$\vec{P}^-(z_0) = W^-(z_0, z_m) \vec{P}^-(z_m) \tag{3.5}$$

The composition operator  $\mathbf{D}^-(z_0)$  transforms the up-going reflected wave field,  $\vec{P}^-(z_0)$ , to the detected wave field as follows

$$\vec{P}(z_0) = \mathbf{D}^-(z_0) \vec{P}^-(z_0) \tag{3.6}$$

After surface-related multiple removal, the model can be simplified as follows:

$$\vec{P}^-(z_0) = \mathbf{X}(z_0, z_0) \vec{S}^+(z_0) \tag{3.7}$$

$\vec{S}^+(z_0)$  represents the downgoing source wave field,  $\vec{P}^-(z_0)$  denotes the up-going component of the measured response, and  $\mathbf{X}(z_0, z_0)$  describes the transfer function of the half space  $z > z_0$ , where

$$\mathbf{X}(z_0, z_0) = \sum_{n=m}^M W^-(z_0, z_m) \mathbf{R}^+(z_m) W^+(z_m, z_0) \tag{3.8}$$

Substitution of equation (3.8) into equation (3.7) and (3.6) yields the measured wave field,

$$\vec{P}(z_0) = \mathbf{D}^-(z_0) \sum_{m=1}^M [W^-(z_0, z_m) \mathbf{R}^+(z_m) W^+(z_m, z_0)] \vec{S}^+(z_0) \tag{3.9}$$

Equation (3.9) represents the total detected wave fields as the function of a source wave field. The related columns of data matrix  $\vec{P}(z_0)$  define the resulting upgoing wave fields, which are measured at the receivers.  $\mathbf{D}^-(z_0)$  is a detector matrix in which its row

describes the operator for one receiver position. The columns of  $W^-(z_0, z_m)$  and the rows of  $W^+(z_m, z_0)$  define primary propagation operators for downgoing and upgoing wave fields, respectively.  $\mathbf{R}^+(z_m)$  defines the reflections operators for the incident wave fields at depth level  $z$ .

### 3.5 Principle of Amplitude-Preserving Migration

The forward modeling describes the wave field propagation from sources at surface via depth point to receivers, generating seismic data. The migration process is an inverse modeling procedure that can be formulated as a numerical process to estimate the reflectivity properties of the subsurface by removing the acquisition and propagation effects from seismic data.

In principle, the AP migration is formulated using the following integral form:

$$\mathbf{R}(z_m) = \int_z \int_s \int_r \Omega(x_s, x_r) \vec{F}^\dagger(z_m, z_0) \mathbf{P}(z_0) \vec{F}^\dagger(z_0, z_m) dx_r dx_s dz \quad (3.10)$$

$\vec{F}^\dagger(z_m, z_0)$  and  $\vec{F}^\dagger(z_0, z_m)$  represent the downgoing and the upgoing operators.  $\mathbf{P}(z_0)$  is the detected wavefield at the surface, which is formulated in equation (3.9). In this equation,  $\Omega(x_s, x_r)$  is the weight function that is used to preserve amplitudes. The weight function is a function of source location ( $x_s$ ), receiver location ( $x_r$ ), and depth point coordinates. The detailed weight function is discussed later on in this section.  $z_0$  and  $z_m$  indicate the surface and the depth position.

Since the numerical process is conducted in the discrete form, the integration along the vertical  $z$ , source  $s$ , and receivers  $r$  coordinates become summations. The multidimensional integral operators become the matrix operators. The discrete version of equation (3.10) can then be written as:

$$\mathbf{R}(z_m) = \sum_z \sum_s \sum_r \Omega(x_s, x_r) \vec{F}^\dagger(z_m, z_0) \mathbf{P}(z_0) \vec{F}^\dagger(z_0, z_m) \quad (3.11)$$

In addition, the double focusing approach is applied to remove the propagation parts from the seismic data. The removal process describes the mathematical operation of the three matrices  $\vec{F}^\dagger(z_m, z_0) \mathbf{P}(z_0) \vec{F}^\dagger(z_0, z_m)$  of equation (3.11), which is split in two consecutive focusing steps.

### 3.5.1 First Focusing Step

The forward model for one seismic experiment, which is formulated in Equation (3.9), includes a combination of several depth points. In the case for a particular depth point, then the summation sign can be omitted and equation (3.9) can be simplified by assuming  $\mathbf{D}^-(z_0)$  and  $\vec{S}^+(z_0)$  are known, yielding

$$\mathbf{P}(z_0) = W^-(z_0, z_m)\mathbf{R}^+(z_m)W^+(z_m, z_0) \quad (3.12)$$

In order to extract  $\mathbf{R}^+(z_m)$ , the propagation matrices  $W^-$  and  $W^+$  must be removed. In the first focusing step, the up-going part, which is the left part of the right hand side of equation (3.12), is removed. This means that the CFP gather in detection is generated. To create the CFP gathers the focusing operator  $\vec{F}_j^\dagger(z_m, z_0)$ , which is acting at the receiver position at the surface, must be constructed.

$$\vec{F}_j^\dagger(z_m, z_0) = [W^-(z_0, z_m)]^{-1} \quad (3.13)$$

Equation (3.13) describes the synthesis operator for focusing in detection in which the focus point is located at  $(x_j, z_m)$ . The resulting CFP gather is

$$\vec{F}_j^\dagger(z_m, z_0)\mathbf{P}(z_0) = \vec{P}_j^\dagger(z_m, z_0) = \vec{\mathbf{R}}_j^+(z_m)W^+(z_m, z_0) \quad (3.14)$$

In case the reflector has an angle-independent reflection coefficients,  $\vec{\mathbf{R}}_j^+(z_m)$  can be represented by a weighted unit matrix  $r_m I$

$$\vec{P}_j^\dagger(z_m, z_0) = \vec{\mathbf{R}}_j^+(z_m)W^+(z_m, z_0) = r_m W^+(z_m, z_0) \quad (3.15)$$

The following identity is shown by a homogeneous medium

$$W^-(z_0, z_m) = W^+(z_m, z_0) \quad (3.16)$$

According to Wapenaar and Grimbergen (1996) the relation between a homogeneous and a weak inhomogeneous medium is obtained:

$$[W^-(z_0, z_m)]^{-1} \approx [W^+(z_m, z_0)]^* \quad (3.17)$$

Substituting equation (3.17) into equation (3.13), this yields:

$$\vec{F}_j^\dagger(z_m, z_0) \approx [W^+(z_m, z_0)]^* \quad (3.18)$$

Here, the CFP gather has the same traveltimes as the traveltimes of the focusing operator. This is called the equal traveltimes principle (Berkhout, 1997a).

### 3.5.2 Second Focusing Step

The second focusing, which is focusing in emission, can be carried out by applying the operator

$$\vec{F}_k^\dagger(z_0, z_m) = [W^+(z_m, z_0)]^{-1} \quad (3.19)$$

to the CFP gather of equation (3.14), resulting in:

$$\begin{aligned} \vec{P}_{jk}(z_m) &= \vec{F}_j^\dagger(z_m, z_0) \vec{P}(z_0) \vec{F}_k^\dagger(z_0, z_m) \\ &= \vec{R}_{jk}^+(z_m) \end{aligned} \quad (3.20)$$

Equation (3.20) shows the result of the double focusing. If the detector-related focus point is equal to the source-related focus point, i.e.,  $j = k$ , then the migration result represents angle-averaged reflectivity information. The migration process is called confocal version. In contrast, if a lateral shift between source related focus point and the receiver related focus point, i.e.,  $j \neq k$ , is included, then the migration process is called bifocal version. The migration result of bifocal version defines the angle-dependent reflection property of the grid-point.

Similar to focusing in detection, the equal traveltimes principle can be exhibited by focusing in emission. Application of focusing in emission to the data set yielding

$$\vec{F}_k^\dagger(z_0, z_m) \mathbf{P}(z_0) = \vec{P}_k^\dagger(z_0, z_m) = \vec{R}_k^+(z_m) W^-(z_0, z_m) \quad (3.21)$$

and similar to the first focusing step, if  $\mathbf{R}^+(z_m)$  is weighted by unit matrix  $r_m I$ , then

$$\vec{P}_k^\dagger(z_0, z_m) = \vec{R}_k^+(z_m) W^-(z_0, z_m) = r_m W^-(z_0, z_m) \quad (3.22)$$

Equation (3.22) describes the CFP gather for focusing in emission in which the focus point is at  $(x_k, z_m)$ . The same relationship as equation (3.17) for homogeneous and weak inhomogeneous media is gained:

$$[W^+(z_m, z_0)]^{-1} \approx [W^-(z_0, z_m)]^* \quad (3.23)$$

Substitution of equation (3.23) to equation (3.19) yields:

$$\vec{F}_k^\dagger(z_0, z_m) \approx [W^-(z_0, z_m)]^* \quad (3.24)$$

Equation (3.24) also describes the equal travelttime principle. Therefore, the order of the focusing step can be chosen arbitrarily, since both focusing steps produce the same result.

### 3.5.3 Amplitude-Preserving Weight Functions

The ability to preserve the amplitudes of reflection coefficients, which will be used in subsequent AVA analysis, is one of the important aspects of the migration method. The amplitude should be handled correctly during the migration process, otherwise the errors occurring in the amplitude caused by the migration process are not trustworthy. Therefore, it is essential to pay close attention to the preservation of amplitude during the migration process.

Preserved-amplitude, particularly amplitude-preserving imaging, remains an extremely fascinating concept amongst geophysicists. There are various approximations to define the concept of preserved-amplitude. A very clear definition of preserved-amplitude is the reflected seismic signal, from which the geometrical spreading effect is removed (Hubral, 2001) or in other words, the compensation for this effect is applied to preserve the amplitude, which is given in terms of the weight function. A modified weighted diffraction stack migration approximation that is commonly based on ray theory has recently been derived by various authors (Hanitzsch et al., 1994; Hubral et al., 1991).

The principle of the developed AP migration is the application of an appropriate weight to the data before diffraction stacking, which automatically removes geometrical spreading effects of the primary reflection during the imaging process. The phase shift effects on the signature due to the summation of diffraction stacks are also considered to permit the

extraction of the source signal. The weighted diffraction stack is performed in every grid-point of the target zone within the subsurface. For this purpose, the following weight, which is approximated to 2D weight for the common shot configuration in terms of Green's function amplitudes, is applied (Hanitzsch et al., 1994):

$$\Omega(x_s, x_r) = \frac{1}{\sqrt{2\pi}} \frac{\cos\theta_G}{v_G} \frac{A_{GM}}{A_{SM}} \quad (3.25)$$

Here,  $A_{SM}$  and  $A_{GM}$  are the Green's function amplitudes of the rays  $SM$  and  $GM$  ( $S$  is source location,  $G$  is receiver location and  $M$  is the specified grid-point),  $\theta_G$  is the angle between the normal of the surface and the ray emerging at the receiver, and  $v_G$  is the velocity at the receiver. However, it is implemented in such a way that the AP migration method is independent of the modeling algorithms. Thus, all required quantities for amplitude-preserving weight migration are estimated from the seismogram operator. The term  $\frac{A_{GM}}{A_{SM}}$  on the right side of equation (3.25) is represented with the cross-correlation processes (between the seismic data and the seismogram operator), which is carried out in two focusing steps and followed by the zero-lag (temporal autocorrelation of the seismogram operator) division in the second focusing step. The cosine function is then estimated by applying a local slant-stack to the seismogram operator.

In addition, the phase shift effects on the signature due to the summation of diffraction stacks are compensated to permit the extraction of the source signal. This compensation is carried out by applying a filter operation to the input data before stacking or afterwards to the summation result. The filter operation consists of two steps, which are carried out simultaneously in the frequency domain. These are the computation of the analytic signal of the input data (complex seismic trace) and the application of the half time derivative. Since the migration process is performed in the complex frequency domain (see Appendix B), the filter operation may be easily implemented. This is one of the advantages of the analytic signal computation. Moreover, the imaginary part and the envelope of the complex image, which is essential to predict the correct reflector position, can be estimated.



### 3.6 General Scheme of the AP Migration

In general, the schematic flow of the AP migration, which is illustrated in Figure 3.3, consists of the following steps:

1. *Preparing input parameters.* As input parameters the AP migration requires the velocity model including the target zone that will be migrated and seismic data volume in the shot profile configuration.
2. *Generating the focusing operators.* The focusing operators are generated by the modeling program, which is separated from the AP migration program. In its implementation, the modeling program and the AP migration program are performed in parallel processing. Both are linked using SEG-Y input/output file. In this work, the focusing operators are computed by using the band limited Green's functions program, which is discussed in Chapter 2. The focusing operators are represented by a set of one-way traveltimes together with related amplitudes in the form of a seismogram.
3. *Estimating the parameters of the weight function.* Those parameters are the cosine function of the emerging angle of ray at the receiver and the auto-correlation of the focusing operator.
4. *Applying the first focusing step.* Using the focusing operator, the AP migration method transforms each shot record into one event of grid-point response that is positioned at the source position. This process is performed by cross-correlating each shot record with the focusing operator and followed by applying the weight function (i.e., cosine function) and stacking to produce one trace. Repeating the focusing process for all shot records that are covered by the aperture. This process yields the CFP gather. The main information in the CFP gathers is given by the focus-point response. For a correct macro velocity model, the focusing operator and the reflection energy in the focus-point response will have equal traveltimes (principle of equal traveltime).
5. *Applying the second focusing step.* This process is carried out by cross-correlating the CFP gather with the focusing operator. Particular in the bifocal version, the focusing operator, which is used in the second cross-correlation, is chosen around the

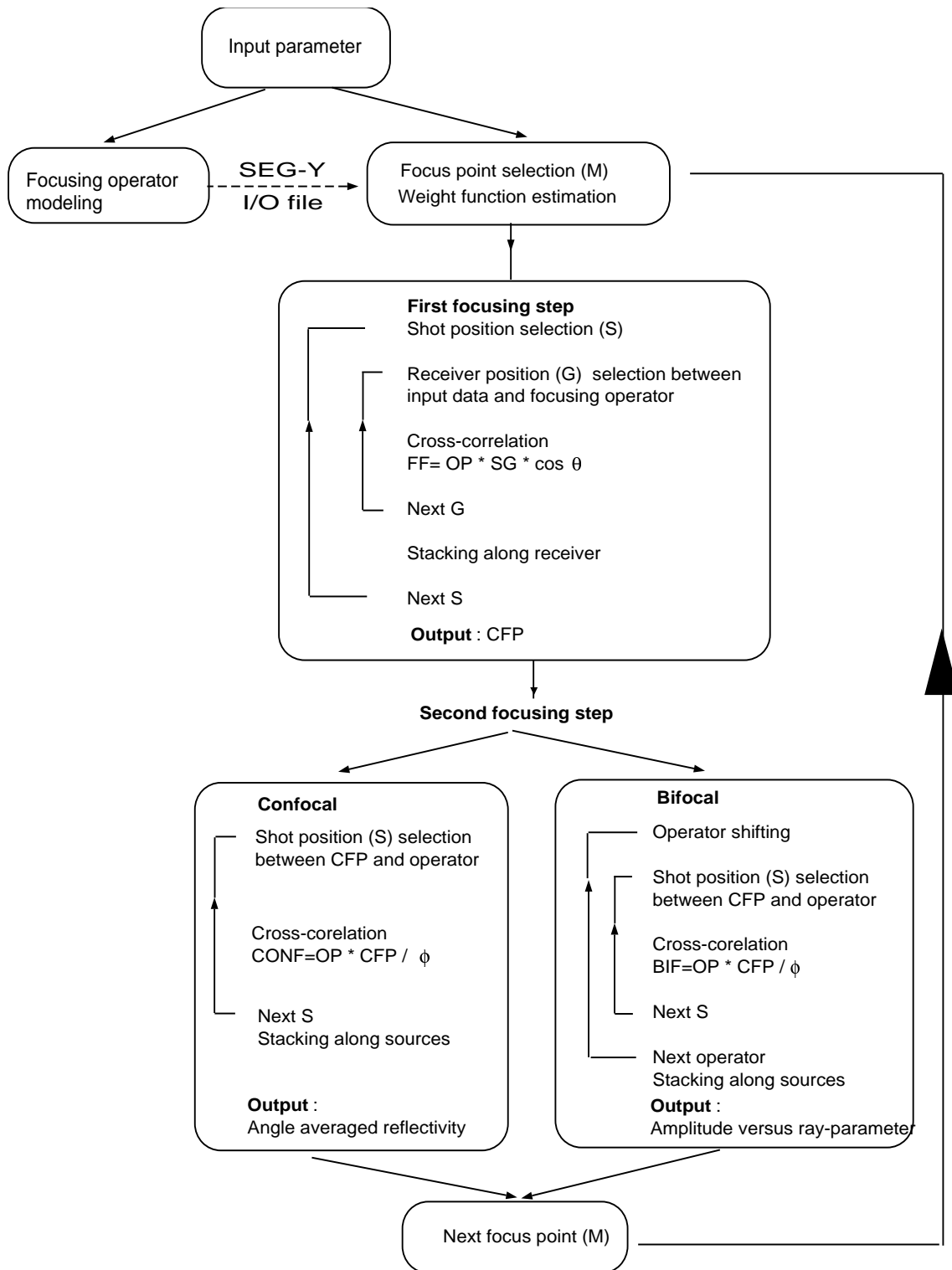


**Figure 3.3.** The schematic flow of the AP migration.

first focusing operator. For the confocal version, the same focusing operator as used in the first cross-correlation is used in the second cross-correlation. In order to correct for the geometrical spreading effects, the second cross-correlation step is followed with a division by the zero-lag (temporal auto-correlation of the focusing operator) and a filter operation.

6. *Applying the confocal version.* In order to produce the structural image, the angle-averaged reflection coefficients for each grid-point in a specific lateral distance, which are the result of the double focusing (at zero intercept time), are positioned at their corresponding position. This step results in a single-trace output. Repeating this step for the next lateral distance results in a zero offset section.
7. *Applying the bifocal version.* Note that the original output of the bifocal version are ray-parameter ( $p$ )-dependent reflectivity gathers. Angle-dependent reflectivity gathers are obtained by applying the postprocessing step, which will be discussed in Chapter 4. In order to produce  $p$ -dependent reflectivity gathers,  $p$ -dependent reflection coefficients for each grid-point in a specific lateral distance, which are the result of the Radon-transformed double focusing (at zero intercept time), are positioned at their corresponding position. This step produces the  $p$ -dependent reflectivity gather (multi-trace output). Repeating this step for the next lateral distance will produce  $p$ -dependent reflectivity gathers.

## Chapter 4

# Application of the AP Migration to Synthetic Data

### 4.1 Introduction

After having discussed the algorithm of the AP migration method, the method is now applied to synthetic data. Three synthetic data sets are prepared: marine multichannel seismic (MCS) reflection data, wide-angle seismic data and a realistic complex model (Marmousi data set). In principle, the differences between marine MCS and wide-angle seismic data originate from the acquisition geometry. The marine MCS data are acquired by deploying the streamer (groups of receivers) and the source (e.g., airgun) at the same depth level. Airguns are deployed behind the seismic vessel and generate a seismic signal by forcing highly pressurized air into the water. Receivers are towed behind the ship in long streamers up to several kilometers in length (Kessinger, 2002; Jones E., 1999). The wide-angle seismic data are acquired by deploying several receivers units (OBH) and the source at different depth levels. OBH instruments are lowered to the sea floor and mounted with a steel pipe (weight) at a fixed position. The seismic source remains close to water surface and is moved with respect to the sea floor with equidistant shooting (Flueh and Fisher, 1996).

This chapter demonstrates the AP migration results from the three synthetic data sets. The migration example on simple generic model validates the AP migration method and the application to OBH synthetic data demonstrates its flexibility to special seismic data acquisition. In addition, to illustrate the potential of the AP migration to complex media, the Marmousi data set is migrated using a variety of input parameters such as: with and without compensation to geometrical spreading effects, the use of an approximate velocity model and the use of sparse-shot geometries. Special analysis to the effect of the wavelet

frequency, which is used in constructing the focusing operator, on the migration result is performed to determine the appropriate wavelet frequency with respect to the frequency content of the seismic input data. For comparison to other migration methods, the Marmousi data set is migrated using standard Kirchhoff migration.

## 4.2 Marine MCS Synthetic Data

MCS reflection profiling is an outstanding technology for imaging the Earth's subsurface. It is used in both applied and fundamental fields such as hydrocarbon exploration, environmental imaging, sedimentary basin research, and the study of crustal tectonics. The marine MCS synthetic data, which is used for testing the AP migration method, are generated by simulating a marine MCS experiment.

The subsequent steps of the AP migration scheme, which involve the focusing operator construction, the first focusing step, and the second focusing step, are demonstrated by using synthetic data generated from a three-layer velocity model with a dipping reflector. The equal traveltimes principle, which can be used to check the focusing operator, is also presented.

### 4.2.1 Velocity Model

The model consists of three layers with a dipping reflector at the first interface. This model is used to show how well the AP migration method compensates the geometrical spreading effects, particularly for the dipping reflector. Moreover, this model is used to get a clear understanding of the subsequent steps of the AP migration method. The size of the model ranges from 0 m to 30000 m in the horizontal direction, and from 0 m to 5000 m in the depth direction. The velocity model is shown in Figure 4.1. The dipping reflector is a line defined through the point ( $x=13200$  m,  $z=2500$  m) and ( $x=17500$  m,  $z=1800$  m) with a dip angle of -10 degrees. As a dip sign convention, from left to right, events with down-dip to the right are assigned positive dip, while events with up-dip to the right are assigned negative dip. The velocities of the model are 1500 m/s, 2000 m/s and 1750 m/s for first, second, and third layer, respectively. The synthetic data for this model was modeled using a ray-tracing modeling algorithm. The acquisition configuration consists of 120 receivers

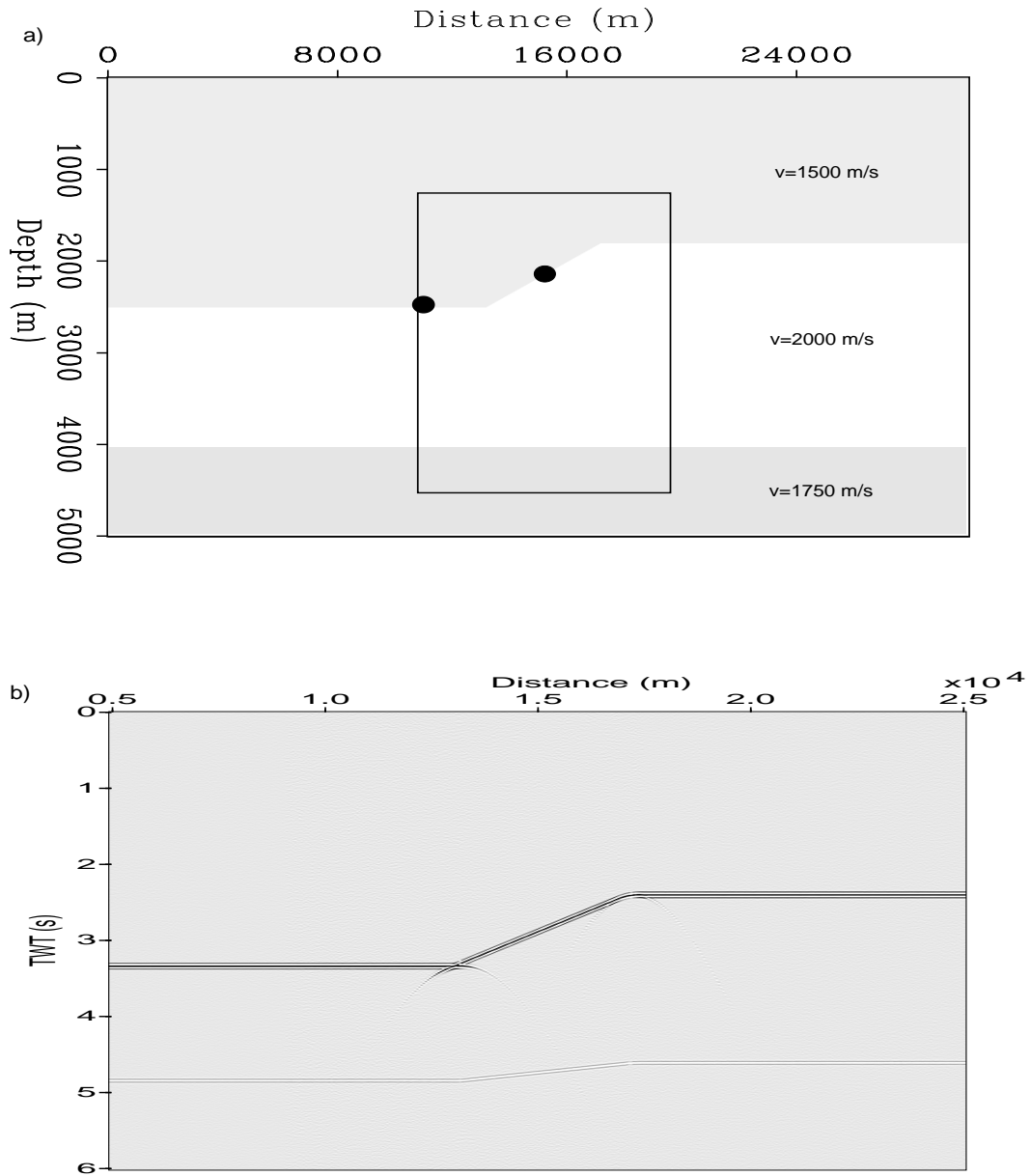


**Figure 4.1.** Subsurface velocity model a) consists of three velocity layers with a dipping reflector at the first reflector and its corresponding near offset section b), which is recorded by shots from 5000 m to 25000 m. Two solid circles represent the focus point in which their angle-dependent reflectivity gathers are analyzed.

that are laid out with a spacing of 25 m. The position of the source and the receivers are assumed to be at the same level close to the water surface. The seismic source is moved from a lateral distance of 5000 m to 30000 m with increment of 50 m.

To get an idea of the imaging procedure, the migration process of the focus point at a lateral distance of 10000 m is demonstrated. The corresponding shot record, which is located in the same lateral distance as the focus point, is represented in Figure 4.2a. In order to investigate the effects of a dipping reflector on the migrated angle-dependent reflectivity gather, the bifocal version of the AP migration is also applied to the focus point at a lateral distance of 15000 m. The subsequent steps to arrive at the desired CFP gather and angle-dependent reflectivity gather, which are discussed in Chapter 3, will be described in the following.

#### 4.2.2 Focusing Operator

Based on the one-way approach, the removal of the propagation effects is accomplished by applying the inverse of these wave field propagators to the seismic data. These inverse propagators are approximated by generating the focusing operators; the down-going and the up-going operator, for each grid-point in the subsurface.

For practical application, the down-going and the up-going operators are computed by downward propagating the wave field from a source at the surface to all grid-points in the subsurface. Note that the wave field propagation is calculated using the band limited Green's function as described in Chapter 2. For a specific lateral distance, once downward propagating the wave field, the three modeling outputs (traveltime, amplitude, and phase map) are obtained. Based on these modeling outputs, the down-going operators at every grid-point for this specific lateral distance are constructed. In addition, the corresponding up-going operators are constructed by resorting the wave field data from each shot. Therefore, their amplitudes correspond to the downward propagation wave field. The construction of the focusing operators is appropriate to the implementation of the weight function, which is described in Chapter 3.

The focusing operator for the focus point (at  $x=10000$  m,  $z=2500$  m) is shown in Figure 4.2b. The focus point yields a single-valued operator because the velocity model is constant.

The down-going operator and the up-going operator are identical, since the focus point is located on a horizontal reflector. The operator consists of 321 traces spaced at 25 m intervals, which covers to total of 8000 m.

### 4.2.3 First Focusing Step

After obtaining the focusing operator, the first focusing step is now applied. The receivers are downward extrapolated to the focus point. The result of this step will yield the CFP gather for focusing in detection. Since the order of focusing steps can be chosen arbitrarily, therefore, to conform with the output from the modeling program, the focusing in detection is applied in the first focusing step. The physical meaning of this step is that all receivers "listen" only to one grid-point in the subsurface. This means that each shot record is transformed to one event of the focus point response. The result of this step is the positioning of a virtual receiver on a chosen grid-point in the subsurface.

To produce the CFP gather for focusing in detection, each trace of the focusing operator is cross-correlated with the trace of the shot gather that has the same lateral position. The process is followed by applying the weight function and stacking the cross-correlation result along all traces in the shot gather. Special normalization to preserve the stacked amplitude is performed. The result of the first focusing step transforms one shot gather to one trace in the CFP gather. Repeating this procedure with the same operator to all available shot gathers, which are covered by the focusing operator aperture, yields the CFP gather.

Figure 4.2c shows the CFP gather, which is synthesized using the focusing operator from the focus point (at  $x=10000$  m,  $z=2500$  m). From this figure it can be noticed that the resulting CFP gather is identical to the focusing operator in terms of traveltimes. This means that the equal traveltimes principle is obeyed. This is obvious because the same velocity model is used for modeling the shot gathers and the focusing operator. However, the CFP gather shows only the right side of the aperture. This is because the synthetic data set is simulated using marine seismic acquisition, where the receivers are laid out on the left side of the source (end-off configuration) and the vessel moves to the right. Thereby, all shots in the left side of the focus point do not illuminate the focus point. The aperture of the CFP gather is only produced in the right side of the focus point position. The clear



illustration can be drawn using ray paths in illuminating the subsurface points. In contrast, a data set which is created using a split spread configuration, would produce the complete aperture of the CFP gather.

#### 4.2.4 Second Focusing Step

As described in Chapter 3, based on the operation of the second focusing step, there are two types of the AP migration version: confocal and bifocal. The confocal migration means that the AP migration synthesizes the CFP gathers and is followed by zero-shift cross-correlation. In the confocal version, only the operator that was used in the first focusing step is needed, while in the bifocal version, the AP migration synthesizes the CFP gathers, followed by shifted cross-correlation. This means that besides the operator that was used in the first focusing step, additional operators surrounding the focus point are needed.

Basically the equal traveltimes principle prompts a new solution to the important problem of velocity model estimation. It can be carried out by applying the operator updating in the intermediate step between the first and the second focusing step. Since the velocity estimation is beyond the scope of this study, the AP migration does not attempt this process. This could be a worthy topic for further study. The AP migration assumes that the focusing operators are generated using the correct velocity model. The velocity model can be estimated using existing software packages (e.g., MIGPACK, SEISMOS).

##### 4.2.4.1 Bifocal Version

In the bifocal version, the CFP gather from the specific focus point ( $x=10000$  m,  $z=2500$  m) is cross-correlated with the shifted focusing operators around the focus point. The result of the bifocal version simulates a virtual response of a virtual source and a virtual receiver that are not in the same position. A number of grid-points for the second focusing step is chosen along the reflector. In this example, the focusing operator is shifted around the focus point ranging from  $x=9500$  m to  $x=10500$  m with a spacing distance of 25 m. The resulting so-called grid-point gather defines angle-dependent reflection property of the focus point within the local seismic (temporal, spatial) bandwidth.

Figure 4.2d illustrates the result of the bifocal version for the specific focus point

( $x=10000$  m,  $z=2500$  m). As a consequence of the asymmetric CFP gather, the asymmetric grid-point gather with a positive diagonal only is obtained. This means that the rayparameter is positive. Therefore, the reflectivity distribution is only produced in the positive rayparameter axis.

The reflectivity information around zero time as a shifting function is transformed to rayparameter function by a linear Radon transformation. The detailed discussion about this process is presented in Appendix D. Figure 4.3a shows the rayparameter domain, which contains the reflectivity information around zero time. Thereafter, they are positioned in the same depth as the focus point to arrive at the migrated depth section. By repeating this procedure to all focus points throughout the subsurface, rayparameter-dependent reflectivity information is obtained. The final result of the bifocal version is the rayparameter-dependent reflectivity gather. Figure 4.3b shows the rayparameter-dependent reflectivity gather resulting from a lateral distance of 10000 m.

#### 4.2.4.2 Angle-Dependent Reflectivity

In order to get the angle-dependent reflectivity gather, the rayparameter-dependent reflectivity gather resulting from the bifocal version is transformed to angle-domain using the following equation based on Snell's law:

$$p = \sin \alpha / v \quad (4.1)$$

where  $\alpha$  is the angle of incidence and  $v$  is velocity at the subsurface grid-point. The transformation is carried out for each depth sample based on the velocity model. However, the velocity model must be smooth enough to avoid a dramatic change of the event. The transformation result is the band limited angle-dependent reflection coefficients of the subsurface.

Figure 4.3c shows the angle-dependent reflectivity gather from a lateral distance of 10000 m. The picked amplitude, which is shown in Figure 4.3d, illustrates the amplitude response of the bifocal version image for the first and the second reflector. The amplitudes of the migrated image (crosses line) are in good agreement with the theoretical amplitudes (solid line), which are calculated using Zoeppritz' equations. The picked amplitudes introduce boundary effects, i.e., diminishing amplitudes at near angle and far angle, caused by the

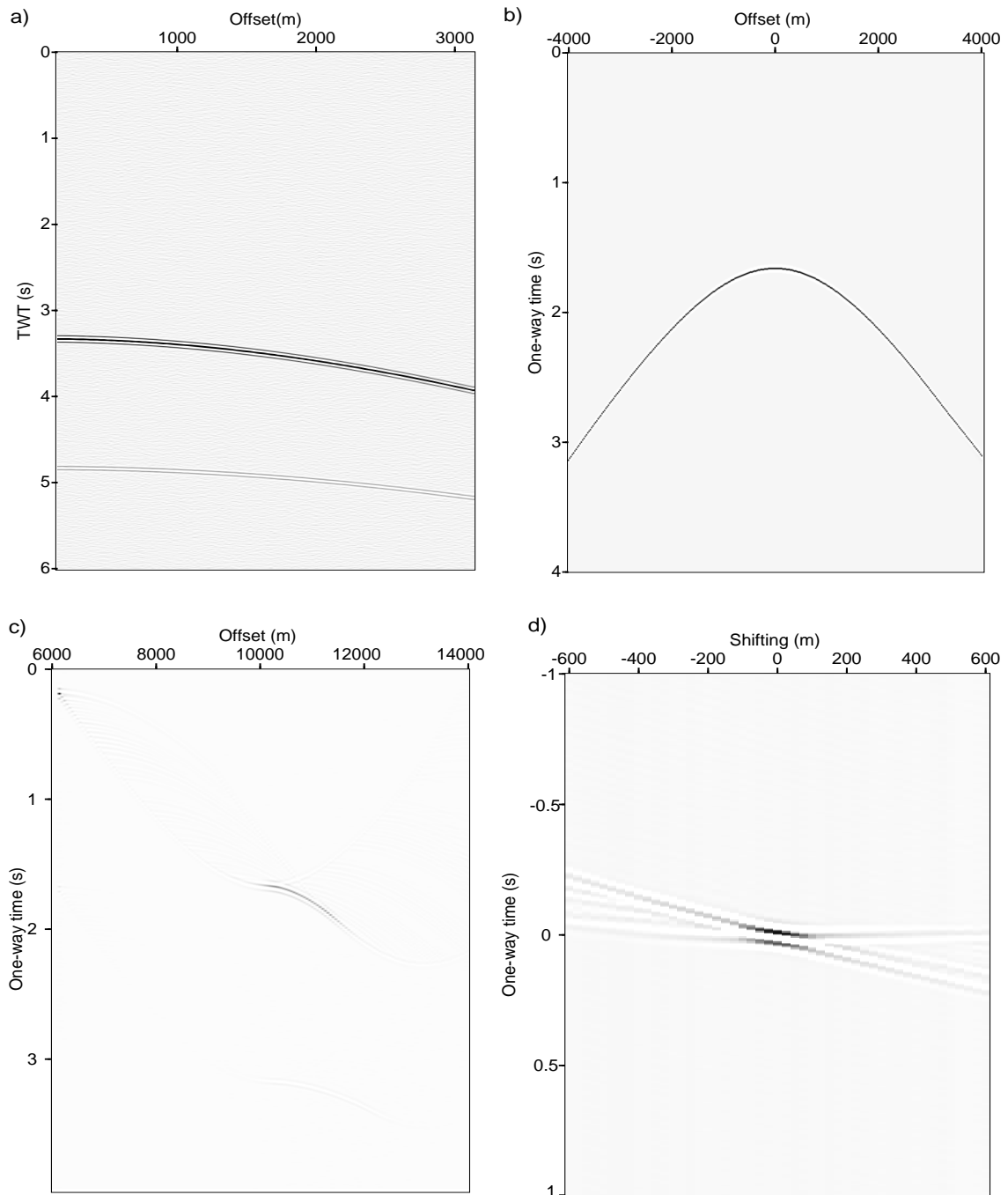


**Figure 4.2.** Illustration of the AP imaging for a specific focus point ( $x=10000$  m,  $z=2500$  m). a) Shot gather. b) Focusing operator. c) The result of the first focusing step. d) The result of the second focusing step.

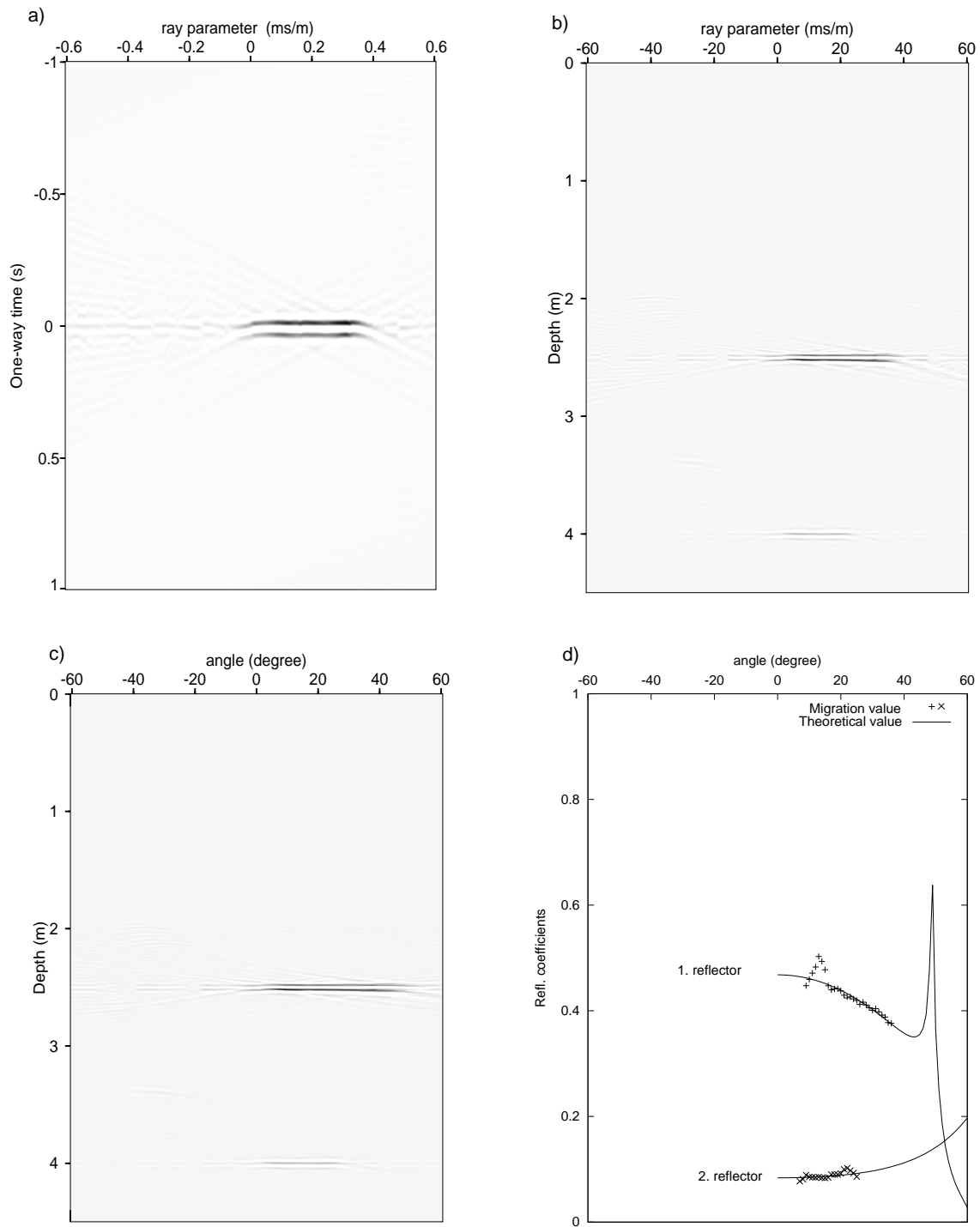


**Figure 4.3.** The bifocal version of the AP migration: a) Reflection coefficients around zero time in the rayparameter domain. b) Rayparameter-dependent reflectivity gather. c) Angle-dependent reflectivity gather. Both b) and c) are in the depth domain. d) Comparison of reflection coefficients obtained by the AP migration (crosses line) with theoretical values (solid line).

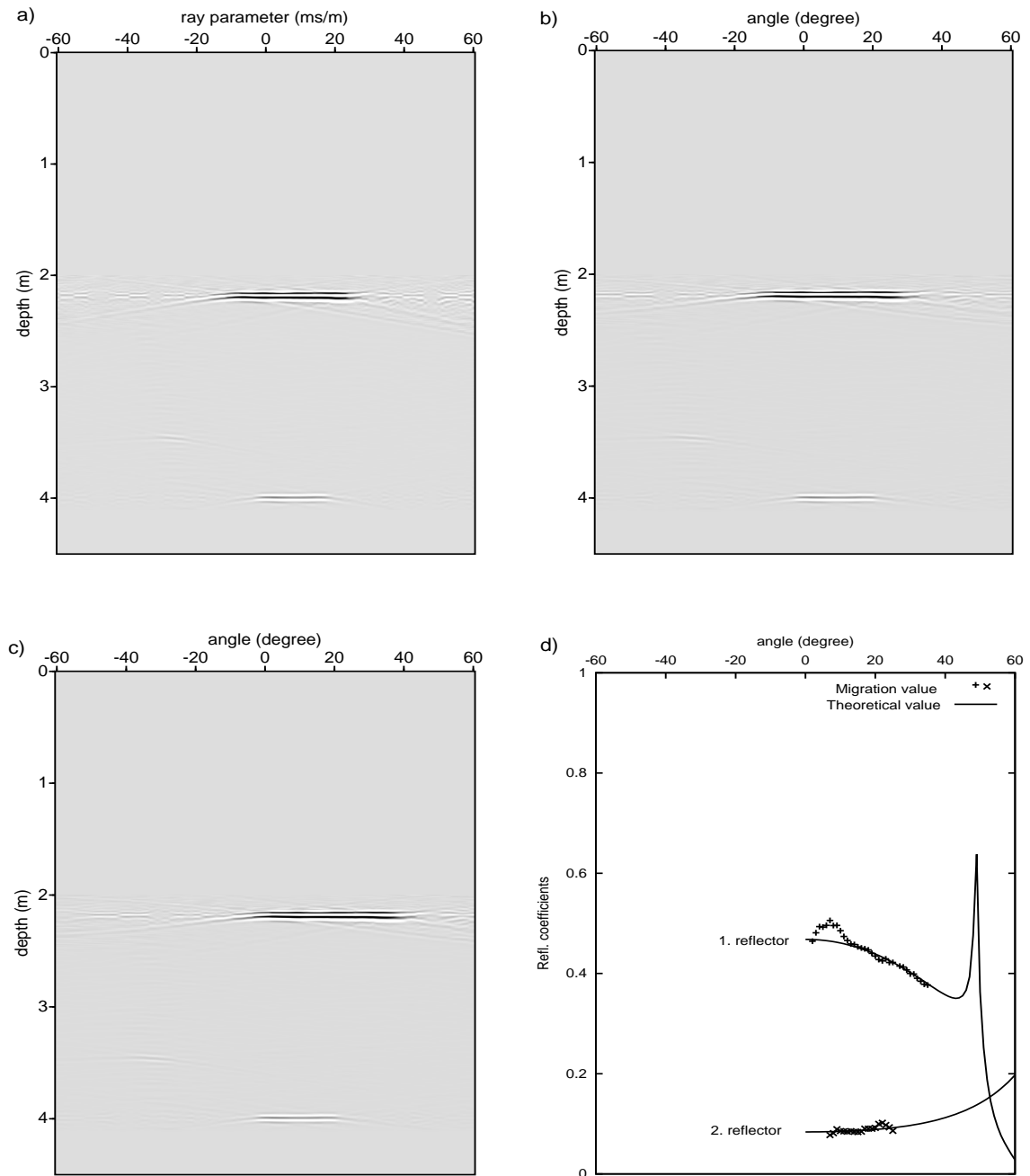


**Figure 4.4.** The migrated angle-dependent reflectivity gather at a lateral distance of 15000 m in which the first interface is a dipping reflector: a) Rayparameter-dependent reflectivity gather. b) Angle-dependent reflectivity gather before dip correction. c) Angle-dependent reflectivity gather after dip correction. d) Comparison of reflection coefficients obtained by the AP migration (crosses line) with theoretical values (solid line).

limited extent of the spread. Such effects are commonly found in the migrated image. For convenience in display, the picked amplitudes are only plotted in the effective ranges.

In addition, the migrated angle-dependent reflectivity gather on a dipping reflector is illustrated. In the following, the influence of the local dip-angle to the migrated amplitude distribution is demonstrated. Figure 4.4 shows the migrated image of the bifocal version for the model of Figure 4.1a at a lateral distance of 15000 m. The model displays that the first reflector is a dipping layer with a dip-angle of about -10 degrees. In the case a grid-point is situated on a dipping reflector, the local dip-angle will influence the amplitude distribution for this depth sample. Figure 4.4a illustrates the migrated image in the ray-parameter domain. The transformed image to the angle domain, which is an uncorrected angle-dependent reflectivity gather, is displayed in Figure 4.4b. The image shows that the amplitude distribution of the first reflector is shifted to the left side of about -10 degrees. The amplitude distribution of the second reflector is in a correct position, since the reflector is horizontal. The shift of the amplitude distribution corresponds to a local dip-angle. Therefore, local dip-angle information is required to move the amplitude distribution to its correct position. However, the dip correction may be performed as a post processing step in which local dip-angle information can also be estimated from the migrated image of the confocal version. The detailed discussion on the dip correction is presented in Chapter 5.

Figure 4.4c shows the angle-dependent reflectivity gather after dip correction. The amplitude distribution of the first reflector has been moved to its correct position. In principle, the local dip-angle has no influence on the traveltimes. Thereby, its effects do not deteriorate the amplitude, since the amplitudes are obtained by a cross-correlation process. Obviously, the picked amplitude of the corrected image shows a good agreement with the theoretical amplitude, which is illustrated in Figure 4.4d.

Finally, the AVA analysis may be performed on the migrated angle-dependent reflectivity gathers. The angle-dependent reflectivity information is more suitable for reservoir characterization than the amplitude versus offset information, particularly if the amplitude analysis is performed in the complex structures.

#### 4.2.4.3 Confocal Version

The zero shifting of the bifocal version, the center trace in Figure 4.2d, is the confocal result for the specific focus point ( $x=10000$ ,  $z=2500$ ). It contains only angle averaged reflectivity information of the focus point. The zero shifting trace acts as a double focus point and its amplitude is the result of a double stacking process (along the receiver and the source coordinate), which is preserved with the weight function. The confocal version yields the structural image in the depth section. Figure 4.5 shows the migrated image using a three-layer velocity model (Figure 4.1a). The image shows that all reflectors are clearly imaged, both the first and the second reflector. This means that the AP migration process succeeds in moving all events to their correct position. In addition, the diffraction effects on the zero offset section (Figure 4.1b) were completely removed. The AP migration is able to remove the diffraction effects by collapsing energy from diffractions back to their scatterer points.

Looking at to the amplitude responses of the confocal version (see Figure 4.5), it can be noticed that the amplitudes are constant along the first reflector, which is situated with the high step from its deep part ( $z=2500$  m) to the shallow part ( $z=1800$  m) through the dipping reflector. This result shows that the AP migration is able to preserve the amplitudes from geometrical spreading effects. For the second, horizontal reflector, the amplitudes are exactly constant.

### 4.3 Effect of Wavelet Frequency on the Migrated Image

It is interesting to observe the effect of the wavelet frequency, which is used in constructing the full waveform (synthetic seismogram) of the focusing operator, on the migration result. As described in Chapter 2, the focusing operator is built by convolving the calculated traveltime, amplitude, and phase with the zero phase Ricker wavelet. Thereby, the choice of the Ricker wavelet frequency is very important in order to preserve the frequency content of the input data on the migration result.

Ideally, the frequency of the chosen wavelet, which is used to construct the focusing operator, should be equal to the frequency content of the input seismic data (the reflection responses). The ideal forward modeling technique, such as the finite difference, involves the frequency-dependence in propagating the wave field. However, the method requires

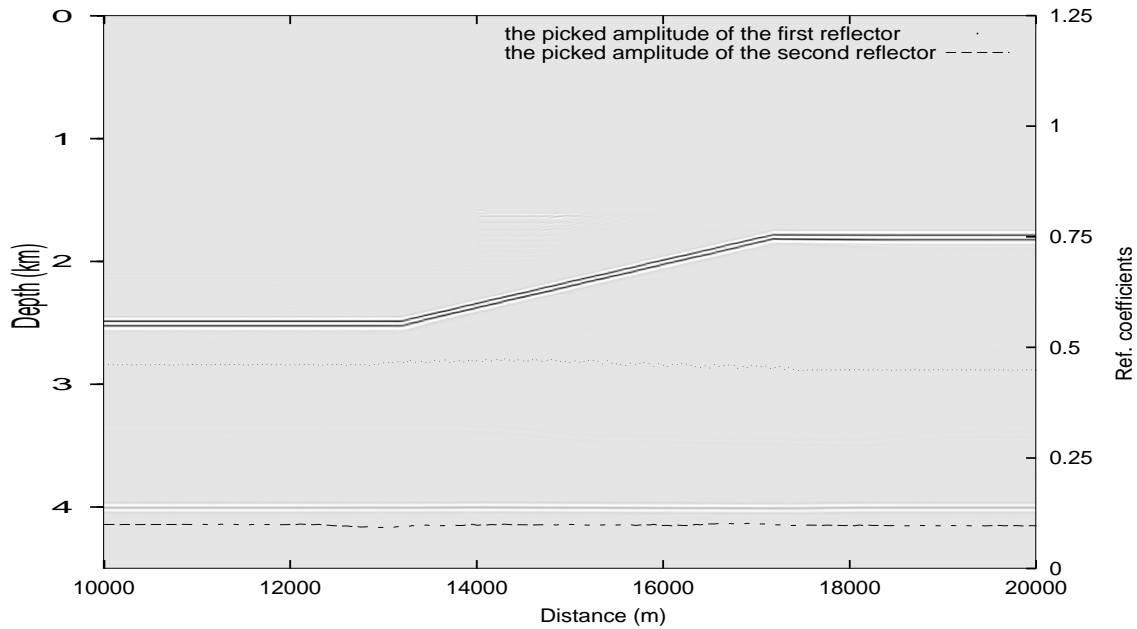


**Figure 4.5.** The confocal version of the AP migration. The amplitude responses are superimposed on the migrated section. The dotted line represents the amplitude responses of the first reflector and the dashed line represents the amplitude responses of the second reflector.

a fine grid-point of the macro model to produce accurate results. As a consequence, the computation cost will be very high. This factor is considered in the migration method. In contrast to the finite difference, the band limited Green's function algorithm allows us to define the frequency of the wave field independent of the subsurface grid-point.

This section will discuss the effect of the wavelet frequency of the focusing operator on the migration result. In principle, this effect can be considered as an effect of frequency filtering. The focusing operator with a certain frequency is assumed as a filter operator and its individual time samples are assumed as filter coefficients. The process described here is non-zero phase frequency filtering, meaning that it will modify the phase spectrum and amplitude of the input trace.

Various frequencies of the Ricker wavelet (5, 25, 50 Hertz and spike) are used to construct the focusing operator. The focusing operator with a specified frequency is then used to migrate the synthetic data. In this analysis, the simple MCS synthetic data, which is



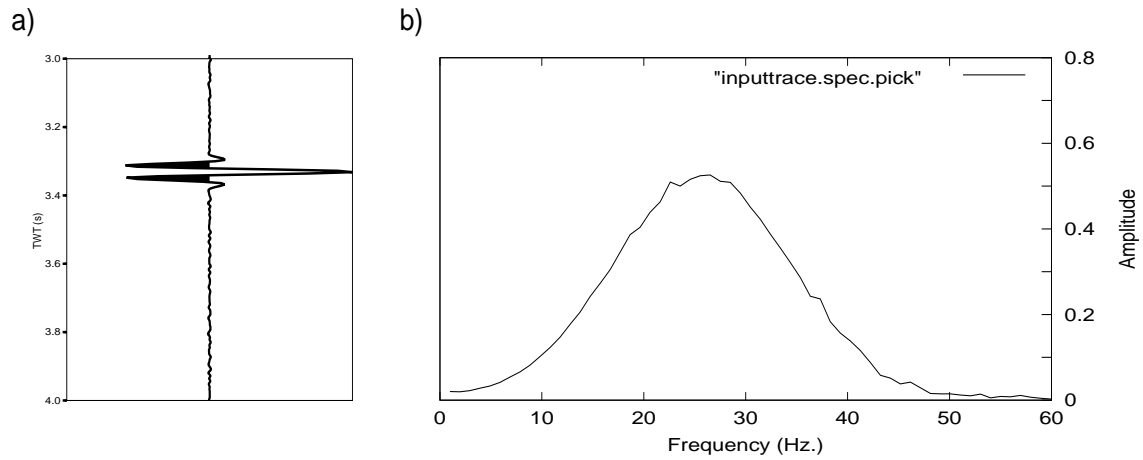


**Figure 4.6.** A trace of the MCS synthetic data and its respective amplitude spectra with a peak frequency of 25 Hertz.

generated with the zero phase Ricker wavelet of 25 Hertz, is used as input data to investigate the response of the migration result for different focusing operators. Figure 4.6 shows a trace of the MCS synthetic data and its respective amplitude spectra. This frequency bandwidth is considered as a reference to be compared to the frequency bandwidth of the migration result. From Figure 4.6b, it can be noticed that the peak frequency of the input data is exactly 25 Hertz and the frequency bandwidth is ranging from 0 to 50 Hertz.

Prior to discuss more details about the effect of the wavelet frequency, it is necessary to bear in mind the mathematical operation, which is carried out during the migration process. As discussed in Chapter 3, the mathematical operation used in the AP migration method consists of cross-correlation and addition (stacking). This operation is performed in the frequency domain. Therefore, the process will become a multiplication between the amplitude spectrum of the input seismic trace and the amplitude of the focusing operator (filter operator).

The discussion is now started with the spike operator. Figure 4.7a presents a spike trace, only one amplitude exists, no convolution is performed. Comparison of the frequency bandwidth between the input data (reference) and the migration result is superimposed in Figure 4.7b. Note that this analysis considers the frequency bandwidth and the peak frequency. The amplitude spectra are equalized. The preservation of amplitude has

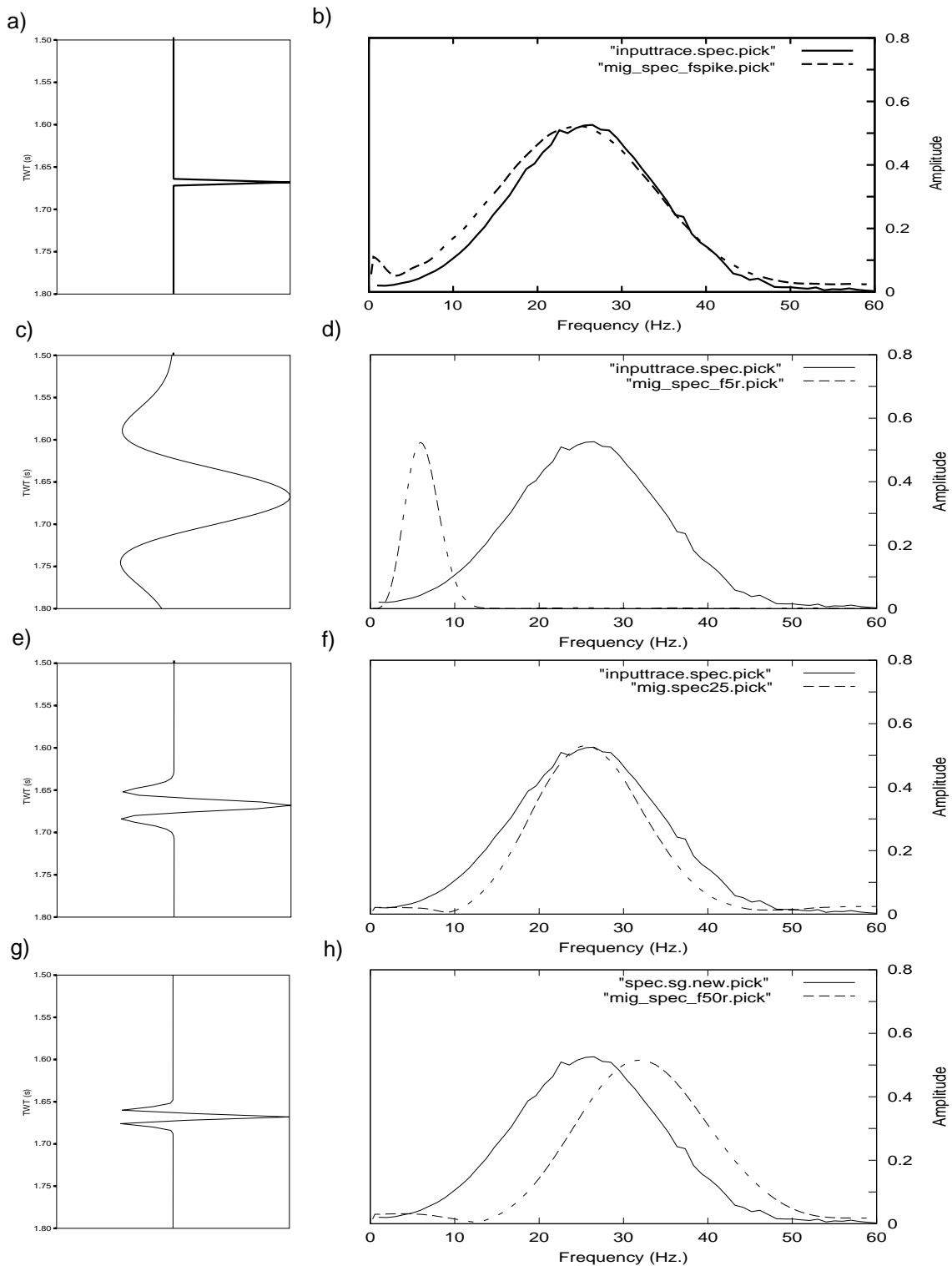


**Figure 4.7.** The effect of the wavelet frequency on the migration result: a) Spike operator trace. b) Comparison of the frequency bandwidth between the input trace (solid line) and the migrated trace (dashed line) from spike operator. c), e) and g) present the operator trace with Ricker wavelet of 5, 25 and 50 Hz, respectively, and d) f) and h) present the comparison of the frequency bandwidth between the input trace (solid line) and the migrated trace (dashed line) from Ricker wavelet of 5, 25 and 50 Hz, respectively.

been discussed in Chapter 3. Figure 4.7b shows that the frequency bandwidth of the input data (solid line) and the frequency bandwidth of the migration result (dashed line) is nearly identical with a peak frequency of 25 Hertz. This result can be easily explained because the spike operator in the time domain is a constant factor in the frequency domain. Therefore, the migration process does not modify the frequency band but merely band limits its amplitude spectrum.

The effect of low frequency is presented in Figure 4.7c. The Ricker wavelet with a frequency of 5 Hertz is used to construct the focusing operator. Figure 4.7d shows that the frequency bandwidth of the migration result (dashed line) is shifted to the low frequency end with the peak frequency of around 5 Hertz. This process looks like low pass filtering. By implication a decimated resolution occurs in the migration result. This result recommends us to avoid using low frequencies in constructing the focusing operator.

Figure 4.7e shows a trace of the focusing operator, which is constructed using the Ricker wavelet of 25 Hertz. The frequency bandwidth of the migration result is given in Figure 4.7f. The peak frequency between the input data (solid line) and the migration result (dashed line) is coincident at 25 Hertz, but the flanks of amplitude spectra of the migration result is steeper than the amplitude spectra of the input data. In addition, for high frequencies (Figure 4.7g), the effect can be seen in Figure 4.7h. The Ricker wavelet with a peak frequency of 50 Hertz is used. The frequency bandwidth of the migration result (dashed line) is shifted to a higher frequency with a peak frequency of 32 Hertz.

The dependence of the migration result on the wavelet frequency can clearly be observed in Figure 4.8. The correlation between the peak frequency of wavelet and the peak frequency of the migration result is non-linear. The use of the wavelet frequency, which is lower than the frequency content of the input data, gives worst effects. The peak frequency of the migration result is shifted to the low peak and the narrow bandwidth. In contrast, the use of the wavelet frequency, which is greater than the frequency content of the input data, produces minimum effects. The peak frequency of the migration result is not shifted too far.

Based on the above analysis, it can be concluded that the wavelet frequency should be well determined in constructing the focusing operator. It is very important in order

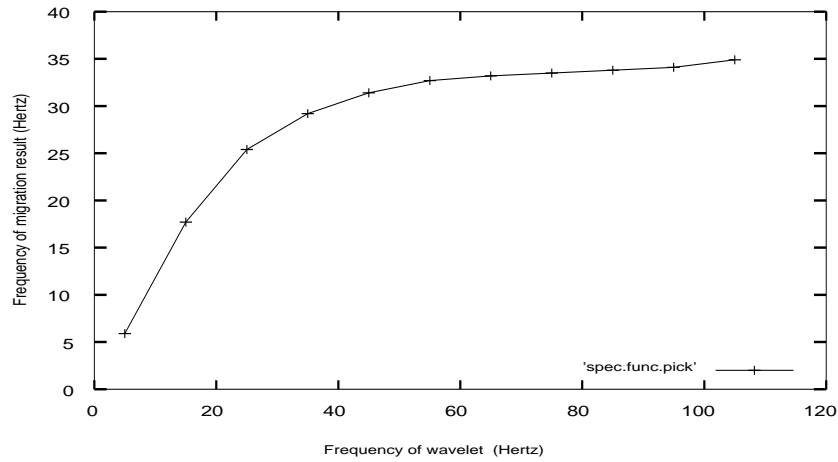


**Figure 4.8.** Frequency-dependent migration result,  $x$  axis represents the frequency of Ricker wavelet used in constructing the focusing operator and  $y$  axis represents the frequency of the migration result.

to preserve the frequency content of the input data. The effect of the wavelet frequency is intimately tied to the temporal resolution of the migration result. Low frequencies will decimate the migration result, on the other hand the high frequencies will produce ringiness. Therefore, the wavelet frequency must be equal to the frequency content of the input data. Since the focusing operator is constructed after traveltime, amplitude and phase calculation, the wavelet frequency can be determined based on the frequency content of the input data. For example, as a simple way, the wavelet frequency can be extracted from the input seismic data as a time variant.

#### 4.4 OBH Synthetic Data

The OBH is a self contained data-acquisition system, which falls freely to the ocean floor and records seismic data generated by airguns and earthquakes. The OBH facility provides technical support for a variety of scientific investigations ranging from deep crustal structure to gas hydrate and seafloor sediment. However, OBH systems are used for refraction seismic measurements to obtain information about deep crust and mantle structures. Using high-resolution systems, the kinematic and dynamic information can be used for investigating the physical and lithological characteristics of the sediment. The analysis method used so far

directly checks models of the physical parameters by forward modeling or inversion to their agreement with the recorded data. The determination of structural images of the subsurface by migration methods is pursued, however, rarely. This is because of the asymmetry of the acquisition geometry of phase shifts from wide-angle reflections, a complex signal form and the limited subsurface area, which can be illustrated by reflections (Hoffmann, 1995; Flueh and Fisher, 1996). The latter is caused on the one hand by the lowered position of the receiver and on the other hand by the overlay of the reflected wave by the direct wave. To illustrate the flexibility of the developed AP migration method in imaging the special seismic data acquisition, an OBH synthetic data set is analyzed.

#### 4.4.1 Velocity Model

For demonstrating the special migration practice the simple model is used. The velocity model is shown in Figure 4.9. The size of the model ranges from 2500 m to 17500 m in the horizontal direction, and from 0 m to 6000 m in the depth direction. The model consists of three layers with a dipping reflector lying at the first interface. It will be regarded as the seafloor. The dipping reflector is a line defined through the points ( $x=8000$  m,  $z=2000$  m) and ( $x=10000$  m,  $z=1500$  m) with a dip angle of 14 degrees. The second reflector that will be imaged by the AP migration method lies at depth of 4000 m. The velocity of the model is varied from 1500 m/s to 4000 m/s as a function of depth.

For generating synthetic data records, six OBHs are deployed over the sea floor (at lateral distances of 5000 m, 7000 m, 9000 m, 11000 m, 13000 m and 15000 m for OBH1 up to OBH6, respectively). The OBH synthetic data for this model is computed by ray-tracing modeling technique. The source position close to the water surface is moved from lateral distance of 100 m to 20000 m and fired at equidistances of 100 m. The synthetic seismogram for each OBH station is shown in Figure 4.10. It should be mentioned that all OBHs record section cover only 10000 shots in which they clearly record the primary reflection. The reflection signals from the distant shots are deteriorated by the direct wave. For example on OBH1, the primary reflection is clearly shown from shot 100 up to shot 10000 and the rest is overlain with the direct wave.

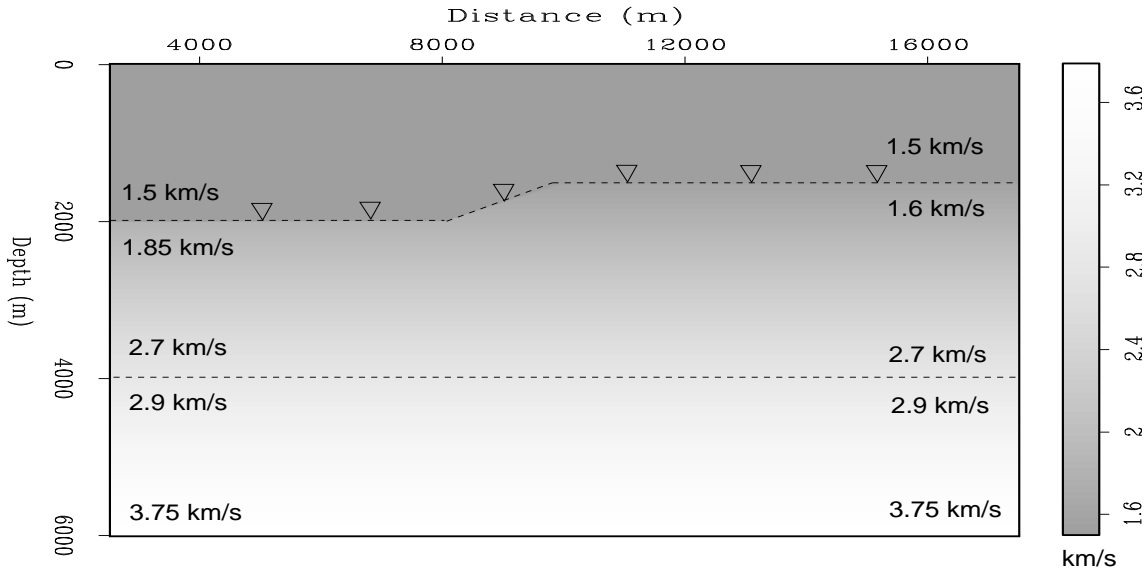


**Figure 4.9.** Subsurface velocity model for OBH experiment. Six triangles from left to right represent the position of OBH1 to OBH6 on the seafloor.

#### 4.4.2 Migrated OBH Synthetic Data

The migration process of the OBH synthetic data is carried out using the same scheme as for the migration process of MCS data. The OBH data are gathered in the shot configuration. For this synthetic data, each shot record contains only six traces related to the number of deployed receivers and has a wide spacing distance of 2000 m, which is uncommon for imaging. As a consequence, a lack of spatial resolving power is observed. This effect is commonly called "acquisition footprints" of relatively sparse source and receiver coverage. Moreover, not all six traces are covered by the focusing operator, except when the coverage of the focusing operator is extended.

To migrate the OBH synthetic data, additional information of the sea floor topography is necessary. In connection with the focusing operator construction, the topography information is required to define the source position for propagating the wave field throughout the subsurface. The correct focusing operators not only require a correct macro velocity model, but also need the correct source location. Since the OBH synthetic data are recorded from the sources that have a different level than the receivers, a preprocessing step is required. The preprocessing step is applied to redatuming the source level from the sea surface to

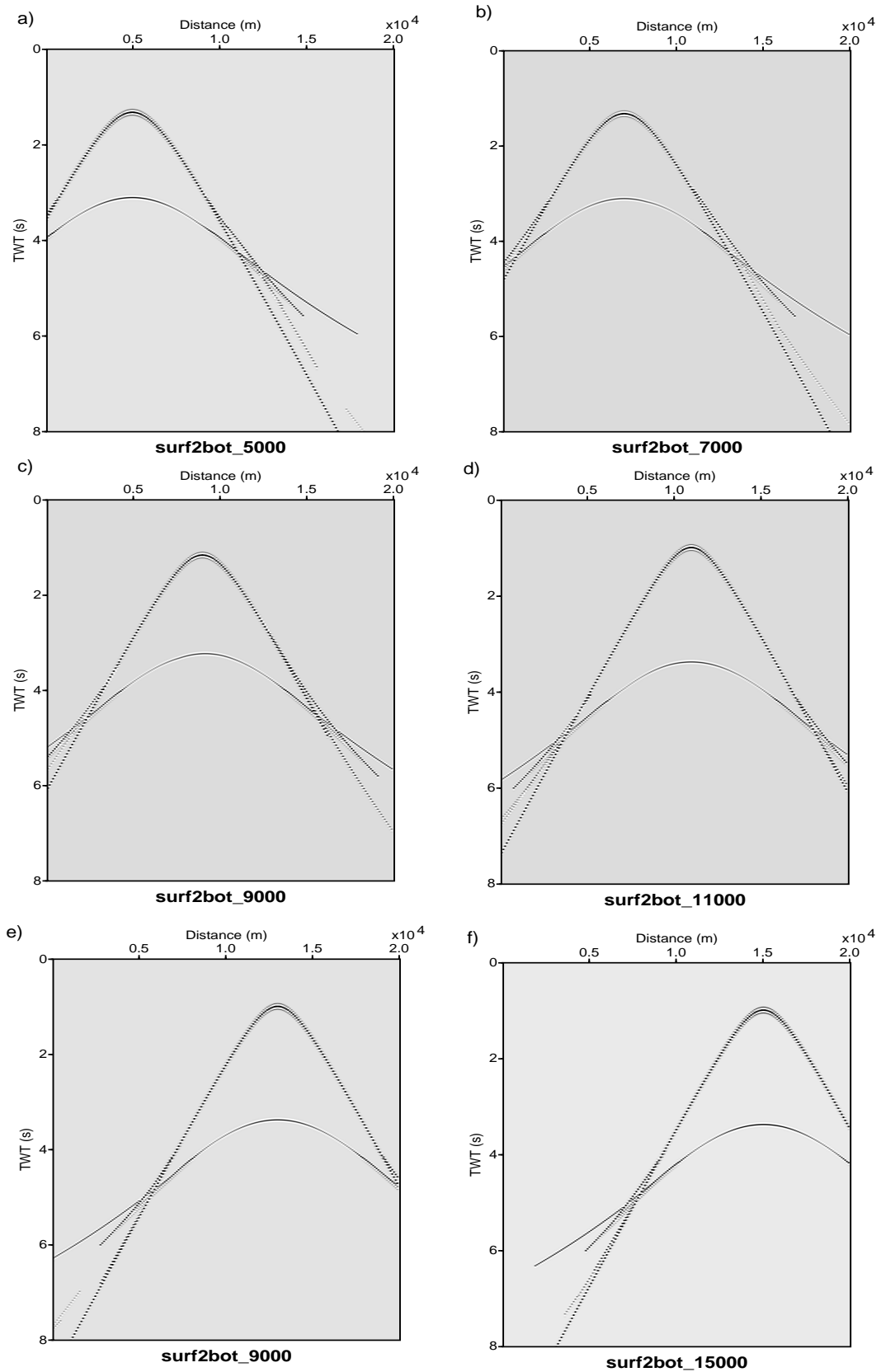


**Figure 4.10.** Original synthetic OBH data: a) OBH1, b) OBH2, c) OBH3, d) OBH4, e) OBH5, f) OBH6.

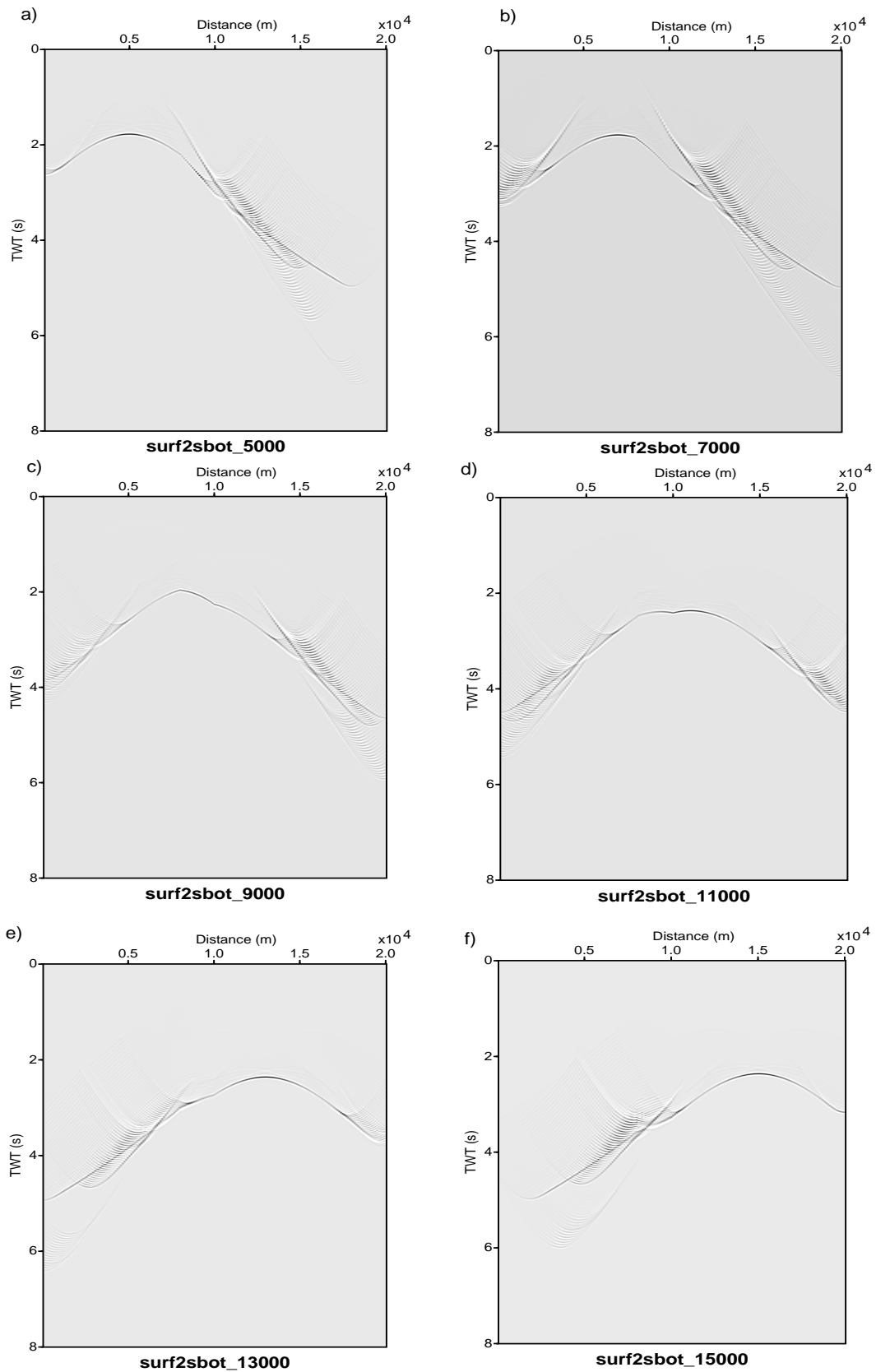


**Figure 4.11.** Synthetic OBH data after downward continuation: a) OBH1, b) OBH2, c) OBH3, d) OBH4, e) OBH5, f) OBH6.



the seafloor by wave field continuation based on the Kirchhoff summation method. The synthetic OBH data after downward continuation are presented in Figure 4.11. The reflection events at the far shots suffer from spatial aliasing during the downward continuation process. However, the reflection events at the centre of the aperture up to a distance of 8000 m still can be identified.

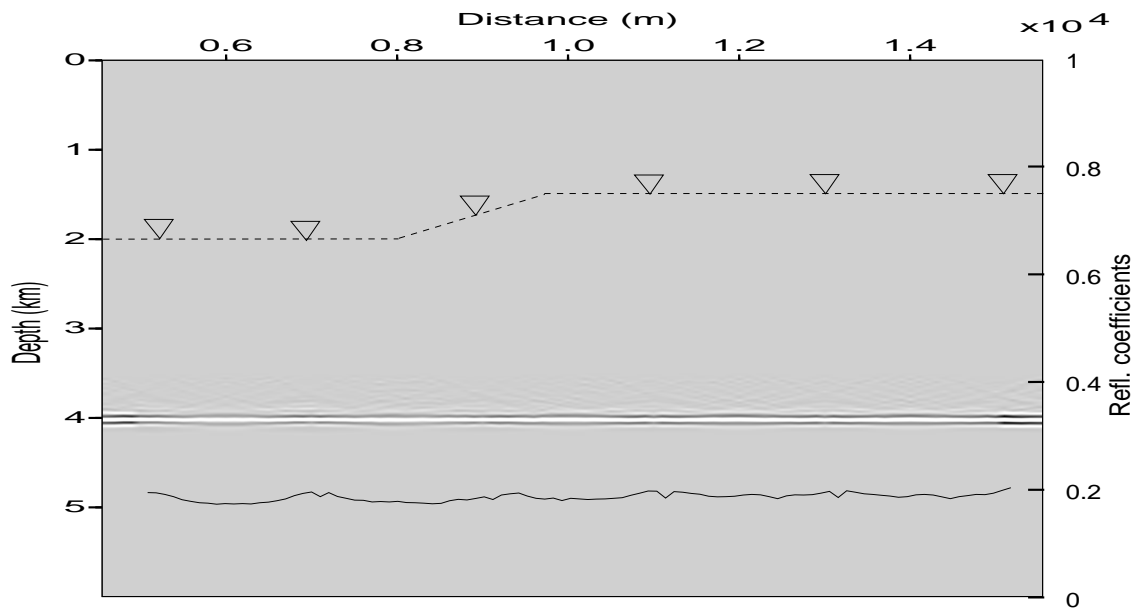


**Figure 4.12.** The AP migration result of the primary reflection of OBH synthetic data. The picked amplitude (solid lines) is superimposed on the migrated section.

The migration result of the OBH synthetic data is presented in Figure 4.12. This example only illustrates the confocal version. The image shows an almost perfect subsurface structure in the entire target zone. The depth position of the reflector can be imaged perfectly and shows a good agreement with the macro velocity model (Figure 4.11) even if a rough spatial grid is chosen (200 m) following the shot position. Smoothing the temporal and spatial grid would permit further improvement of the subsurface image. A combination of the migration result from OBH and MCS data would be very useful, in order to close the gap of the seismic reflection image from one another.

The picked amplitudes, which are superimposed with the migrated section shown in Figure 4.12, illustrate the amplitude response of the migrated image. In general, the amplitude

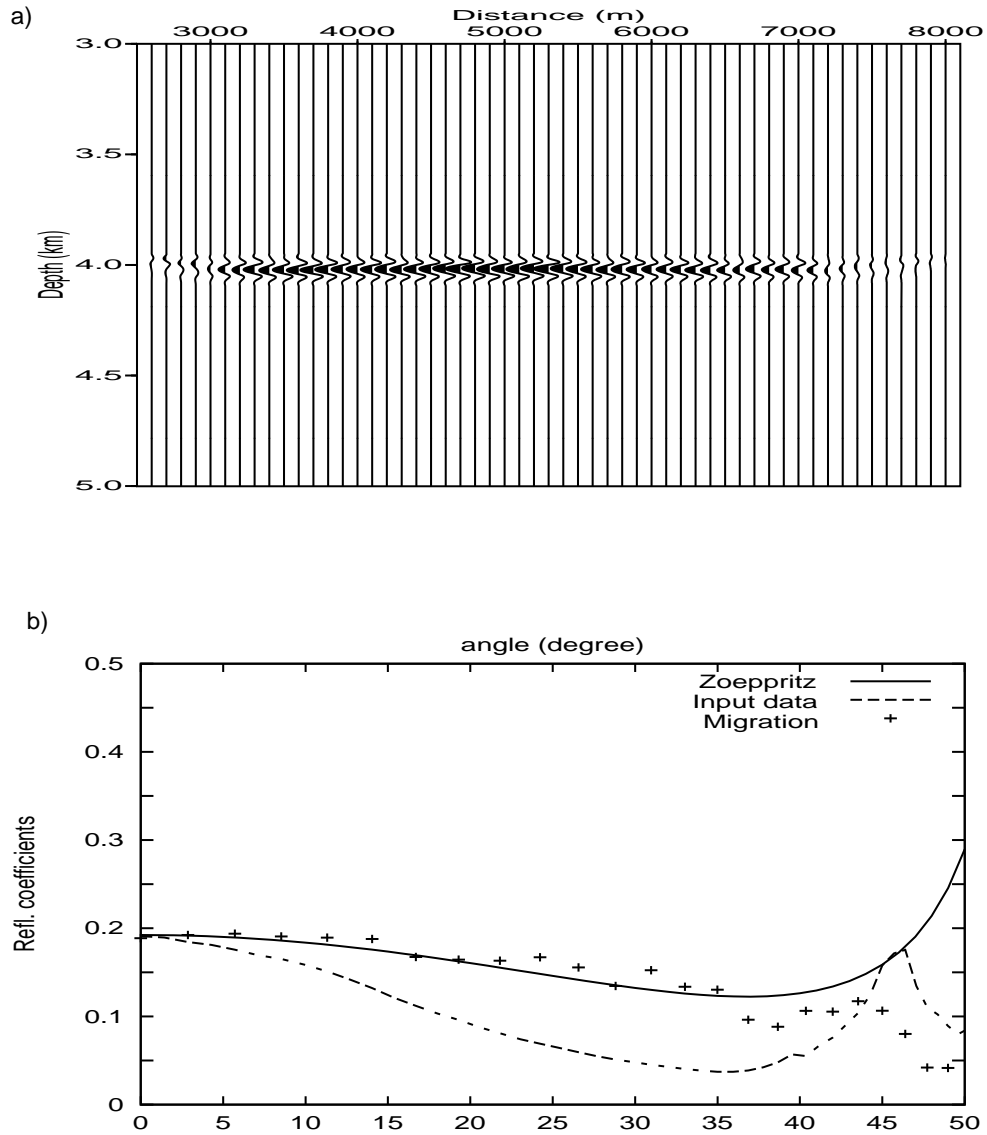


**Figure 4.13.** The AP migration result of the recorded data by OBH1 at a lateral distance of 5000 m a) and comparison of reflection coefficients obtained by the AP migration (crosses line) after distance to angle conversion with theoretical value (solid line) calculated by Zoeppritz' equations, which are superimposed with reflection coefficients of the input data after downward continuation (dashed line) b).

response is reasonable in that it is nearly constant along the reflector. However, since the spacing distance between two OBHs is too far, the high amplitudes are distributed around the OBH position. There is a limitation of the focusing operator coverage and fold coverage.

Unfortunately, the bifocal version of the AP migration, which produces angle-dependent reflectivity gathers, cannot be applied to this special seismic data acquisition. This is because the OBH data provide a minimum fold coverage, which is caused by a very sparse receiver distance and a few number of receivers. Therefore, the migrated angle-dependent reflectivity gathers are not demonstrated for this data set.

In this example, the amplitudes of the AP migration result are verified based on the migrated image of the OBH1 at a lateral distance of 5000 m. This data set is recorded by the OBH1 from shot position at 100 m to 20000 m. This means that each shot record contains only one trace. Technically, this migration procedure is similar to the bifocal version, where the focusing operators are shifted around the grid point at a lateral distance of 5000 m. However, the migrated gather is a function of the distance from the grid point at 5000 m to where the focusing operators are shifted. Figure 4.13 shows the migrated image of the OBH1 a) and its reflection coefficients in comparison to its theoretical value and the input data b). The reflection coefficients are illustrated in the angle domain after a distance to angle conversion, which is performed from a lateral distance of 5000 m as zero point to 7500 m as a maximum distance. The reflection coefficients of the migrated image agree well with the theoretical value calculated by Zoeppritz' equations. Their comparison to the amplitudes of the input data set indicates that the AP migration has successfully compensated the geometrical spreading effects.

## 4.5 Marmousi Synthetic Data

The Marmousi data set is a complex model for testing migration methods. It is a realistic model based on a profile through the North Quengeula trough in the Cuanza basin, which was generated at the Institute Français du Pétrole. This data set has been used in the workshop for practical aspects of seismic data inversion at the 1990 EAEG meeting in Copenhagen (Versteeg, 1993). Many groups tried to determine a correct Earth image from this data set and reported the failure of the Kirchhoff algorithms using first arrival

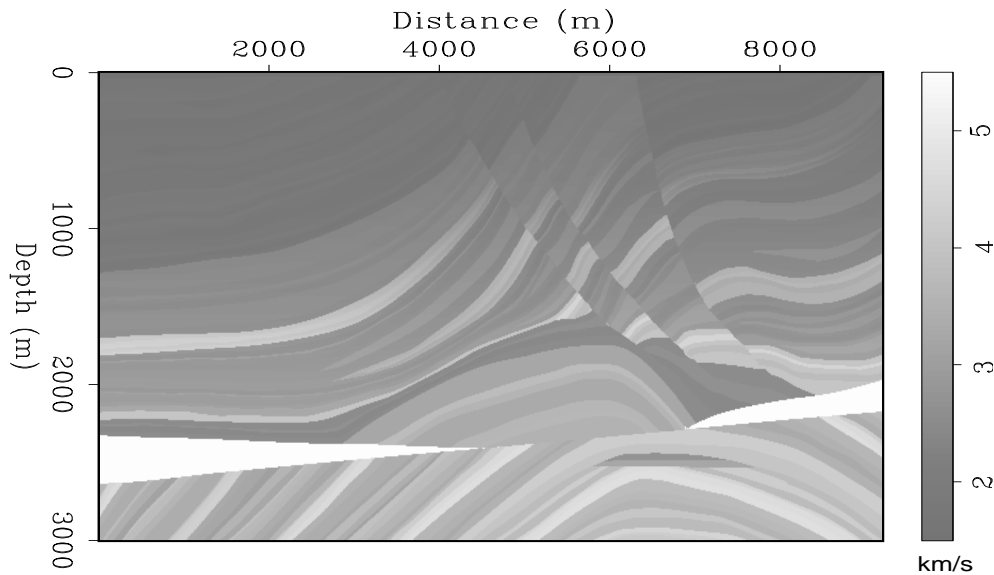


**Figure 4.14.** The Marmousi velocity model with a fine grid size (12.5 m, 4 m).

traveltimes in imaging the complex area (Geoltrain and Brac, 1993).

The velocity distribution of this model has strong horizontal and vertical gradients (with a minimum velocity of 1500 m/s and a maximum velocity of 5500 m/s). The velocity of the Marmousi model, which is conformable with the geometry and the geological structure, is shown in Figure 4.14. The velocity distribution is generated with the aim of producing complex seismic data. Marine data acquisition was simulated using a two-dimensional finite difference acoustic modeling algorithm. The data set consists of 240 shots with 96 traces/shots. The near offset is 200 m, the source and receiver spacing is 25 m. Shooting extends from  $x=3000$  m to  $x=8975$  m. The record length is 2900 ms with a sample rate of 4 ms.

No preprocessing step was applied to the input data set, except a refraction mute to suppress all events with an apparent velocity of less than 1500 m/s. Several shot gathers of the Marmousi data set after muting are presented in Figure 4.15. The shot gathers show non-hyperbolic move-out and back scattered energy. This data set indicates that it may only be imaged correctly using prestack depth migration. A near offset section of the Marmousi data set is shown in Figure 4.16. The data set is free of noise and contains refractions and multiple reflections.

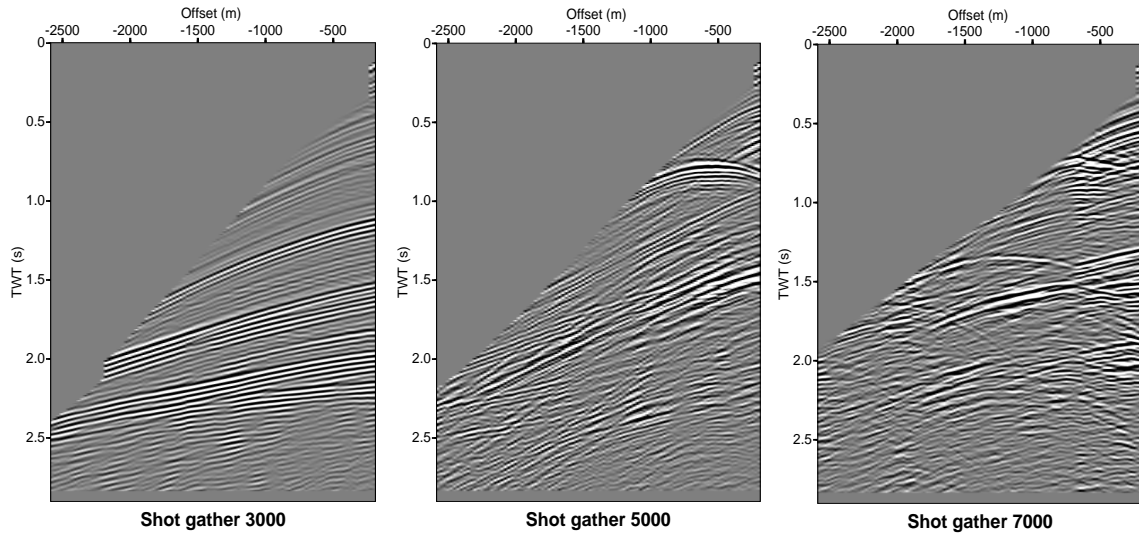


**Figure 4.15.** The Marmousi data set, three shot gathers at lateral distance of 3000 m, 5000 m, and 7000 m.

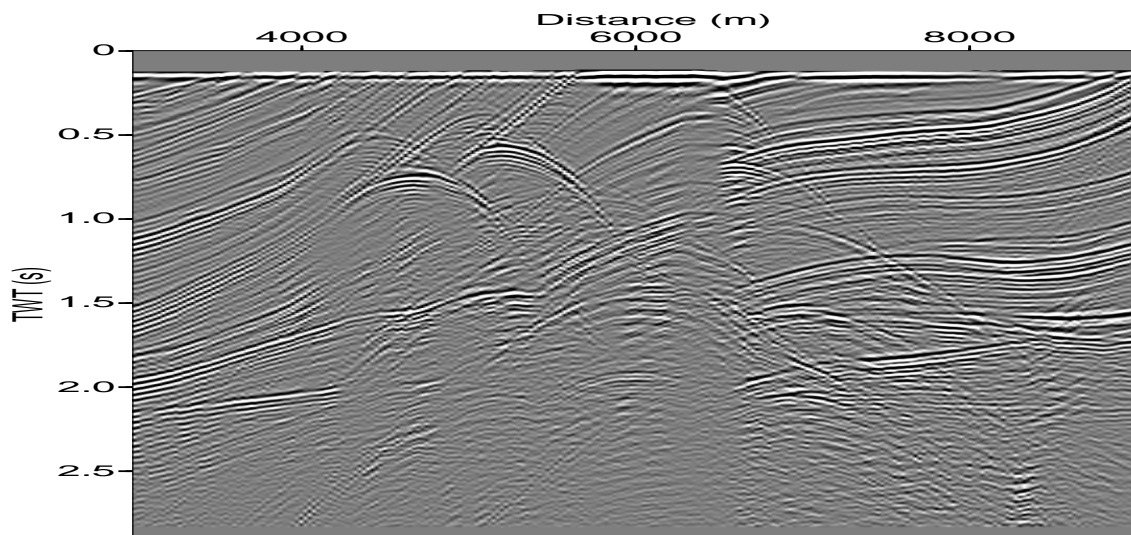


**Figure 4.16.** The near offset section of the Marmousi data set.

The application of the AP migration method to the Marmousi data set is restricted to structural imaging. As a comparison for structural imaging, the Marmousi data set is also migrated using the commercial Kirchhoff method. To see the essential role of amplitude and phase information in the imaging process, this data set is migrated with and without amplitude and phase information. In addition, the use of an approximate velocity model and sparse-shot geometries are presented.

The examples on the angle-dependent reflectivity imaging are applied to see the performance of the AP migration in a realistic complex model. However, no attempt to verify the amplitudes of the migrated angle-dependent reflectivity gathers is made, since the model is very complex and not suitable for doing an AVA analysis. Multiple thin layers and complex structures caused the reflection amplitudes to suffer from several effects (e.g., tuning effects, interbed multiples). Moreover, the data set is the result of an acoustic modeling. Therefore, it does not represent the true response of an elastic Earth and will not contain shear wave conversion or correct amplitude versus angle behavior.

#### 4.5.1 Migrated Marmousi Synthetic Data

Figure 4.17 is the migration result of the Marmousi synthetic data set using a commercial Kirchhoff method. In principle, this program uses explicit traveltimes to define the operator aperture and stacks all events that are covered by the aperture. The Kirchhoff method uses a fine grid size (12.5 m, 4 m) of the velocity model. Amplitudes and phases are not taken into account in the migration process. The migration result can not be regarded as true-amplitude, but is useful as a benchmark of structural images. In general, the migration result is good, almost all features of interest have been imaged. The upper part of the model is visible, but the area of interest below 2200 m and the anticlinal structure (at 6500 m, 2500 m), particularly the flat spot, is not clearly imaged. In another part of the section, the blocky structures (at around 6000 m, 1700 m) are also not clear.

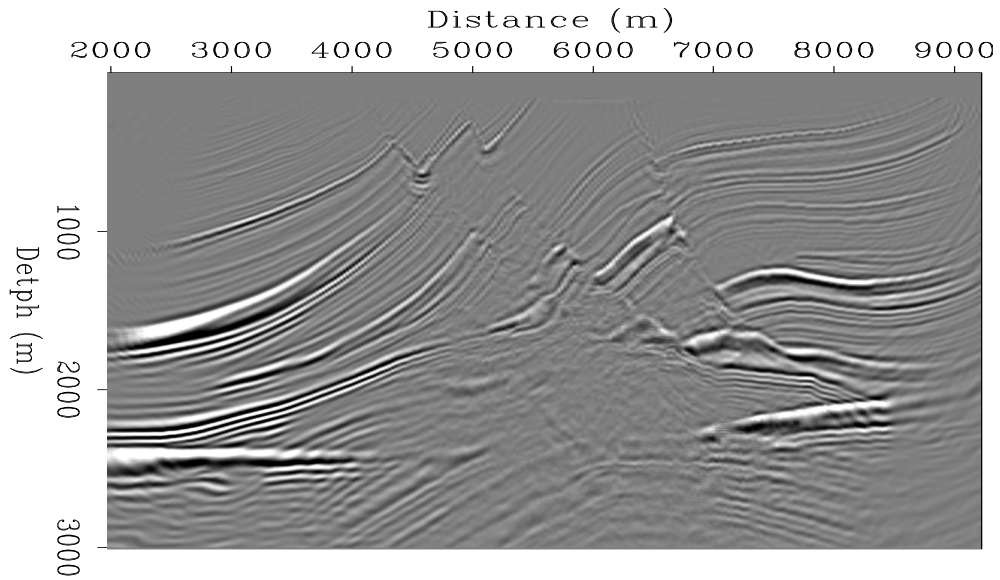
The AP migration result of the Marmousi data set using the multi-valued operators is presented in Figure 4.18. In addition to the traveltimes information, the amplitudes and phases are included in the focusing operators. The Marmousi data set is migrated using a large grid size (25 m, 25 m) of the velocity model. This image shows a good recovery of

relative correct reflectivities and an overall crisper image. Each reflector displays relative correct amplitudes and the trap structure, especially the flat spot, shows a strong amplitude. For structural imaging, the AP migration method produces a much better image of the subsurface than the Kirchhoff method. The blocky structures and the dome section that were not clear in the Kirchhoff image have been clearly imaged.

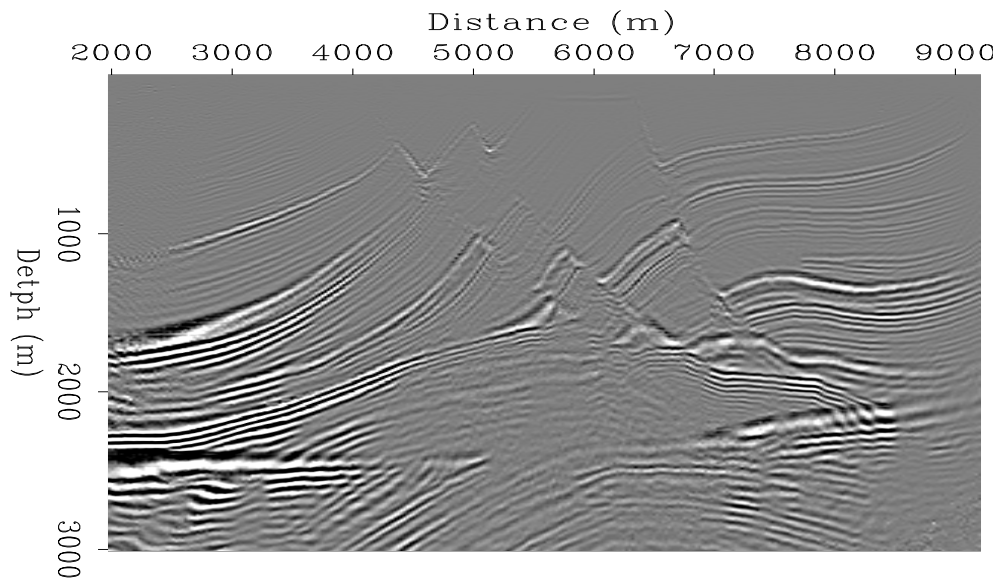
Figure 4.19 demonstrates the AP migration result of the Marmousi data set using the single-valued operators. Note that the single-valued operators in this case are the maximum energy arrival instead of the first arrival of the wave field. This means that the main contribution of the wave field is introduced by the focusing operators. This result shows a comparable image to Figure 4.18, which is migrated using the multi-valued operators. Only minor artifacts, particularly in the dome structure, are introduced. Even the peak of the anticlinal structure is less clear, however, the image has no significant distinction compared to Figure 4.18, since the energetic events are given by the focusing operators. On the other hand, the use of the single-valued operators of the maximum energy is less expensive than the multi-valued operators. In order to generate the multi-valued operators, the band limited Green's function algorithm requires a large number of frequencies and a fine grid of polar coordinates. Therefore, the next migration examples use the single-valued operators.

Figure 4.20 illustrates the effects of the amplitude and phase information on the migration result. The Marmousi data set is migrated using the AP migration method, but the amplitude and phase information are not included in the focusing operators. The phase is assumed to be zero and the amplitude is assumed to be one. The migrated image looks noisy, particularly in the dome section and in the vicinity of the target zone. Moreover, the blocky structures (around  $x=5600$  m,  $z=1700$  m) are not clear. Some events (e.g., a wedge structure around  $x=2500$  m,  $z=2500$  m) indicate a phase shift compared to the image in Figure 4.20, in which amplitude and phase information are included in the focusing operators.

The closer inspection of the target zone of the migrated image in which the focusing operators consider and ignore the amplitude and phase information is illustrated in Figure 4.21. Figure 4.21b shows a better image compared to Figure 4.21a. The flat spot and



**Figure 4.17.** The Marmousi data set migrated using a commercial Kirchhoff method.



**Figure 4.18.** The AP migration result using multi-valued operators in which amplitudes and phases are taken into account.



the anticlinal structures are deteriorated by ignoring the amplitude and phase information. In contrast, the flat spot and the anticlinal structures are well imaged by considering the amplitude and phase information.

Figure 4.22 shows the migrated image using the AP migration where the focusing operators consider the amplitude and phase information but the weight function, which is used to preserve the amplitude, is not applied. This means that no division with zero-lag of the focusing operators after double stacking is applied. The migrated image shows prevalent amplitude distribution throughout the section. The upper portion of the section shows stronger amplitudes compared to the image in Figure 4.19. For structural imaging purposes, the AP migration method without the zero-lag division may be useful. Obviously, the image is very good, almost all features are clearly displayed. However, the correct relative amplitudes are not seen on the different reflectors. In this case, the effect of the weight function, which is represented using the zero-lag division, is not significant because the amplitude decay in the data set may not be present. In contrast, the weight function will be essential for real seismic data sets, especially for angle-dependent reflectivity imaging.

In the previous examples, the Marmousi data set is migrated using the true velocity model. To see the sensitivity of the AP migration method to the velocity model, an approximate (smoothed) velocity model is used to image this data set. Figure 4.23 shows the migrated image using the smoothed Marmousi velocity model with a smoothing radius of 100 m. Note that the weight function is not applied, since the goal is to check the resulting image using an approximate velocity model. Generally, the migrated image looks similar to the image in Figure 4.22, which uses the true velocity model. The minor difference is shown in the faulted structure (at around  $x=4500$  m,  $z=600$  m). From this image it can be concluded that the AP migration method is still able to produce a good image even when using an approximate velocity model only.

The sparse-shot geometries as so-called acquisition footprints are presented in Figure 4.24. The data set, which consists of 24 shots with an increment of 250 m started from  $x=3000$  m to  $x=8900$  m, is migrated using a true velocity model. In order to produce strong events, the weight function is also not applied. The image shows the area of high illumination corresponding to brightspots, particularly in the part of the section (shallow depth). These

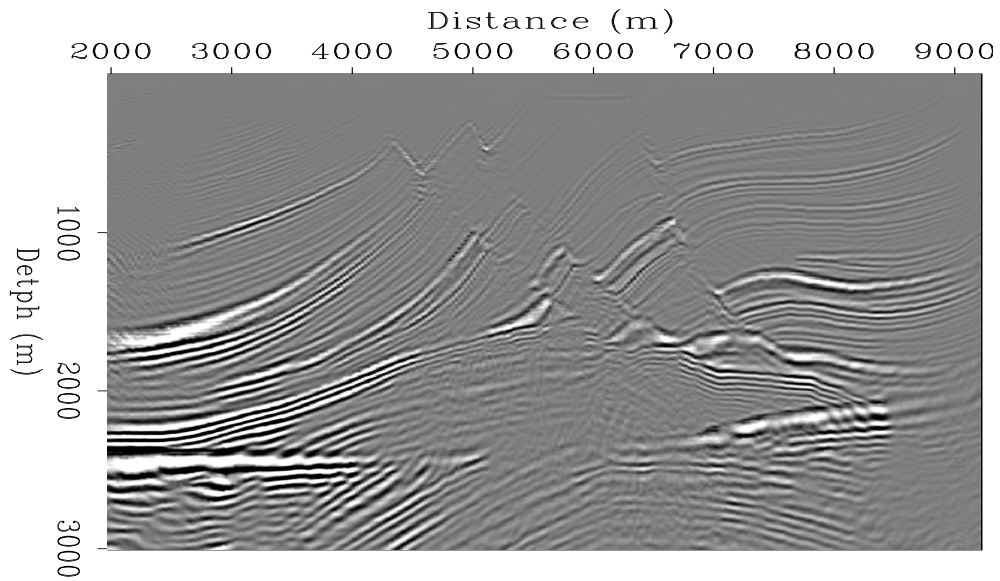


**Figure 4.19.** The AP migration result using the single-valued operators of the maximum energy in which the amplitude and phase information are taken into account.

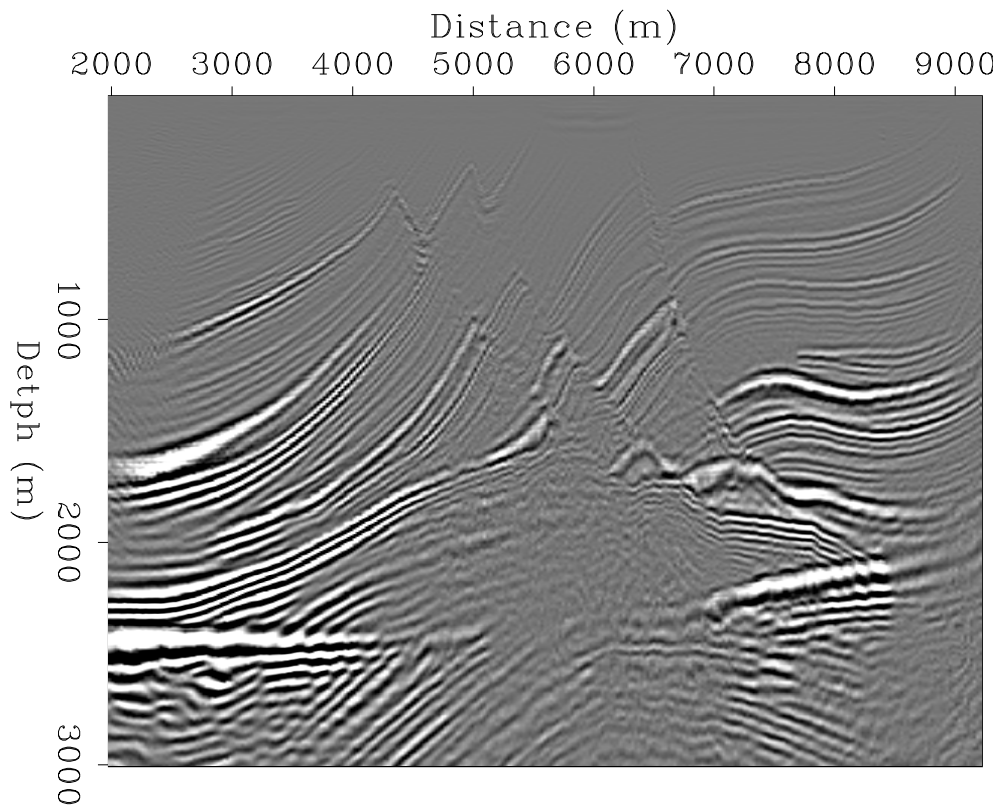


**Figure 4.20.** The AP migration result using the single-valued operators of the maximum energy, but the amplitude and phase information are not taken into account.

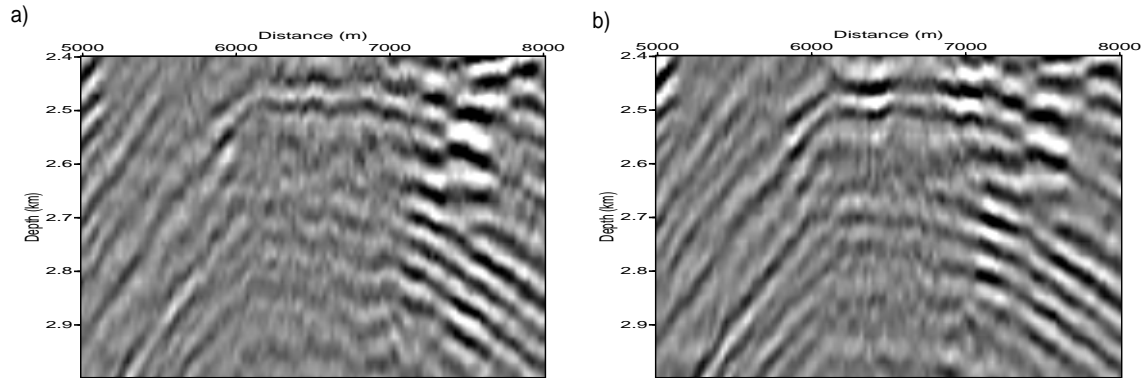


**Figure 4.21.** The close up comparison at the target zone of the migrated image in which the focusing operators ignore a) and consider b) the amplitude and phase information.

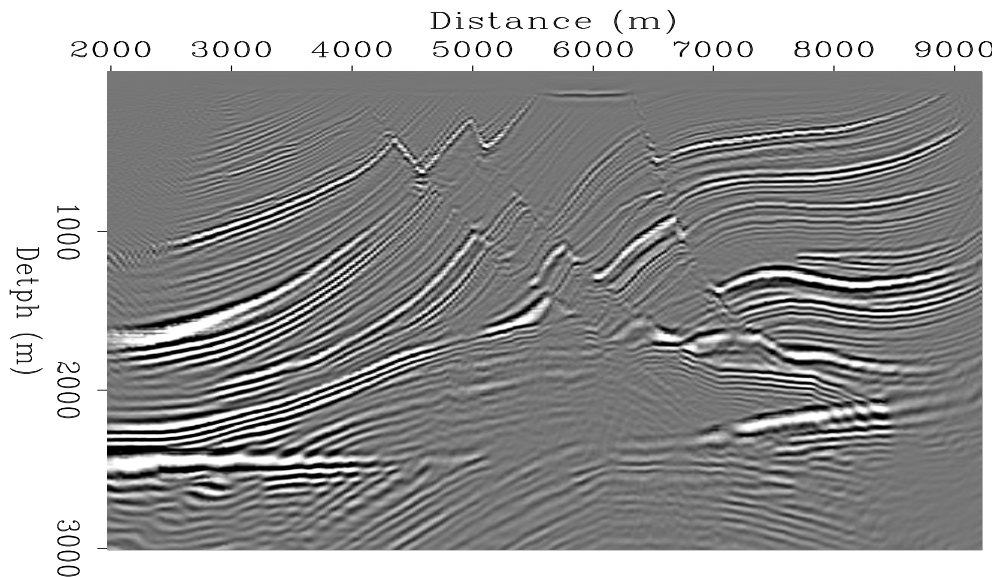


**Figure 4.22.** The Marmousi data set migrated using the AP migration in which the amplitude and phase information are included in the focusing operators, but the zero-lag division is not applied.

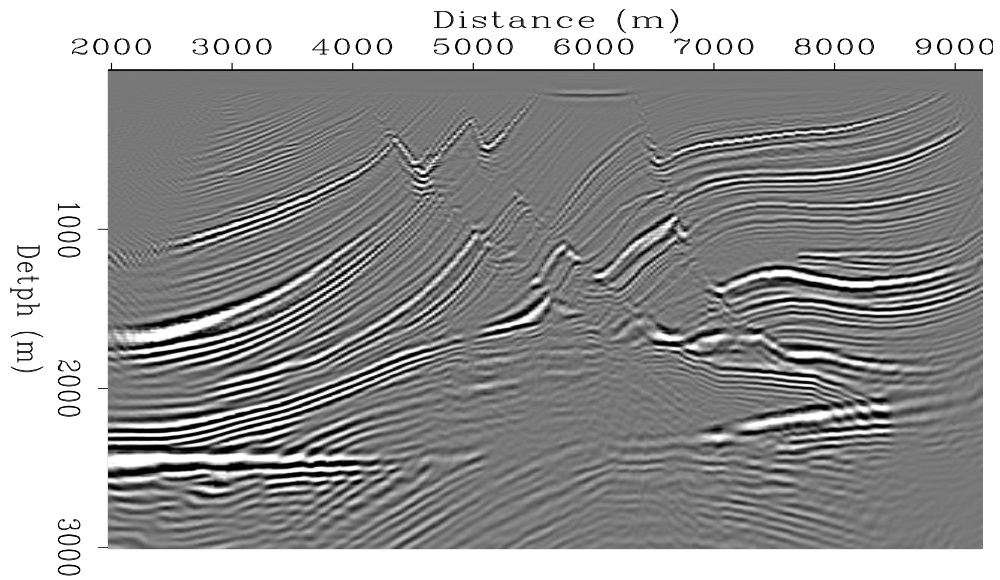


**Figure 4.23.** The AP migration result using an approximate velocity model without applying the zero-lag division.

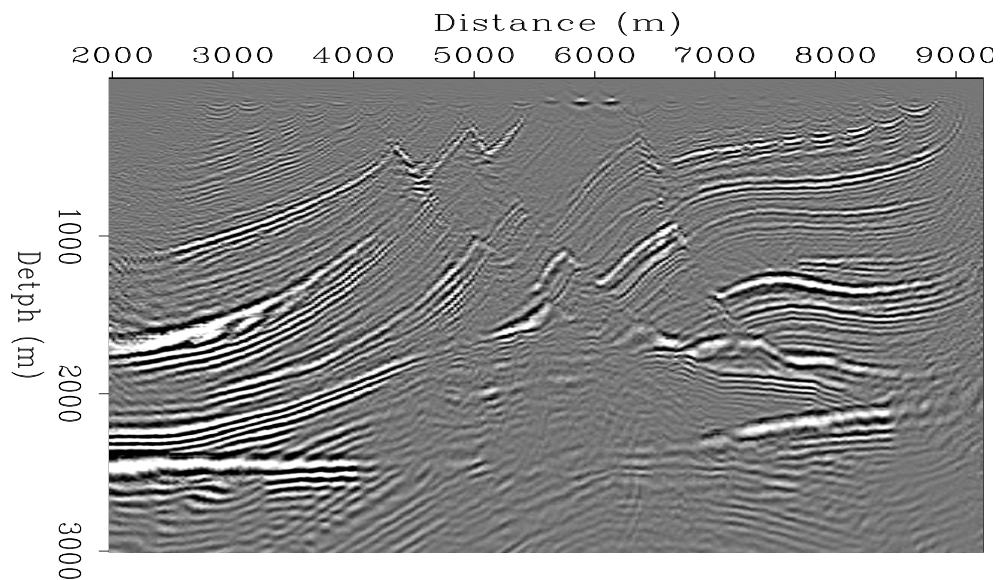


**Figure 4.24.** The Marmousi data set migrated using the AP migration without applying the zero-lag division for a relatively sparse source spacing ("acquisition footprints").

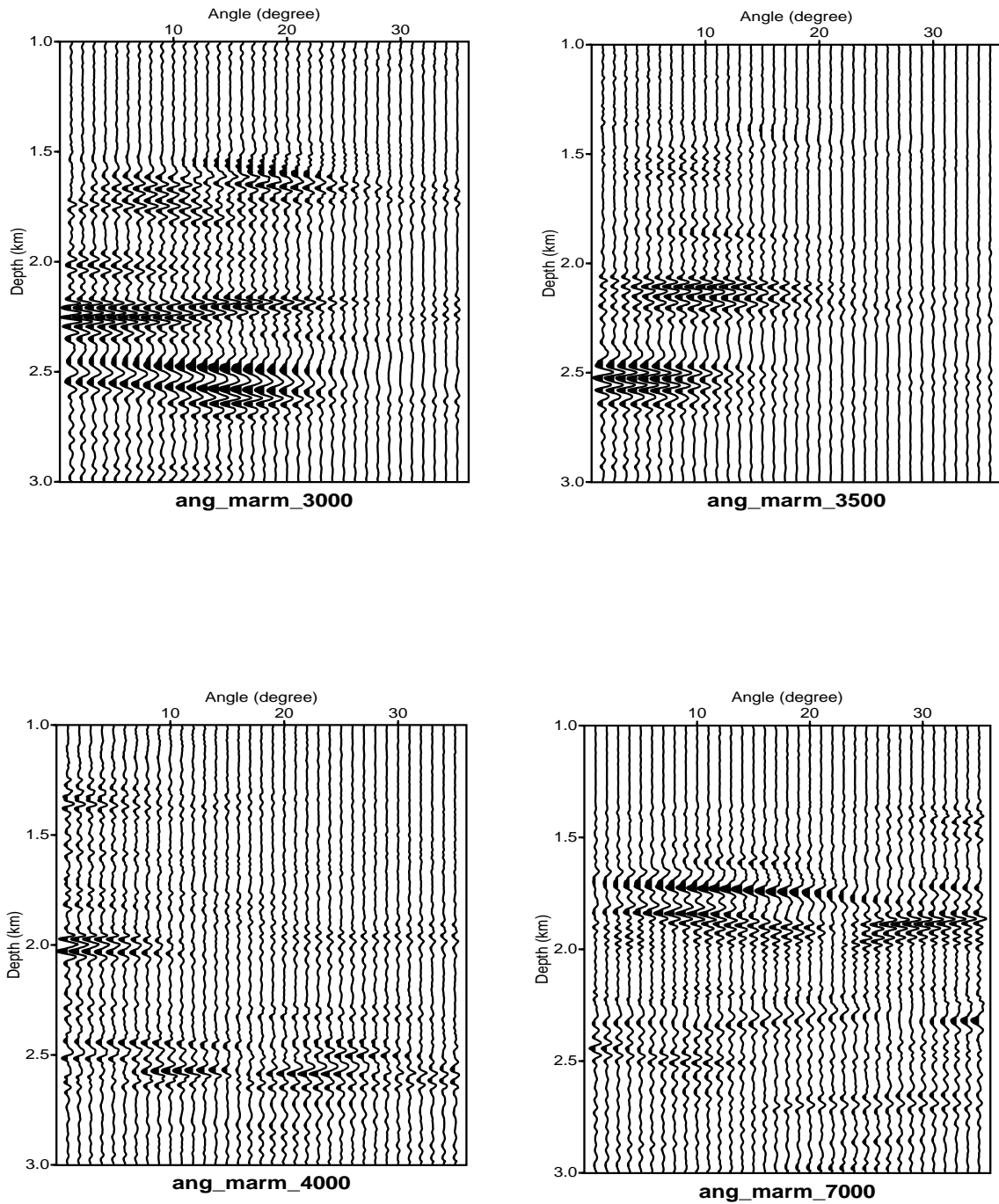


**Figure 4.25.** Angle-dependent reflectivity gathers at lateral distances of 3000 m, 3500 m, 4000 m, and 7000 m.

artifacts are created by truncation in the data set (mute, acquisition geometry). For greater depths, these artifacts are subdued. In general, the migrated image shows comparable structures in terms of lateral continuity and structural definition. However, this image needs to be normalized to remove shot-aliasing effects.

The last example demonstrates the angle-dependent reflectivity imaging using the bifocal version of the AP migration. Figure 4.25 shows the migrated angle-dependent reflectivity gathers for several lateral distances. Three positions (3000 m, 3500 m and 4000 m) at surface in the relatively simple part are selected. The migrated angle-dependent reflectivity gathers show flat images. Another position is at a lateral distance of 7000 m. This position is located across the complex part in the hydrocarbon trap at a depth of 2500 m. The angle-dependent reflectivity gather still shows flat events. However, the amplitude distribution is at incorrect positions, since the dip correction is not applied. The dip correction is included as a postprocessing step toward AVA analysis. Therefore, thorough discussion about the correction of the dip reflector effects is given in Chapter 5.

## Chapter 5

# Application of the AP Migration to Real Seismic Data

### 5.1 Introduction

After achieving promising results with synthetic data sets, the AP migration is now applied to a real seismic data set. Marine MCS reflection data collected across the continental margin offshore Oregon (line OR89-02), that reveal hydrate through the presence of bottom simulating reflectors (BSRs), will be imaged in terms of angle-dependent reflectivity as well as structural imaging. BSRs are commonly interpreted as the boundary between hydrate-bearing sediment and gas-bearing sediment located beneath them and present an area of interest to the developed method to recover correct relative amplitudes, which are essential for the subsequent amplitude versus angle (AVA) analysis.

This chapter gives an overview of the data set used in this study and presents the result of the AP migration applied to the 2D marine data set. The migration result is analyzed in the context of the performance of the AP migration in preserving correct relative amplitudes and in view of the quality of the structural image. As a comparison, particularly for structural imaging, the data set is also migrated using two commercial software packages; Kirchhoff migration and shot profile finite difference migration. The examination of local BSR AVA response is demonstrated at several locations along the profile using the migrated angle-dependent reflectivity gathers. The AVA attributes include a primary and a secondary AVA attribute, which are essential for the interpretation and for an estimation of the physical properties of the bottom simulating reflector. The primary AVA attribute is the normal

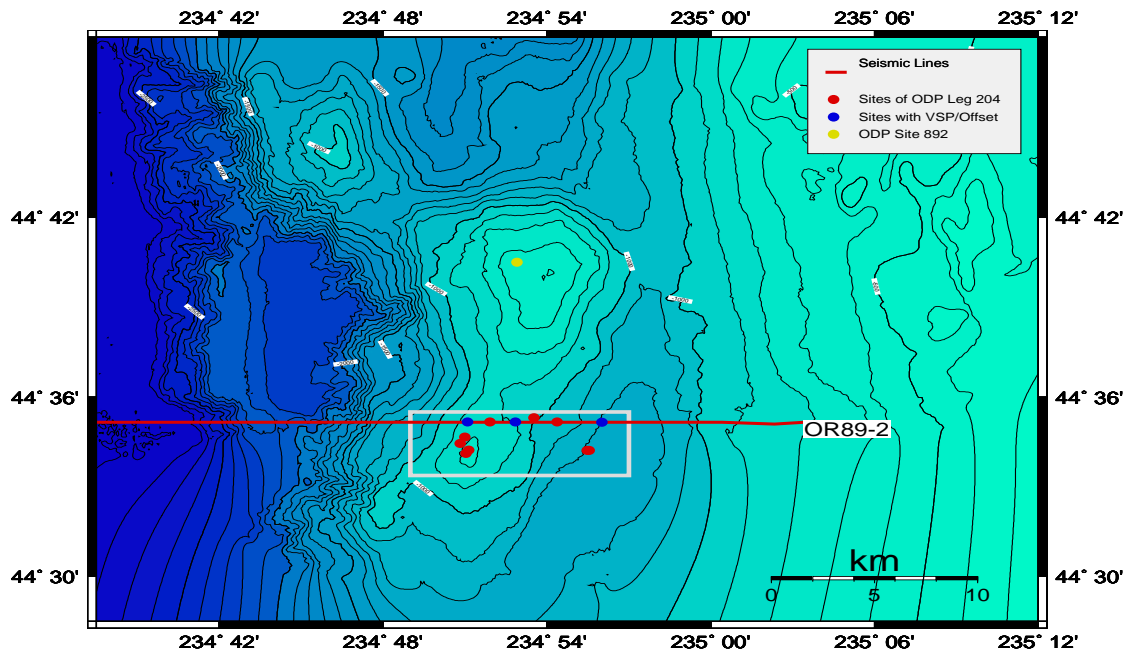


**Figure 5.1.** Map of the location of seismic line OR89-02 crossing the Hydrate Ridge area.

incidence P-wave reflection coefficient, whereas the secondary AVA attribute is the gradient of amplitude versus squared sine of incidence angle. These two attributes are estimated from migrated angle-dependent reflectivity gathers. Finally, an AVA modeling is performed to explain the possible causes of the seafloor and the BSR response.

## 5.2 Oregon Seismic Line OR89-02

The data used in this study was recorded at Hydrate Ridge off Oregon (MacKay, 1992). A map of the region is shown in Figure 5.1. Seismic line OR89-02 extends in E-W direction over the Hydrate Ridge. The part of the seismic line, which is used for this test, is marked by the rectangle in Figure 5.1. The map also displays the position of the drill hole and the proposed drill site for Ocean Drilling Program (ODP) leg 204. The data set consists of 600 shots with 111 traces/shot. The near offset is 250 m, and the source and receiver spacing are 25 m. The record length is 4000 ms with a sample rate of 4 ms.

The geology of this area is characterized by the young oceanic lithosphere of the Juan de



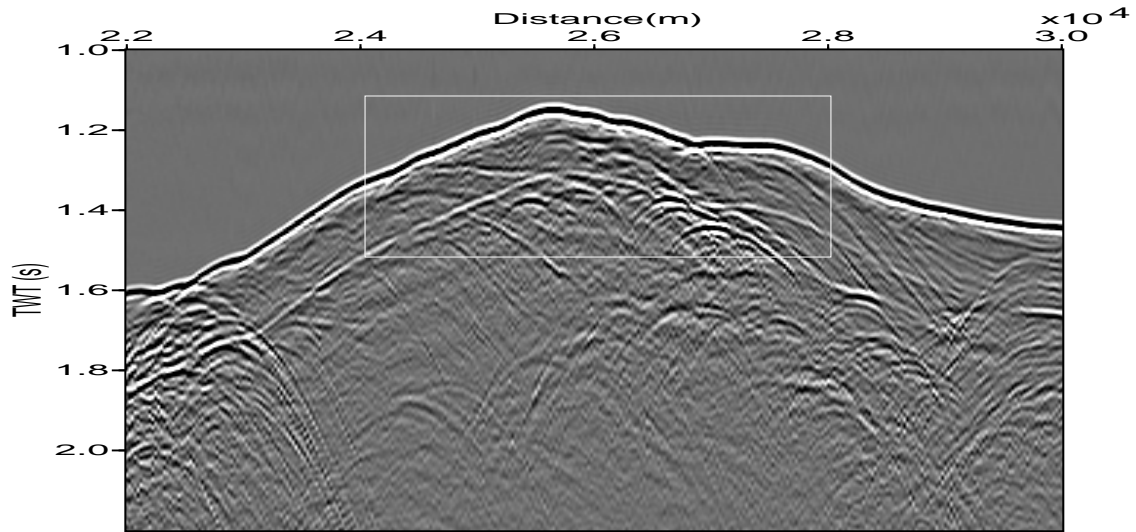


**Figure 5.2.** Near offset section of seismic line OR89-02. The area of interest, which will be inverted to AVA attributes, is marked by the rectangle.

Fuca plate subducting obliquely beneath North America. A thick, actively deforming accretionary wedge exists along the base of the continental slope adjacent to the sediment filled trench (Flueh and Fisher, 1996). This area is also characterized by its wealth of clathrates and hydrate-related deposits. Previous studies have reported that the accumulated sediment of the upper plate, the so-called Cascadia accretionary prism, contains massive gas hydrates and associated chemical anomalies (brines), their chemical oxidation products (authigenic carbonate), and typical fauna assemblages related to methane-rich fluids (e.g., Klaeschen et al., 2001). In the seismic section, this condition is indicated by the distribution and variability of the BSR.

### 5.2.1 Preprocessing

In the first preprocessing step, a refraction mute is applied to the data set to suppress all events with an apparent velocity of less than 1500 m/s. Following a refraction mute, a surface-consistent deconvolution is applied to compress the basic source and receiver wavelet. Figure 5.2 displays a near offset section of seismic line OR89-02 after preprocessing. The figure shows numerous strong diffractions underneath the BSR. These diffractions show the complexity of the structures and may be caused by three-dimensional features such as

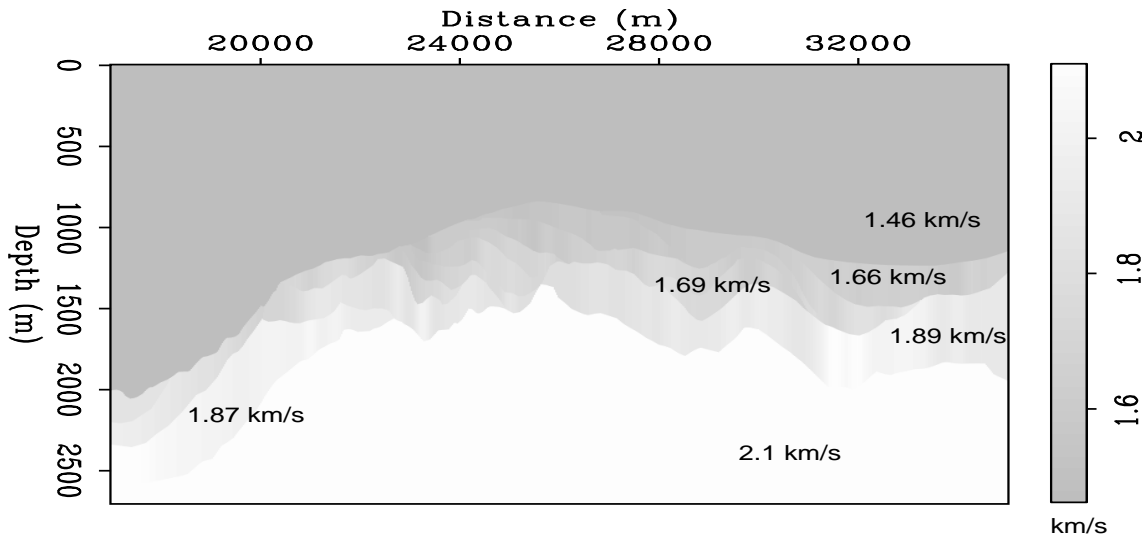


**Figure 5.3.** Velocity model as input to the AP migration.

small gas pockets. The seafloor reflection occurs at about 1.6 s two-way traveltime (see scale at the left side of the section), indicating a water depth of more than 1200 m with variation across the Hydrate Ridge (and decreases in depth gradually up to the summit of the Hydrate Ridge and increases back in depth up to the end of the line). A strong BSR follows the seafloor along the line, suggesting the presence of gas hydrates in this region.

The macro velocity model, which is generated from the focusing analysis conducted during iterative prestack depth migration using MIGPACK commercial software, is shown in Figure 5.3. The sediments in the region are fairly uniform with no major lithological changes within several hundred meters beneath the seafloor. According to the BSR appearance, the structural imaging of the MCS line OR89-02 is carried out from lateral distance of 22000 m to 30000 m, whereas for the angle-dependent reflectivity analysis, imaging is performed only on the area of interest.

### 5.3 Migration Results

This section presents the results of the application of the AP migration to the 2D marine data set. The AP migration recovers both: the structural image and the angle-dependent reflectivity image. Two tests, especially to investigate structural imaging, are performed

on the data set in connection with the improvement of spatial resolution. Another test is carried out to see the effect of the amplitude and phase information, which is included in the focusing operator, on the migration result.

In addition, to compare the structural image of the AP migration to other migration types, two images resulting from Kirchhoff migration and the finite difference shot-profile migration, respectively, are presented. Finally, angle-dependent reflectivity imaging is carried out to produce migrated angle-dependent reflectivity gathers, which are used as input to the AVA inversion. Several migrated angle-dependent reflectivity gathers along the seismic line are displayed to examine the amplitudes that correspond to the BSR reflection and the seafloor reflection, respectively.

### 5.3.1 Structural Image

Two tests using the AP migration with different migration grid size are presented to demonstrate the influence of the grid size on spatial resolution. Figure 5.4 shows the migration result using a relatively sparse migration-grid. The increment of the horizontal grid follows the trace spacing within the shot gather (25 m), whereas the increment of the vertical grid is 5 m. In order to cover the whole offset of the shot gather profile, a wide aperture (6 km) of the focusing operator is generated. Each focusing operator consists of 241 traces with a trace spacing of 25 m. The focusing operator used in this migration process includes traveltime, amplitude and phase information. Please refer to Chapter 2 for the construction of the focusing operator.

In general, the AP migration produces a good structural image. Almost all features of interest have been clearly imaged. The seafloor reflection can be clearly seen along the section, which is marked by a positive polarity. The strong bottom simulating reflection is indicated by a negative reflection polarity. The BSR continuity, following the seafloor reflections, is very clear along the seismic line.

Furthermore, the image shows considerable stratigraphic and structural complexity both above and below the BSR. Each reflection is characterized by its correct relative amplitude. Some reflections are anomalously bright, and these amplitude anomalies are maintained for hundreds of meters. For example, two reflection events below the BSR (labeled B1 and

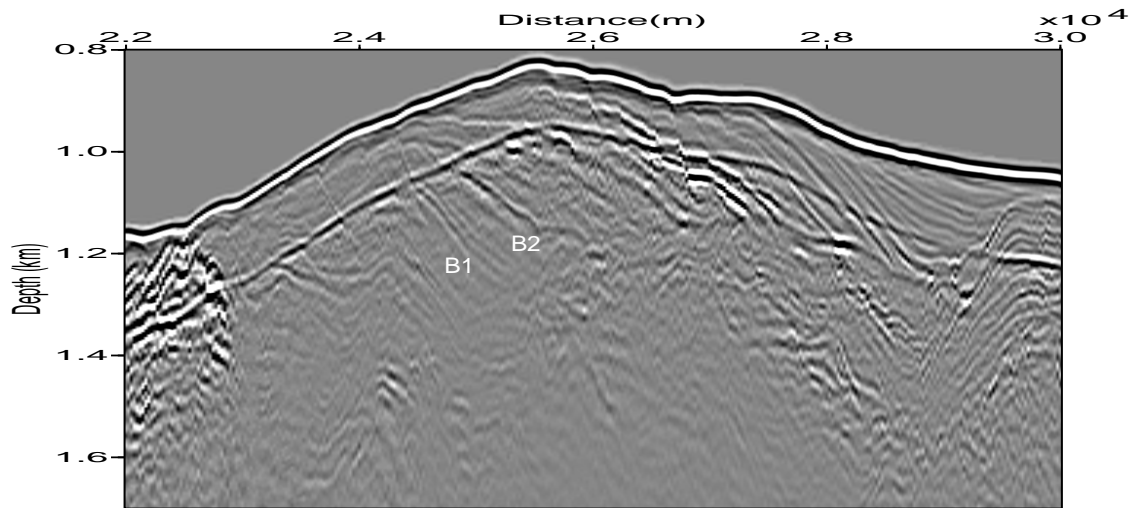


**Figure 5.4.** The AP migration result of seismic line OR89-02 using a relatively sparse migration-grid. The increment of the horizontal grid is 25 m and the increment of the vertical grid is 5 m.

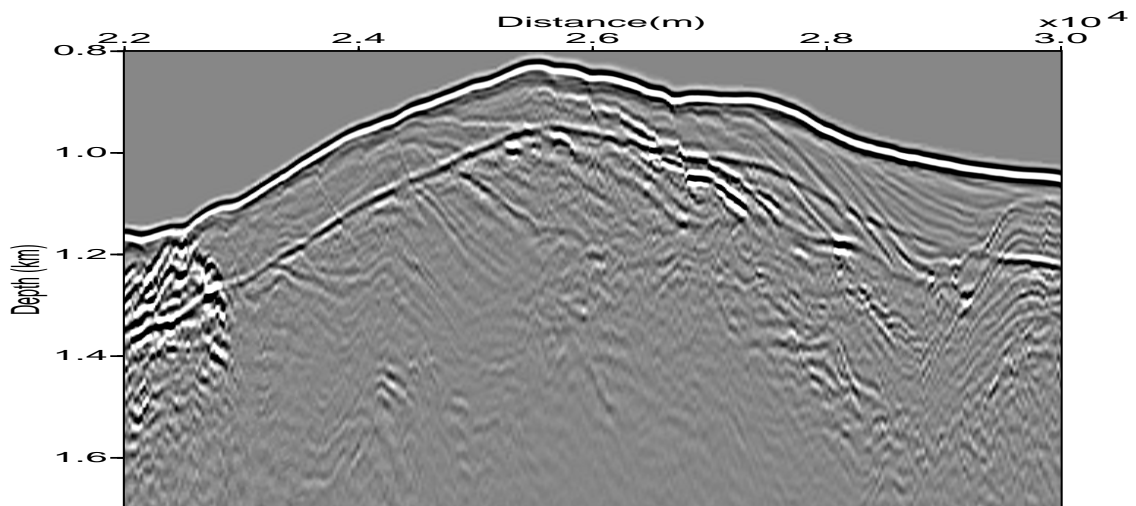


**Figure 5.5.** The AP migration result of seismic line OR89-02 using a fine migration-grid. The increment of the horizontal grid is 12.5 m and the increment of the vertical grid is 5 m.

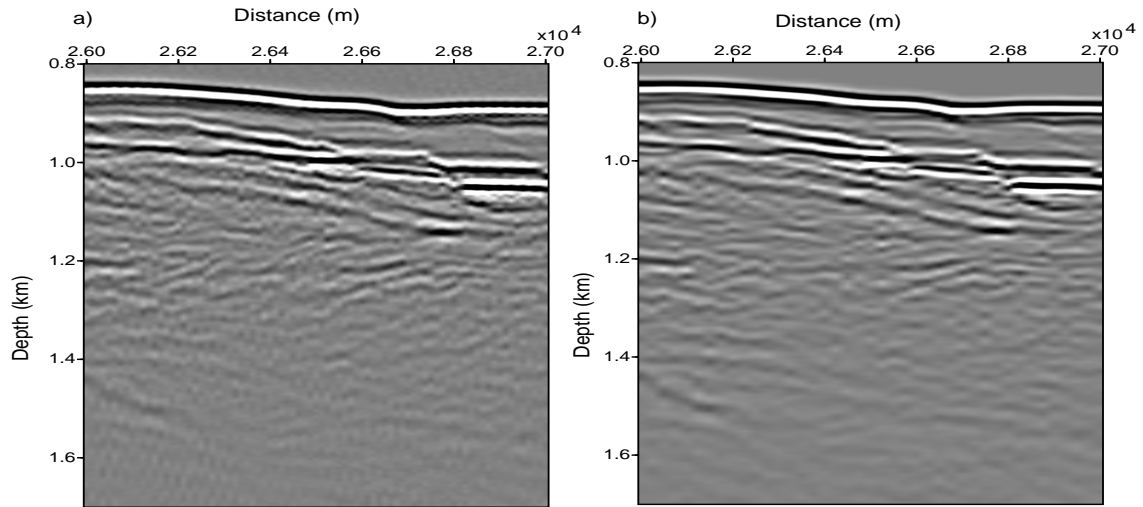


**Figure 5.6.** Comparison of the AP migration result in which the amplitude and phase information are not considered (a) and are considered (b) by the focusing operator.

B2) show higher amplitudes compared to the adjacent stratigraphic events. These bright sections show a negative polarity. Moreover, complex structures around the summit of Hydrate Ridge, such as faults that cut across the BSR, are also clearly imaged. Although a sparse migration-grid is used, its clarity is comparable with Figure 5.5, which uses a finer migration-grid.

A clear improvement to the result shown in Figure 5.4 can be achieved by applying a finer migration-grid. In principle, the AP migration is able to produce a finer grid of the migration output, both lateral and vertical grid, without using a fine sampling of the recording surface. However, the use of a fine migration-grid will be extremely computer-intensive.

Figure 5.5 shows the migration result using a fine migration-grid. The increment of the horizontal grid is 12.5 m and the increment of vertical grid is 5 m. The focusing operator, which covers the full offset of 6-km wide, consists of 841 traces. As a consequence, the computation time is twice that of the sparse migration-grid. However, the migration result is much better than the previous image (Figure 5.4). The use of a finer migration-grid is improving the spatial resolution.

Another test to see the effects of the amplitude and phase information on the migration

result is performed on the small part of seismic line OR89-02 from lateral distance of 26000 m to 27000 m. The result is demonstrated in Figure 5.6. The figure shows the comparison of the AP migration result in which the focusing operators are not consider a) and consider b) the amplitude and phase information. If the focusing operator does not consider the amplitude and phase information, then the amplitude is assumed to be one and the phase is assumed to be zero. The difference between the two images is clearly visible. The image in Figure 5.6a. looks noisy, particularly in the lower part of the section. This is because the geometrical spreading effects are not well compensated. This test shows that the quality of the migration result is strongly dependent on the accuracy of the focusing operator.

### 5.3.2 Comparison to Other Migration Methods

Figure 5.7 shows the comparison of the AP migration result to a Kirchhoff migration using maximum-amplitude traveltimes and the finite difference shot-profile migration that are generated using commercial software packages. Both methods, Kirchhoff migration and the finite difference shot-profile migration, are not taking into account the amplitude and phase information. However, intensive attention to the amplitude preservation is given by applying a geometrical spreading correction prior to the migration process.

The result of the Kirchhoff migration is displayed in Figure 5.7a. In general, this method produces a good image in terms of lateral continuity and structural definition. Almost all features, especially the BSR reflections, are visible along the section. However, the image does not show good recovery of correct relative reflectivities. The brightness of the amplitude reflections is strongly reduced in this image. Moreover, the seafloor reflection is slightly blurred. The lobe of the wavelet, which is indicated with black color, is not clearly separated. In addition, this method requires extensive smoothing of the slowness model to ensure stability, since in its implementation the method makes use of an asymptotic approximation that is valid only for high frequencies.

Figure 5.7b is the result of the finite difference migration. This method produces a good structural image by recursively downward-continuing source and receiver wave fields for all frequencies using explicit finite difference extrapolators. The image also shows good recovery of correct relative reflectivities and a slightly 'crisper' image than using Kirchhoff

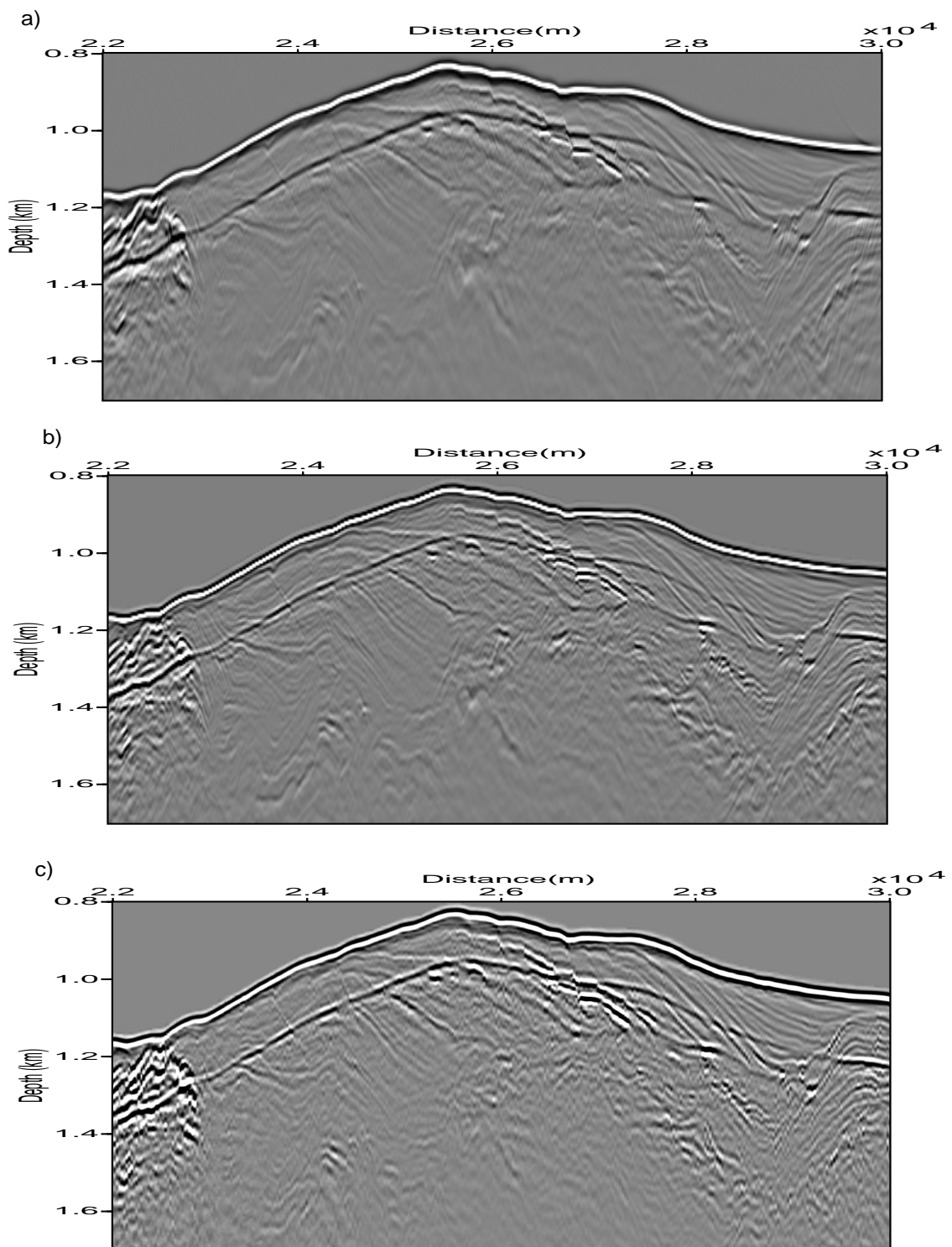


**Figure 5.7.** Comparison of migration results of seismic line OR89-02 using Kirchhoff migration (a), the finite difference migration (b), and the AP migration (c).

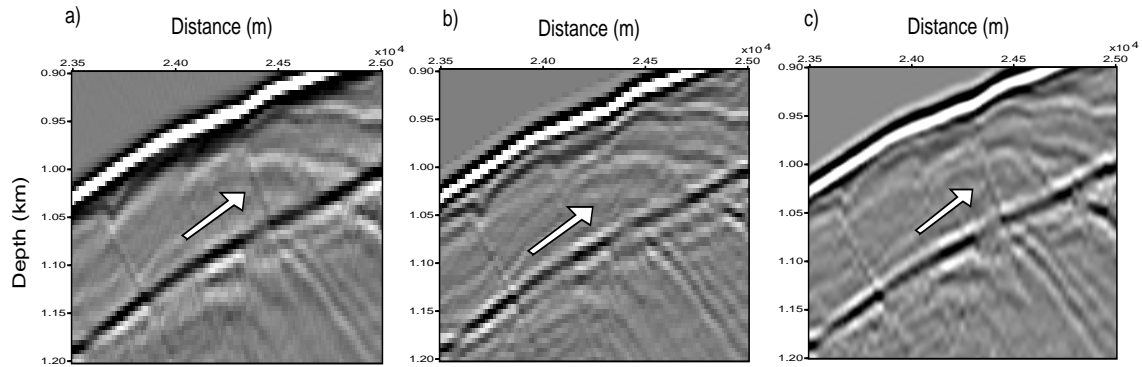


**Figure 5.8.** Closeup comparison in the region ( $x=23500$  m -  $25000$  m,  $z=900$  m -  $1200$  m) of Kirchhoff migration (a), the finite difference migration (b), and the AP migration (c). Arrow indicates the event that is missing in the finite difference migration image.

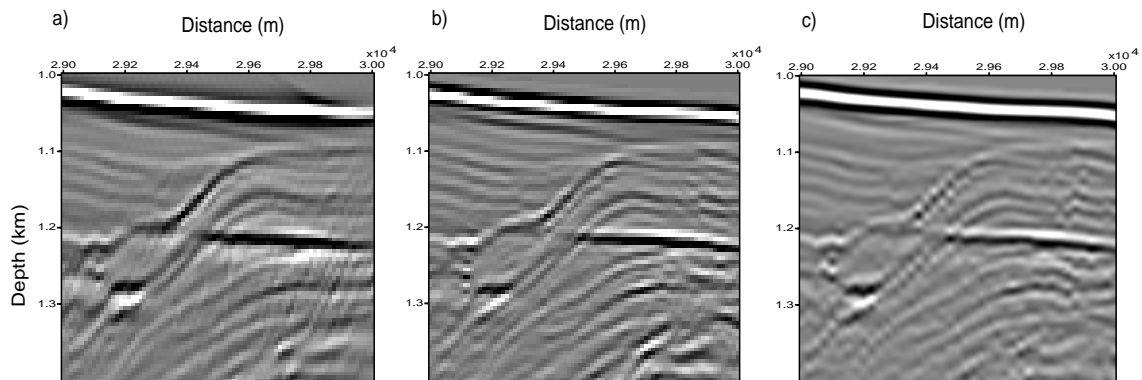


**Figure 5.9.** Closeup comparison in the region ( $x=29000$  m -  $30000$  m,  $z=1000$  m -  $1300$  m) of Kirchhoff migration (a), the finite difference migration (b), and the AP migration (c).



migration. The problem with this method is that it is an expensive process because it extrapolates every frequency to all depths and it requires a regular fine sampling of the recording surface.

Figure 5.7c shows the AP migration result in which the focusing operators involve the amplitude and phase information obtained by Band limited Green's function algorithm. This result is comparable to the image in Figure 5.7b, the output of the finite difference shot-profile migration. This figure shows a good recovery of correct relative reflectivities, which are shown in each reflector. The implementation of the AP migration does not require extensive smoothing of the slowness model. Moreover, no fine sampling of the recording surface is needed.

The closer comparison of three migration results in the region ( $x=23500$  m -  $25000$  m,  $z=900$  m -  $1200$  m) is displayed in Figure 5.8. In this image it is observed that the event, which looks like a fault across the BSR reflection to the seafloor (indicated by the arrow), is not clearly imaged in Kirchhoff migration and is completely missing in the finite difference migration, but is, however, clearly seen in the AP migration. On the other hand, the AP migration produces a smoother image compared to the Kirchhoff migration and the finite difference migration.

Another closer comparison in the region ( $x=29000$  m -  $30000$  m,  $z=1000$  m -  $1300$  m) is displayed in Figure 5.9. The Kirchhoff migration shows a poor image compared to the finite difference migration and the AP migration. However, the continuity of the reflectivities is not clearly seen in the finite difference migration. In this target area, the AP migration shows a much better image compared to the Kirchhoff migration and the finite difference migration.

### 5.3.3 Angle-Dependent Reflectivity Gathers

The variation of reflection coefficients with incidence angle, which is the basis of an AVA analysis, is commonly known as angle-dependent reflectivity. It can be used as a direct hydrocarbon indicator (Ostrander, 1984). As discussed in Chapter 3, the angle-dependent reflectivity is obtained using the bifocal version of the AP migration. In implementation, the angle-dependent reflectivity is used to examine the local BSR AVA response.

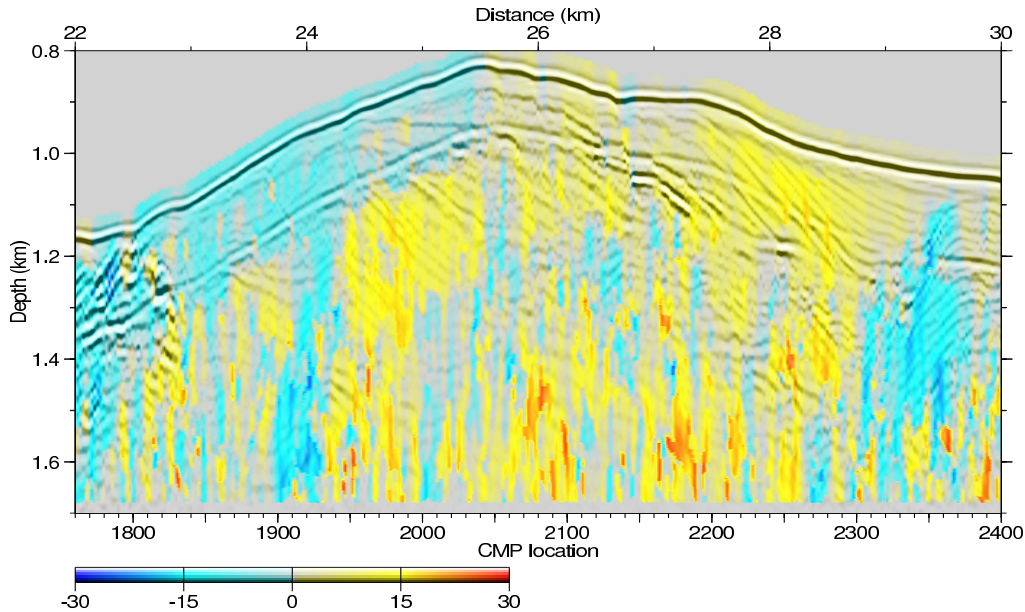


**Figure 5.10.** The dip-angle field, which is used to correct for the angle-dependent reflectivity gathers from the reflector dip effects.

As described at Chapter 4, if a grid-point is situated on a dipping reflector, the local dip-angle will influence the amplitude distribution along the depth sample, resulting in an incorrect position of the amplitude distribution. The shift of the amplitude distribution has also been observed by Berkhout (1997b). Therefore, prior to the examination of the local AVA response, a dip correction must be applied to the angle-dependent reflectivity gather to move the amplitude distribution to its correct position.

To correct for the effect of the reflector dip on the angle-dependent reflectivity gather, the dip-angle field is required. The dip-angle field is estimated for each depth sample throughout the migrated section. In principle, the dip-angle estimation is carried out based on the migrated section by using the adaptive filtering, which filters the data with a set of dip filters and performs a weighted stack of the dip filtered data. Thereafter, the filtering process is followed by coherency filtering to make a dip analysis within a specified depth. Six adjacent traces (three each side) of the specified trace are considered to estimate the trend of the dips. The selected dips are then evaluated and the dip direction with the highest signal strength is chosen.

The result of the dip-angle field estimation is shown in Figure 5.10. As described in

Chapter 4, a dip sign convention, from left to right, events with downdip to the right are assigned positive dip, while events with updip to the right are assigned negative dip. The dip-angle ranges from -30 to 30 degrees. The left part of the section, following the seafloor and the BSR, shows a negative dip-angle, as indicated by the dip of each event. The two events below the BSR, which are labeled B1 and B2 in Figure 5.4, show a positive dip-angle. In contrast, the right part of the section shows a positive dip-angle with exception in the region close to the dome structure (around a lateral distance of 29200 m).

In the following, it is demonstrated how the effect of the reflector dip is corrected. Figure 5.11 shows the angle-dependent reflectivity gather before and after dip correction. As a reference, consider the seafloor reflection. Figure 5.11a shows uncorrected angle-dependent reflectivity gathers with a different dip-angle. The left panel of Figure 5.11a shows the reflectivity gather at a lateral distance of 24200 m in which the seafloor reflection has a negative dip-angle (-5 degrees). This dip-angle causes the amplitude distribution of the seafloor reflection to be shifted 5 degrees to the left side. In contrast, Figure 5.11d shows the reflectivity gather at a lateral distance of 27600 m in which the seafloor reflection has a positive dip-angle (7 degrees). This dip-angle causes the amplitude distribution of the seafloor reflection to be shifted 7 degrees to the right side.

The corrected reflectivity gathers are shown in Figures 5.11b and 5.11e for lateral distances of 24200 m and 27600 m, respectively. The amplitude distribution of both reflectivity gathers has been moved to its correct position. The shift in amplitude distribution to its correct position is presented in Figures 5.11c and 5.11f. The solid line represents the picked amplitude of the seafloor reflection before dip correction, whereas the dashed line represents the picked amplitude of the seafloor reflection after dip correction. Note that this correction is carried out based on the dip-angle of each depth sample.

After having corrected angle-dependent reflectivity gathers, several spots along the BSR are picked to examine the amplitude that corresponds to the seafloor and the BSR reflections. The angle-dependent reflectivity gather and the picked amplitudes of the seafloor reflection (solid line) and the BSR reflection (dashed line) at lateral distances of 24200 m, 25000 m, 26000 m and 27200 m are shown in Figure 5.12. For convenience in display, the negative amplitude of the BSR reflection is reversed. These locations are close to the

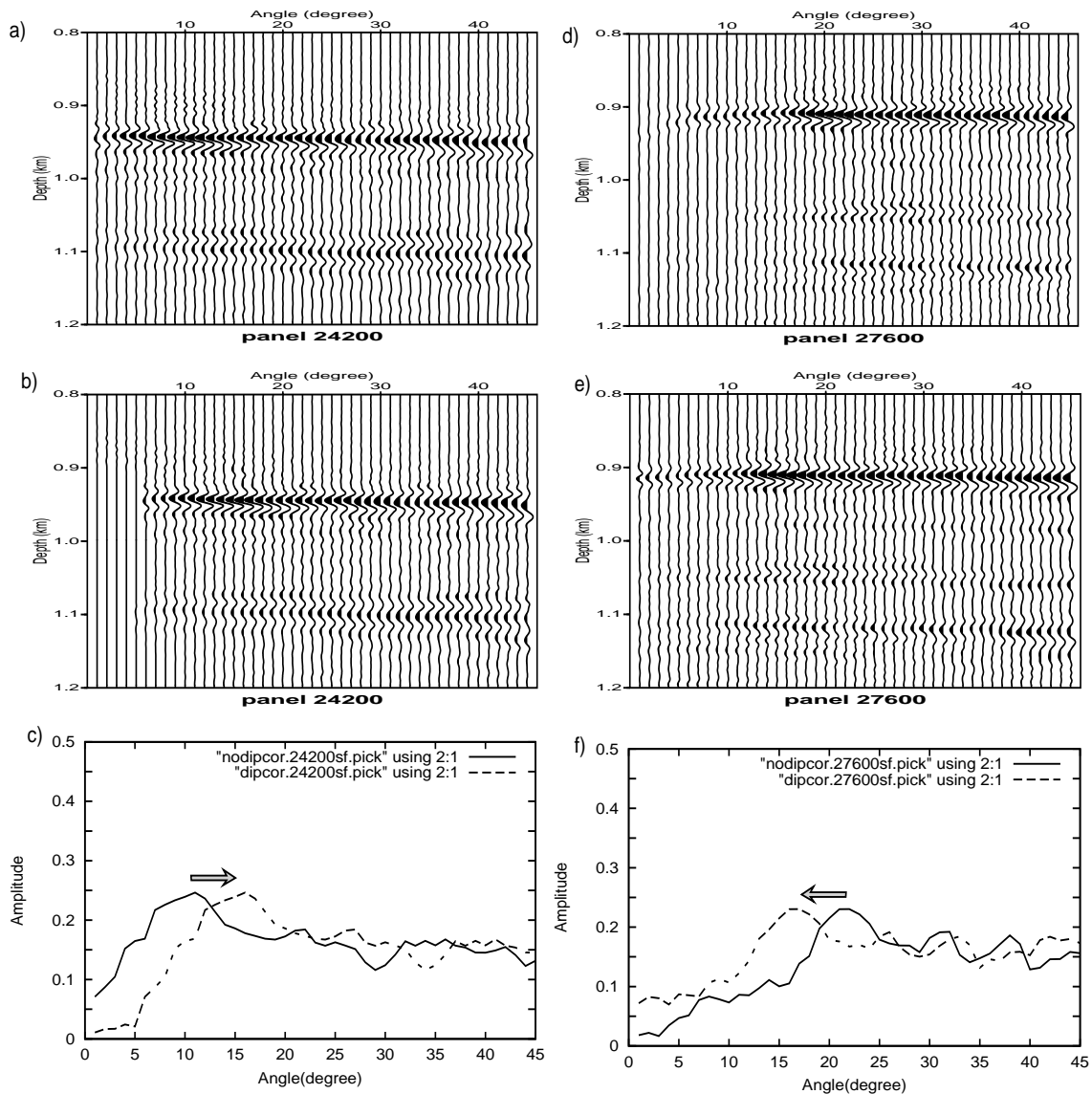


**Figure 5.11.** Angle-dependent reflectivity gather at lateral distance of 24200 m before dip correction (a), after dip correction (b) and the picked amplitude of the seafloor reflections before dip correction (solid line) and after dip correction (dashed line) (c). Another angle-dependent reflectivity gather at lateral distance of 27600 m before dip correction (d), after dip correction (e) and the picked amplitude of the seafloor reflection before dip correction (solid line) and after dip correction (dashed line) (f). Arrows indicate the shift direction of amplitude distribution.

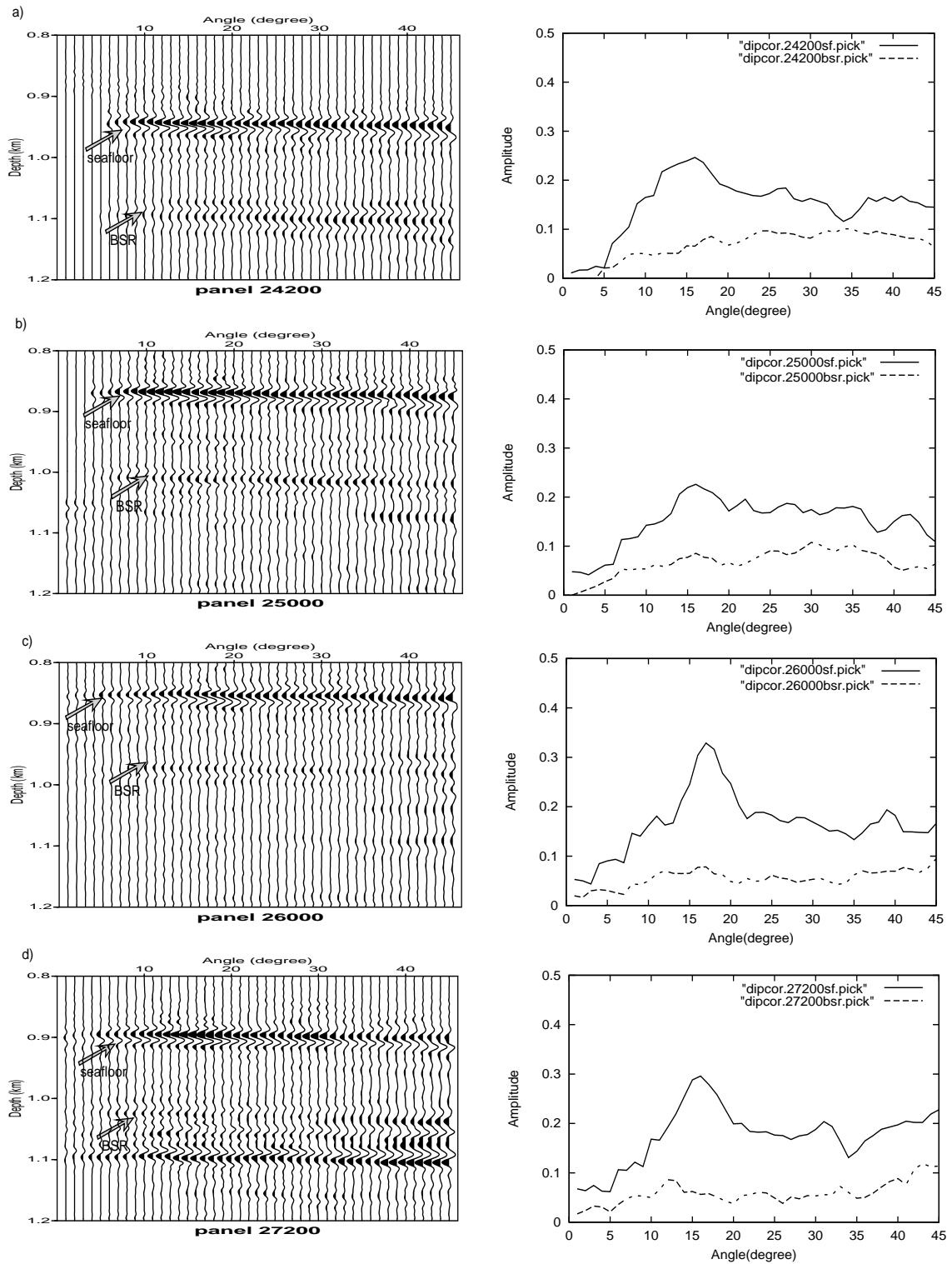


**Figure 5.12.** Angle-dependent reflectivity gather after dip correction and the picked amplitude of the seafloor reflection (solid line) and the BSR reflection (dashed line) at lateral distances of 24200 m (a), 25000 m (b), 26000 m (c), and 27200 m (d).

proposed well site, which will be drilled in the course of deep sea drilling ODP leg 204 (Bohrmann et al., 2002).

The angle-dependent reflectivity gather at a lateral distance of 24200 m is shown in Figure 5.12a. This gather is located in the relatively simple situation in which no significant event in the region between the seafloor and the BSR reflection is present. The BSR reflection is clearly identified. The picked amplitude of the BSR reflection at a depth of 1092 m indicates slightly increasing amplitudes as the angle increases. Note that the limited extent of the spread caused boundary effects (i.e., peak at an angle of 15 degrees and trough at angle of 35 degrees). These effects are displayed in all gathers. Figure 5.12b shows the angle-dependent reflectivity gather from continuation of the BSR at 25000 m distance. The appearance of the BSR reflection still can be identified, even though the gather shows a quite strong event in between the seafloor and the BSR reflection. The amplitude of the BSR reflection, which is picked at a depth of 1002 m, increases toward higher angles.

The angle-dependent reflectivity gather at 26000 m is shown in Figure 5.12c. The BSR reflection is weak and not clearly identified. Both regions above and below the BSR reflection contain several strong events, which are similar to the BSR reflection. These events may be caused by the complexity of the subsurface structure at this location. As displayed in Figure 5.5, the location of this gather coincides with the fault structure across the BSR and bright reflections underneath the BSR. However, based on the section in Figure 5.5, the BSR appearance can be picked at a depth of 968 m. The picked amplitude of the BSR is constant as the angle increases. Figure 5.12d shows the angle-dependent reflectivity gather at 27200 m distance. This location is also crossing the complex reflection events. The BSR AVA response, which is picked at a depth of 1015 m, indicates relatively constant amplitudes as the angle increases.

In general, the picked amplitudes of the BSR reflections show increasing amplitudes with increasing angle. However, in the complex structure, the BSR AVA response exhibits constant amplitudes with increasing angle. In contrast to the BSR response, the picked amplitude of the seafloor reflections are slightly decreasing as the angle increases. Based on the picked amplitude from the seafloor reflections and the BSR reflections, it can be seen that the AVA response is valid only in the region between incidence angles of 15 degrees

and 35 degrees. Therefore, this range of incidence angles (15 - 35 degrees) is considered as an input parameter to the AVA inversion.

#### 5.4 AVA Attributes

Numerous studies have demonstrated that AVA analysis is a diagnostic tool in hydrocarbon detection and delineation. AVA attributes are being used with more confidence outside of traditional low relief areas, as the amplitude-preserving prestack migration has resulted in significantly improved signal quality with better preservation of lithological information.

In principle, the AVA analysis involves three different scenarios concerning the amplitude variation with incidence angle (Castagna and Backus, 1993). Figure 5.13 shows the theoretical AVA curves corresponding to these three different scenarios. The first scenario is characterized by a large positive amplitude, which reduces to a smaller positive amplitude (curve 1), the so-called dim spot. The second scenario involves a phase reversal, which is indicated by a small positive amplitude changing to a small negative amplitude (curve 2). The last scenario is a bright spot, which is indicated by a negative amplitude increasing to an absolute larger negative amplitude (curve 3). These three scenarios can be directly related to changes in Poisson's ratio, indicating pore fluid transitions. One of these three scenarios that meets the BSR characteristic is the bright spot (curve 3), since the BSR is characterized by a negative reflectivity, then the zero-offset reflection amplitude can be expected to be negative. The BSR characteristic can be clearly seen on the AVA attributes image.

The local examination of AVA response by observing the change of amplitude reflections manually on the angle-dependent reflectivity gather is extremely inefficient, particularly for large data sets. In order to have a general insight of the AVA response in the area of interest, several different attributes describing the amplitude variation with incidence angle are defined. Most straightforward is the parameterization of the amplitude variation with incidence angle using the so-called AVA attributes.

The basic AVA attributes are given by the parameterization of the amplitude variation with incidence angle using the intercept of the fitted line with the amplitude axis and the gradient of a linear fit of amplitude versus the squared sine of incidence angle. The two

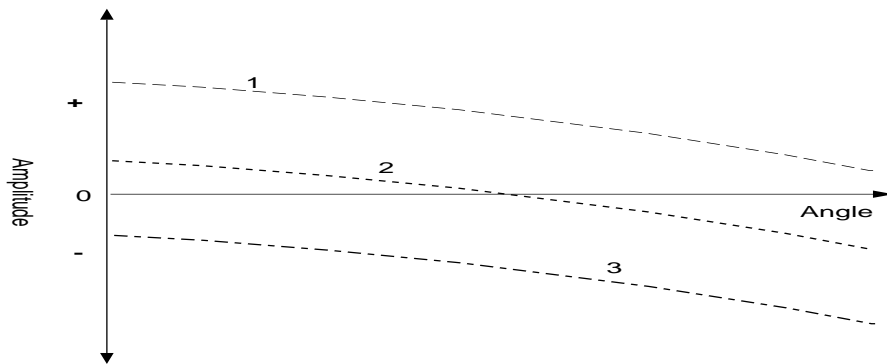


**Figure 5.13.** Theoretical AVA curves of three different scenarios; (1) dim spot, (2) phase reversal, and (3) bright spot (after Castagna 1993).

linear AVA attributes are related to the elastic properties of the subsurface (Cambois, 1998; Shuey, 1985). The intercept corresponds to the  $P$ -wave reflection coefficient, the so-called primary AVA attribute. The secondary AVA attribute is the gradient, which is a complex function of  $P$ - and  $S$ -velocities,  $P$ - and  $S$ -reflection coefficients and density contrast.

The AVA gradient describes whether the amplitude is increasing or decreasing as the incidence angle increases. Special attention must be given, however, when amplitudes vary from high positive values to small positive values, the gradient will be negative, while for the mirror situation, i.e., high negative amplitudes move to small negative ones, the gradient will show a positive value. Therefore, it is much better to estimate the AVA attributes by capturing the energy envelope. The energy envelope will show a negative sign in both situations described above, indicating decreasing amplitudes, and will be positive in case of increasing amplitudes. As a consequence, the intercept of both situations will be positive. In case of phase reversal, the gradient is not well defined by the energy envelope. For this purpose, all traces within the angle-dependent reflectivity gather are transformed to complex traces to produce angle-dependent envelope gathers.

In this section, the intercept and AVA gradient of the area of interest, which is marked by a rectangle (see Figure 5.2), are directly estimated from the angle-dependent envelope gather. These two attributes are derived using a least squares line fit to the trace amplitudes versus incidence angle at each depth sample as follows (after Shuey, 1985):



$$R(\theta, z) = I(z) + G(z)\sin^2[\theta(x, z)] \quad (5.1)$$

where  $R$  is reflection coefficient,  $I$  is AVA intercept, and  $G$  is AVA gradient.  $x$ ,  $z$ , and  $\theta$  indicate trace offset, depth, and angle of incidence, respectively.

In addition, AVA interpretation is facilitated by two subsurface images (the intercept and gradient). This approximation holds where  $0 < \theta < 35$  degrees and therefore the range 0 - 35 degrees that represents the range of incidence angles to be considered. However, based on the local examination of BSR AVA response as presented in the previous section, in which the reflection amplitudes for incidence angles of less than 15 degrees are lacking, the AVA attributes are then estimated in the range of 15 - 35 degrees.

The two additional subsurface images of the AVA attributes are shown in Figure 5.14. From top to the bottom, the intercept a) and the AVA gradient b) are shown color-coded indicating their magnitude. These two images must always be considered simultaneously to unambiguously identify AVA anomalies generated by the presence of gas or hydrocarbons.

The intercept image (Figure 5.14a) shows a positive value, which is ranging from magnitude 0 to 0.48. This is because the AVA attributes are estimated using the envelope energy. However, each depth point in the subsurface yields a different value. This value can be viewed as deviation from the background, which is related to hydrocarbons or lithological factors. This intercept image is also important to conduct the AVA modeling of amplitudes.

The gradient image shown in Figure 5.14b is used to classify the scenario of response from each interface. The seafloor response, which shows a higher intercept value compared to the BSR and the other events throughout the area of interest, yields a negative gradient. Therefore, the seafloor response can be classified as dim spot. The same response is shown by the two events below the BSR at a lateral distance of about 25 km. They show a negative gradient, indicating the reflection coefficients of these events decrease as the angle increases. The AVA responses of these events are also dim spots. In contrast, the BSR shows strong AVA anomalies, as indicated by positive gradients. Therefore, the AVA response of the BSR can be classified as a bright spot. In the case where the BSR is characterized by increasing amplitudes for increasing incidence angles, the BSR results from hydrate-bearing sediment overlying gas-saturated sediment (Ecker, 2001).

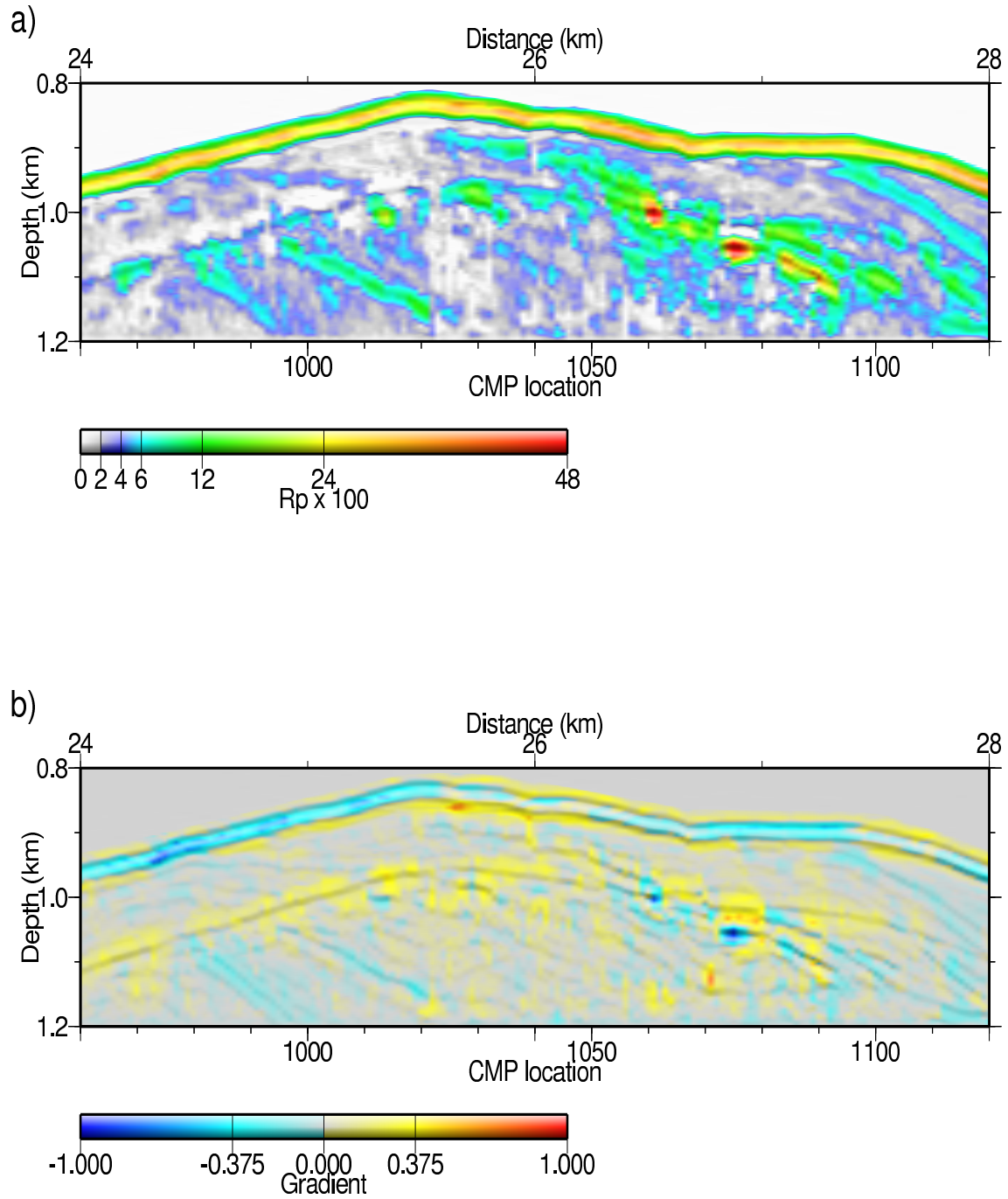


**Figure 5.14.** AVA attributes consist of intercept a), and gradient b).

## 5.5 AVA Modeling

The AVA modeling of the seafloor and the BSR are carried out in order to estimate the possible (lithological) properties of the subsurface. The effects of different elastic properties on the seafloor and the BSR are explored in an attempt to match the synthetic AVA response with the observed seismic data. Synthetic AVA responses of the seafloor and the BSR are calculated using Zoeppritz' equations for elastic models, which are varied until an acceptably close match is obtained between computed and observed AVA curves. The resulting models are expected to be able to explain the possible causes of the seafloor and the BSR responses.

In this AVA modeling, the amplitude effects of the observed data (i.e., the picked migration amplitudes at four different locations), which are shown in Figure 5.12, are analyzed to examine the actual prediction of the models. Four locations of the observed data are shown in Figure 5.15b, which are indicated by a white-line crossing the migrated section.

Generally, the two angle-dependent reflectivity gathers at lateral distances of 24200 m and 25000 m display similar AVA trends, both for the seafloor and the BSR responses. The BSR reflection is clearly identified for all angles. The AVA trend of the BSR displays increasing amplitudes with increasing angle. In contrast, the AVA trend of the seafloor shows decreasing amplitudes with increasing angle. Therefore, these two angle-dependent reflectivity gathers (at 24200 m and 25000 m) can be explained by the same model. On the other hand, the BSR AVA curves of the two angle-dependent reflectivity gathers at lateral distances of 26000 m and 27200 m exhibit nearly constant amplitudes with increasing angle. Since these two regions exhibit the complex structures, their amplitudes might suffer superpositions or interference effects. Therefore, based on the observed data in the area of interest, the AVA modeling of the BSR response is performed based on the two amplitude effects: increasing amplitudes with increasing angle and nearly constant amplitudes with increasing angle.

In the first attempt, the AVA behavior of the two angle-dependent reflectivity gathers at lateral distances of 24200 m and 25000 m is modeled. The AVA modeling is started with the seafloor response and followed with the BSR response. The predicted physical parameters of the seafloor and the BSR models are shown in Figure 5.15a. The P-wave velocities

(black-line) are taken from the migration velocity (Figure 5.3), which are consistent with the estimated velocity at the northern part of Hydrate Ridge (Trehu and Flueh, 2001). The S-wave velocities (green-line) are estimated by assuming a Poisson's ratio of unconsolidated sediments (0.35-0.4), which corresponds to sediments typical of this region. The densities are varied from 1 g/cc at the sea water to 1.92 g/cc at the sediments below the BSR.

The resulting AVA curve is calculated using Zoeppritz' equations and is compared to the one observed at a lateral distance of 24200 m (Figure 5.16). The comparison of the modeled AVA response and the migrated image indicates that this model successfully reproduces not only the zero angle data but also the AVA trend of the seafloor and the BSR responses. This synthetic AVA curve also agrees well with another one observed at a lateral distance of 25000 m, which is shown in Figure 5.17. The agreement of the synthetic AVA curve with the two observed AVA trends at lateral distances of 24200 m and 25000 m confirms the first prediction. These two regions are represented with the same model.

The estimated seafloor interface model indicates that the AVA behavior of the seafloor response is caused by a positive impedance contrast between the sea water and the sediments underneath. The resulting velocities are reasonable, which is consistent with a Poisson's ratio of 0.5 for the sea water and 0.45 for the seafloor sediments.

In addition, the BSR interface model generally conveys that the BSR response is caused by a negative impedance contrast between the sediments containing methane hydrates and the underlying sediments, which are either brine or gas saturated. Looking at the resulting P-wave velocities of 1.6 km/s and 1.38 km/s for above and below the BSR, respectively, the model suggests that the layer below the BSR is composed of free gas saturated sediments. Referring to Carcione and Tinivella (2000), the P-wave velocity of 1.38 km/s corresponds to sediment properties with 20 % free gas saturation. However, the P-wave velocity of 1.6 km/s above the BSR suggests low (1%) hydrate concentration. The obtained S-wave velocities of this model slightly increase and practically are independent of hydrate concentration. These S-wave velocities are consistent with unconsolidated sediments and a non-cemented gas hydrate model (Carcione and Tinivella, 2000; Ecker et al., 1998). These velocities represent a Poisson's ratio of 0.43 for the sediments above the BSR and 0.39 for the sediments underneath.

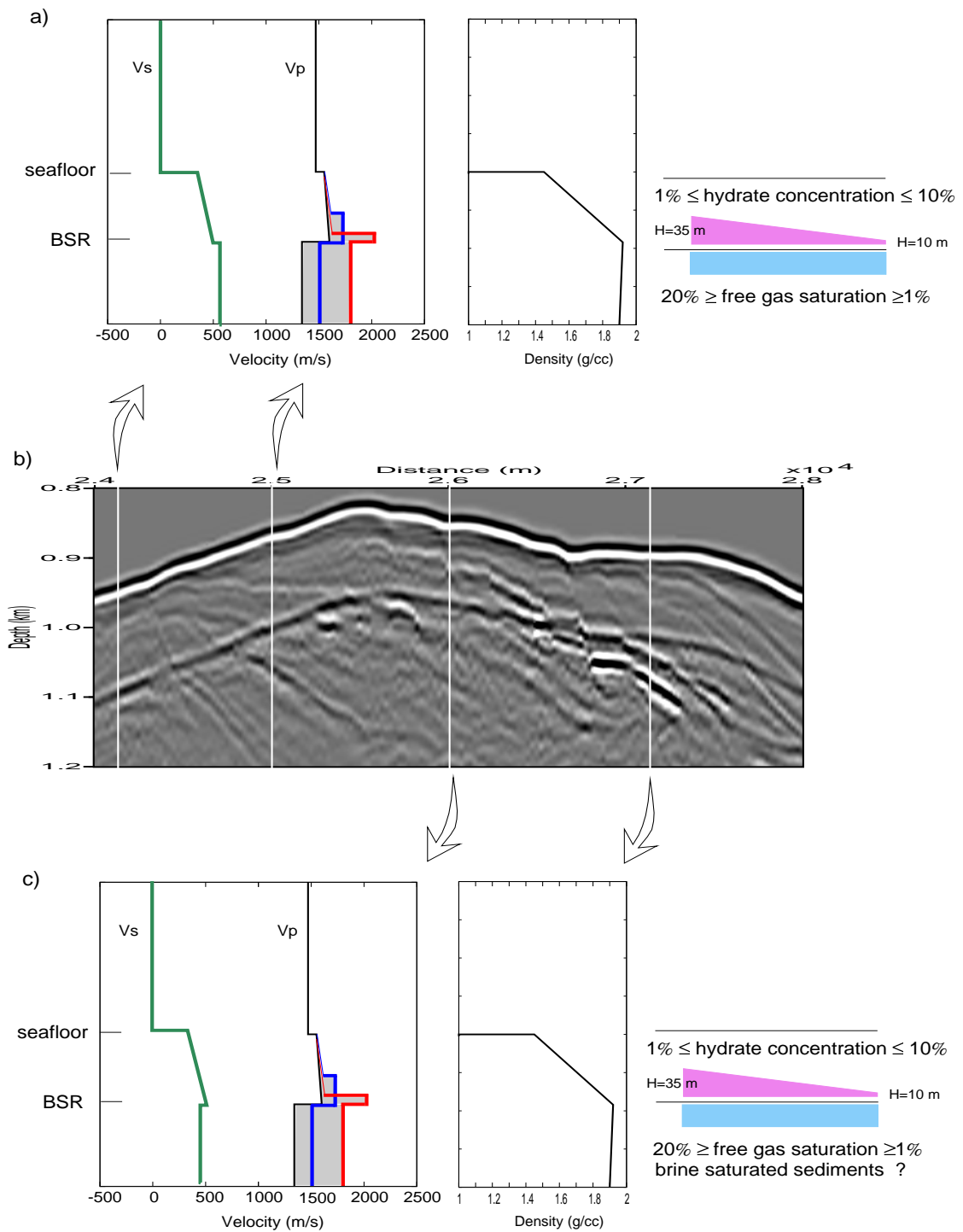


**Figure 5.15.** The estimated models for the observed AVA curves at lateral distances of 24200 m and 25000 m a) and at lateral distances of 26000 m and 27200 m c). The locations of the observed data are indicated by white lines superimposed on the migrated section b).

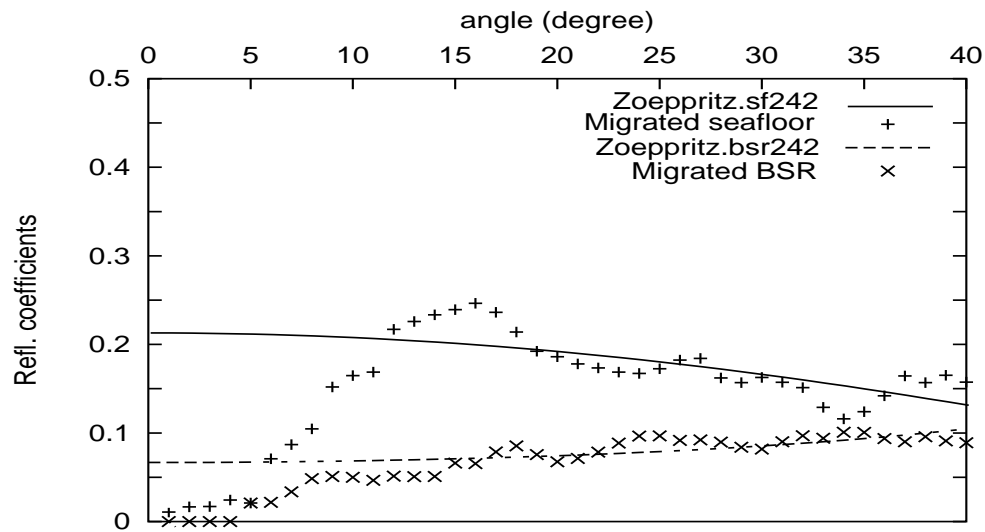


**Figure 5.16.** Comparison of the AVA curve calculated using Zoeppritz' equations based on the model (Figure 5.15a) with the AVA curve of the migrated angle-dependent reflectivity gather at a lateral distance of 24200 m.

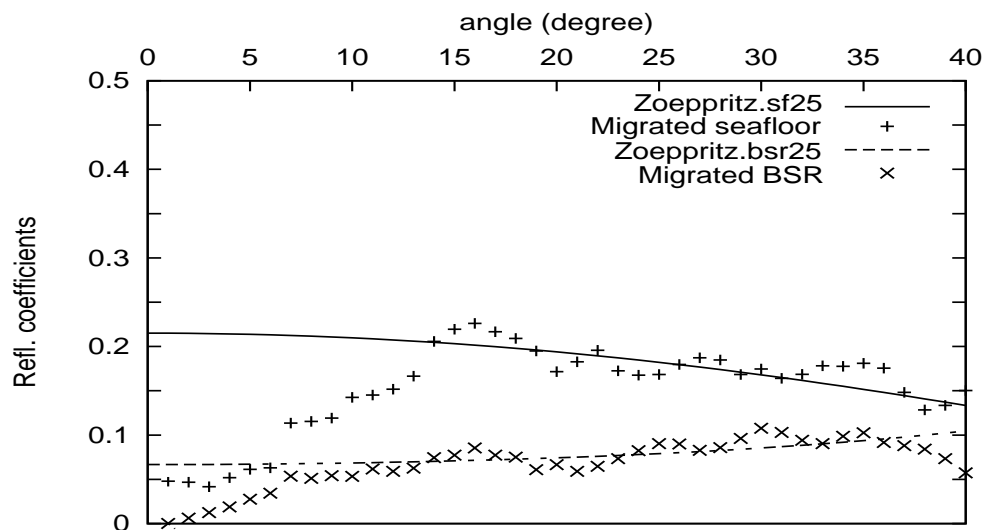


**Figure 5.17.** Comparison of the AVA curve calculated using Zoeppritz' equations based on the model (Figure 5.15a) with the AVA curve of the migrated angle-dependent reflectivity gather at a lateral distance of 25000 m.

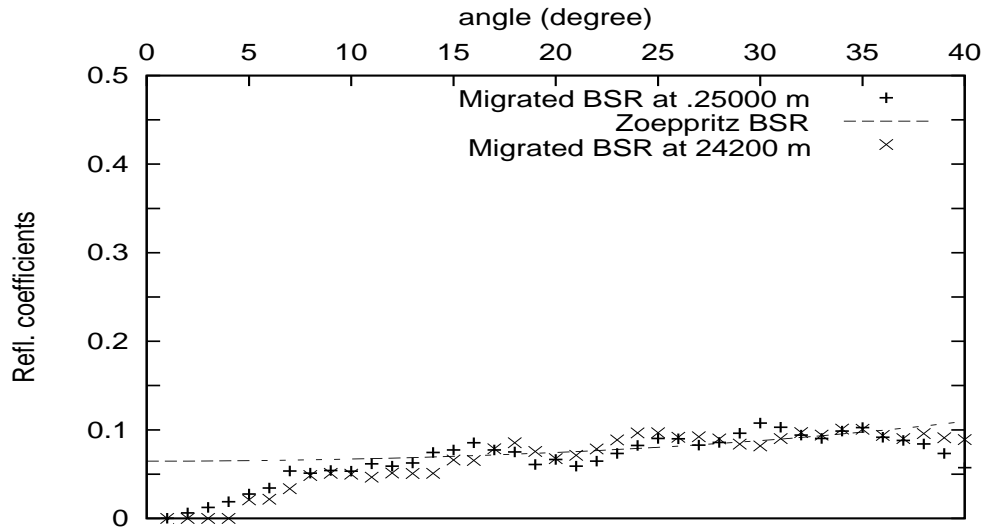


**Figure 5.18.** Comparison of the BSR AVA curve calculated using Zoeppritz' equations based on the increasing of P-wave velocities, which are illustrated in Figure 5.15a by a red-line, with the two AVA curves of the migrated angle-dependent reflectivity gather at lateral distance of 24200 m and 25000 m.

Particularly, the resulting model for representing the BSR response is inherently non-unique. This non-uniqueness can be demonstrated by increasing the P-wave velocities above and below the BSR and keeping the impedance contrast constant. The S-wave velocities and the densities are the same as the previous model (Figure 5.15a), which follows a non-cemented gas hydrate model (Ecker et al., 1998; Carcione and Tinivella, 2000). The increasing of P-wave velocities are illustrated in Figure 5.15a by a red-line. As a consequence, the hydrate layer above the BSR must be modeled by thin layer in order to fulfill the mean P-wave velocity of the layer between the seafloor and the BSR.

The synthetic BSR AVA curve, which is illustrated in Figure 5.18, shows a good agreement with the two observed AVA curves at lateral distance of 24200 m and 25000 m. Based on the agreement of these AVA curves and the fairly unchanged Poisson's ratio is defined above and below, thus, the model would suggest hydrate over sediments with low free gas saturation. The resulting P-wave velocity (2.05 km/s) above the BSR strongly suggests the presence of a high (10%) concentration of hydrate. In contrast, the sediment layer below the BSR, which is indicated by a P-wave velocity of 1.78 km/s, represents low (1%) free gas saturation.

Based on the resulting model, there are two extreme possibilities: the BSR response is probably caused by an interface separating a) sediments with low hydrate concentration and sediments with high free gas saturation, or b) sediments with high hydrate concentration and sediments with low free gas saturation. Both conditions match the AVA curve of the observed data. Assuming the predicted average P-wave velocity of the layer between the seafloor and the BSR has an error of 2%, then the thickness of the hydrate layer with P-wave velocity of 2.05 km/s (indicated by a red-line in Figure 5.15a) will be 10 m to fulfill the mean P-wave velocity. In addition, the hydrate layer with P-wave velocities of 1.7 km/s (blue-line) will have a maximum thickness of 35 m. As a consequence, the first possibility suggests that low hydrate concentration must be trapped in a thicker layer within the depth range between the seafloor and the BSR. Conversely, the second possibility conveys that the layer with high hydrate concentration must be thin in the thickness range from 10 m to 35 m, otherwise the predicted P-wave velocity in disagreement with the migration velocity (1.6 km/s). In case that the hydrate layer is thin, then a waveform change must be visible at the BSR response. Further study on the waveform analysis is required to provide a more accurate interpretation.

In order to emphasize the effects of the different thickness of the hydrate layer on the waveform response, the synthetic seismograms, which are calculated based on the variation of the P-wave velocity of the hydrate layer, are modeled. The resulting waveform response is then compared to the waveform of the observed data. Figure 5.19 shows the resulting synthetic seismograms. The first and the second reflection represent the response of the seafloor and the BSR, respectively. The BSR response of the hydrate layer with P-wave velocity of 2.1 km/s and the estimated thickness of 10 m, which is illustrated in Figure 5.19a, shows the waveform change clearly. Obviously, the thin layer introduces a waveform change. The waveform change still can be observed up to a hydrate thickness of 35 m with the P-wave velocity of 1.7 km/s (Figure 5.19e). No one of the effects of the hydrate thickness match with the observed data (Figure 5.19g), only the response of the hydrate layer with P-wave velocity of 1.6 km/s match with the observed data. This means that the existence of the thin layer with high hydrate concentration may be neglected. Therefore, the non-uniqueness factor can be minimized by neglecting the second extreme possibility.



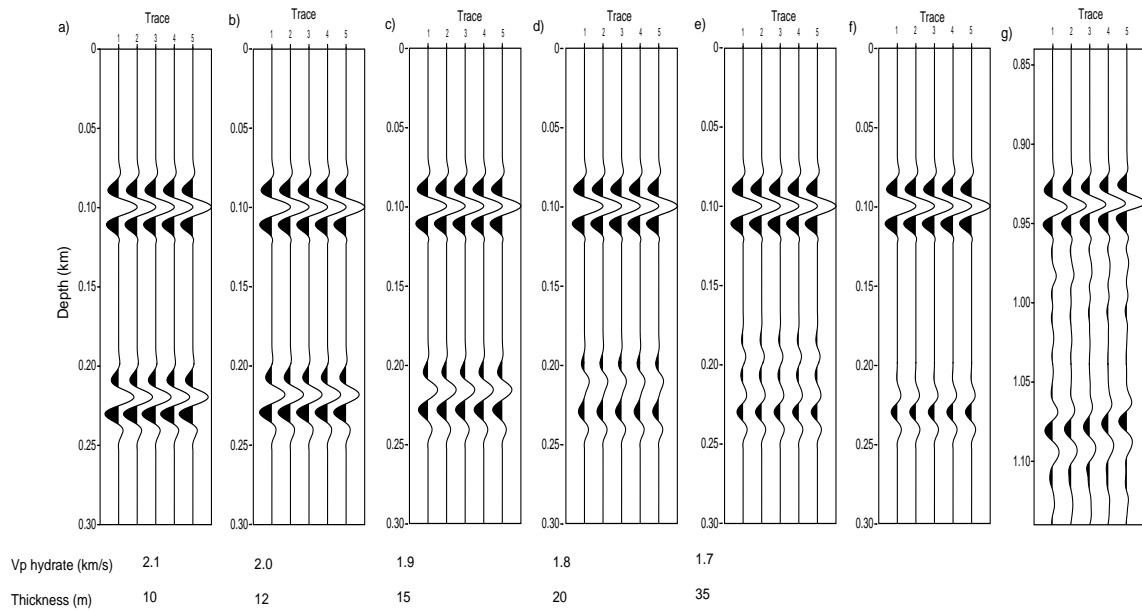


**Figure 5.19.** The effects of the different thickness of the hydrate layer on the waveform, which are estimated based on the P-wave velocity of the hydrate layer of 2.1 km/s a), 2.0 km/s b), 1.9 km/s c), 1.8 km/s d), 1.7 km/s e), and no thin hydrate layer f). The observed data are taken from the migrated image around a lateral distance of 24200 m g).

Based on this analysis, the reasonable conclusion for this region is suitable to the first possibility that the BSR response is caused by an interface separating sediments with low hydrate concentration and sediments with high free gas saturation.

In the next attempt, the same procedures are applied to model the AVA response of the migrated angle-dependent reflectivity gathers at lateral distances of 26000 m and 27200 m. In particular for the BSR response, the second amplitude effects in which the amplitudes are nearly constant with increasing angle are modeled. The estimated elastic parameters of the seafloor and the BSR model are shown in Figure 5.15c. The P-wave velocities (black-line) are again taken from the migration velocity (Figure 5.3). The S-wave velocities (green-line) are also determined by assuming a Poisson's ratio of unconsolidated sediments (0.4), which corresponds to sediments typical of this region. The densities are also varied from 1 g/cc at the sea water to 1.92 g/cc at the sediments below the BSR.

The resulting synthetic AVA curve corresponding to this model is again calculated using Zoeppritz' equations. It is compared to the observed AVA behavior at a lateral distance of

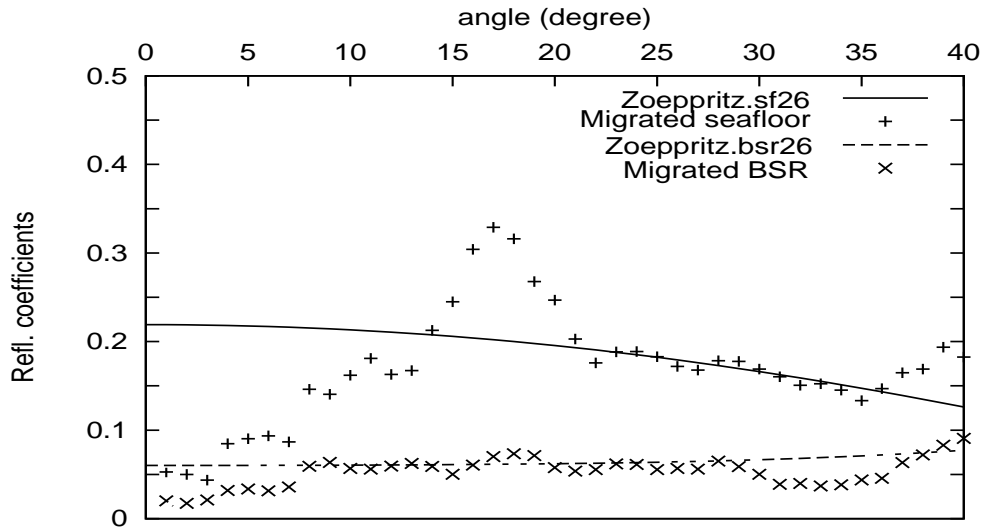


**Figure 5.20.** Comparison of the AVA curve calculated using Zoeppritz' equations based on the model (Figure 5.15c) with the AVA curve of the migrated angle-dependent reflectivity gather at lateral distance of 26000 m.

26000 m, which is shown in Figure 5.20. The comparison shows that this model completely reproduces the AVA trend of the seafloor and the BSR responses. The good agreement is also exhibited by the AVA synthetic curve with the observed AVA trend at a lateral distance of 27200 m as shown in Figure 5.21. Both the seafloor and the BSR responses at lateral distances of 26000 m and 27200 m are represented with the same model.

In general, the seafloor responses from the observed angle-dependent reflectivity gathers, which are located at different lateral distances, can be explained by the same model. The second amplitude effects of the BSR response, which are nearly constant with increasing amplitudes, indicate that the BSR response corresponds to a negative P-wave velocity contrast. The correspondence between the synthetic and the observed BSR AVA curves suggest that there exists a small decrease in S-wave velocity across the BSR.

The resulting model of the BSR response is also non-unique. This non-uniqueness is also demonstrated by increasing the P-wave velocities above and below the BSR as indicated by a red-line in Figure 5.15c. The S-wave velocities and the densities are the same as in the previous model (Figure 5.15)c. The synthetic BSR AVA curve, which is illustrated in Figure 5.22, shows a good agreement with the two observed AVA curves at lateral distances

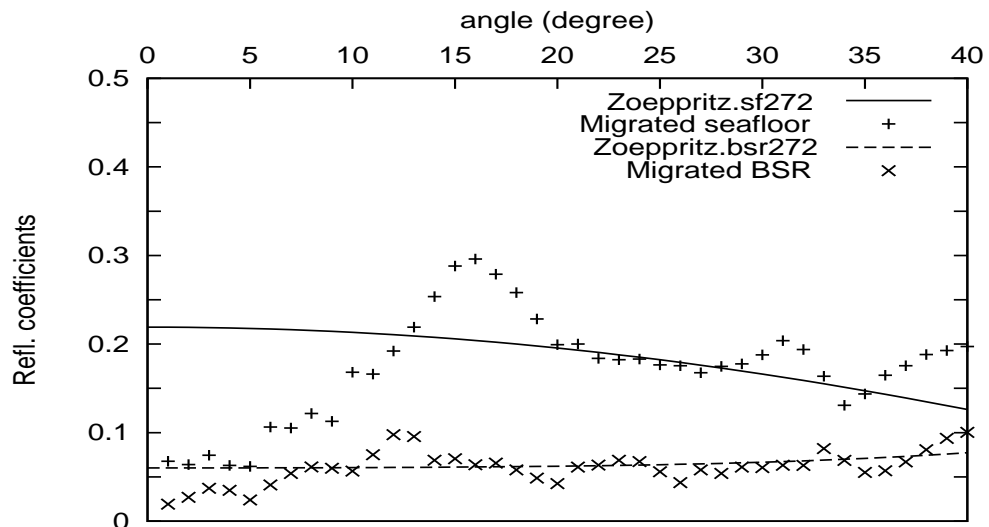


**Figure 5.21.** Comparison of the AVA curve calculated using Zoeppritz' equations based on the model (Figure 5.15c) with the AVA curve of the migrated angle-dependent reflectivity gather at lateral distance of 27200 m.

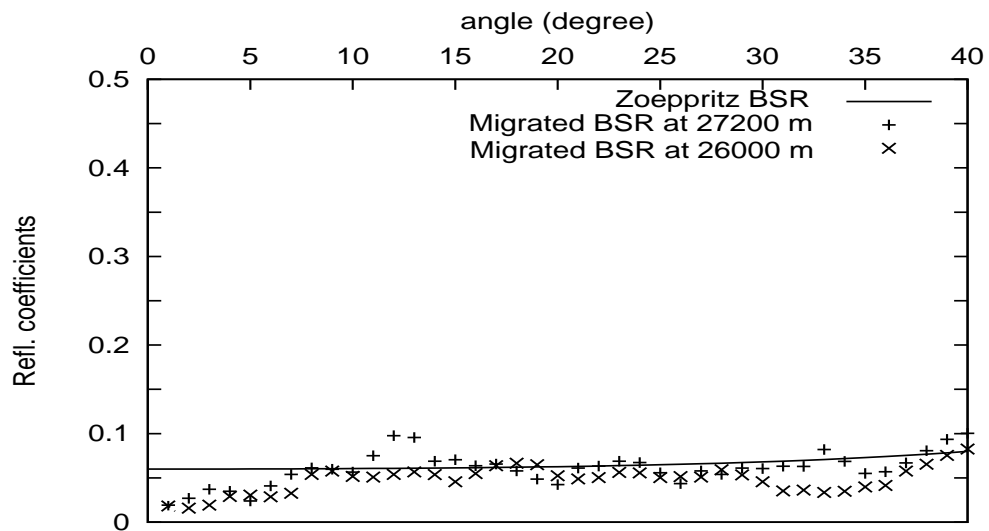


**Figure 5.22.** Comparison of the BSR AVA curve calculated using Zoeppritz' equations based on the increasing of P-wave velocities, which are illustrated in Figure 5.15c by a red-line, with the two AVA curves of the migrated angle-dependent reflectivity gather at lateral distance of 26000 m and 27200 m.

of 26000 m and 27200 m. Based on the agreement of these AVA curves, this condition favors the model of the gas hydrate sediments over the brine saturated sediments (Ecker et al., 1998).

In principle, the analysis of the second amplitude effects are the same as the first amplitude effects. The resulting models of the two amplitude effects are mostly similar, except there are decreasing S-wave velocities for the second amplitude effects and increasing S-wave velocities for the first amplitude effects. Two interpretations as described for the first amplitude effects are also possible for the second amplitude effects. The most important aspect that should be underlined in interpreting the second amplitude effects is that in fact it is more reasonable to assume that the constant amplitude trend is caused by interference effects, rather than patchy brine saturated sediments beneath the BSR. These interference effects may result from the complexity of the structures above and below the BSR, which are present in these regions.

## Chapter 6

# Conclusions and Perspectives

The presented applications to synthetic and real data sets demonstrate that the developed AP migration is able to preserve relative amplitude information and to construct angle-dependent reflectivity gathers as well as structural images. In general, the AP migration can be evaluated positively, particularly in producing correct relative amplitudes and comparable structural images.

This chapter summarizes the AP migration method in the context of strategy in implementing the CFP theory to the practical migration method, problems and limitations during handling of the migration process, and application possibilities. Finally, the recommendation for future work is presented at the end of this chapter.

### 6.1 Strategy of the AP Migration

The theoretical base of the AP migration, which is a modified CFP algorithm, has been successfully implemented to the flexible migration method. The strategy of the developed AP migration is mainly divided in two migration steps, which is formulated as a double complex cross-correlation process instead of conventional move-out correction.

The first complex cross-correlation is carried out to synthesize the response of a focused detector array by transforming the shot record into one trace that is positioned at the source position (focusing in detection). The second complex cross-correlation is carried out to synthesize the response of a focused source array by transforming the CFP gather (output of the first step) into reflectivity information (focusing in emission). The second step introduces the confocal version for producing angle-averaged reflectivity and the bifocal

version for producing angle-dependent reflectivity. The bifocal version involves a local slant-stack as part of the image-forming step.

Special attention is paid to preserve the amplitudes during the migration process by applying the weight function, which is performed in the two complex cross-correlation steps. The weight function is based on integrating the total downgoing energy at each point in the subsurface, which can be calculated at very little cost during the migration process. In the first complex cross-correlation process, the weight is carried out by multiplying the result of the cross-correlation (between a trace of the focusing operator and a trace of the shot gather) with the cosine of the incidence angle at the receiver. In the second complex cross-correlation process, the weight is carried out by dividing the zero-lag temporal cross-correlation between the response and the operator event with the zero-lag temporal auto-correlation of the operator event. Since the AP migration requires the focusing operator in the form of a seismogram, the parameters of the weight function are directly estimated from the focusing operator. In addition, the AP migration is designed as a separate program from the modeling algorithms in which both are compiled using a soft link (i.e., I/O SEG-Y files). Therefore, it may be implemented using the existing modeling algorithms.

The following are some advantages of the AP migration method:

- In spite of structural images, the AP migration method provides a complete process to recover angle-dependent reflectivity information, which are the basis to perform AVA analysis.
- The method offers a flexibility in accommodating any kind of migration operators (single-valued, multi-valued operator).
- The AP migration process is performed based on the double complex cross-correlation steps instead of the normal moveout correction. Thus, no explicit traveltimes information is required.
- The intermediate output may provide important information on errors in the migration operators as well as the underlying macro velocity model.

## 6.2 Focusing Operator

In connection with the modeling of focusing operators, the modified band limited Green's function algorithm is theoretically described and tested with numerical examples ranging from simple to complex models. Important aspects include the calculation of the correct multi-valued traveltimes, amplitudes, and phases of the seismic wave fields and the stability in handling complex velocity models. One of the advantages of the modeling algorithm is the estimation of multi-valued traveltime, amplitude, and phase information. This is an important point, particularly in migrating structurally complex velocity models. They provide multi-arrivals in the focusing operator, which also contain a large part of the energy. All events contribute considerably to the final image. In case of a single-valued operator, the calculated traveltime is a maximum amplitude traveltime. This operator provides enough energetic event than the first arrival. Another advantage is that no restrictions on the smoothness of the velocity model must be met. This follows from the fact that when a velocity estimation algorithm has produced a discontinuous model, it is better to use a discontinuous model rather than a smoothed model in calculating traveltime, amplitude, and phase. The other advantage is that the solution is found at every point in the subsurface and it is an estimate of the Green's function in the seismic frequency band, not the solution at very high frequency (Nichols, 1994).

On the other hand, this algorithm also has disadvantages. One of the disadvantages is that no explicit raypaths are calculated. They must be inferred from the Green's function. Another disadvantage is that the cost is 2 -10 times as expensive as the finite-difference solution to the eikonal equation (Nichols, 1994). The modeling algorithm also needs a finer output grid of traveltime, amplitude, and phase map in order to get a stable result, particularly for handling complex models.

Downward extrapolation, which is represented with a double complex cross-correlation step, is the central process in this AP migration scheme. It removes the propagation effects from the seismic measurements. These propagation effects are quantified in terms of one-way wave field propagators in the macro model (Berkhout, 1982). Consequently, the removal of the propagation effects is accomplished by applying the inverse of these wave field propagators to the seismic data. These inverse propagators are approximated by gen-

erating the focusing operators, downgoing and upgoing operator, for each grid-point in the subsurface.

The focusing operator is either parameterized or defined in the macro model. The model for the AP migration is a lossless, isotropic, and acoustic earth that generates only the primary reflections. Both focusing operators are generated by downward propagating the wave field from the surface. Referring to the amplitude (operator) index expressed in the weight function,  $A_{GM}$  and  $A_{SM}$ , the downward wave field propagation provides correct amplitudes. Note that the  $GM$  and  $SM$  index represent the wave field propagation from receiver and source, respectively, to the grid-point in the subsurface. Thereafter, the data are resorted to construct the upgoing operator. Thereby, the amplitude of the upgoing operator corresponds to the downgoing operator.

In addition, the full waveform of the focusing operator is constructed by convolving the three modeling outputs (traveltimes, amplitudes, and phases) with the Ricker wavelet. Analysis of the effect of wavelet frequency on the migration result indicates that the wavelet frequency that is used for constructing the seismogram operator should be equal or higher than the frequency content of the seismic data. Practically the appropriate wavelet frequency may be estimated by applying spectral analysis of the seismic data as time or depth variation. The use of low wavelet frequency should be avoided, because it will degrade the resolution of the migrated image.

### 6.3 Problems and Limitations

Several consequences to the amplitude-preserving migration are shown by this method. The most important aspects are summarized as follows:

- The AP migration is significantly more expensive and time consuming when it is performed in time domain, since the main migration process is performed as a double cross-correlation. As a solution, the cross-correlation process is carried out in the frequency domain. However, the cost of imaging is proportional to the number of shot gathers covered by the aperture, the offset within the shot gather, and the record length.



- The accuracy requirement on the focusing operator is higher. It is directly connected to the performance of the modeling algorithm as well as the accuracy of the velocity model used to construct the focusing operator. As a solution, the AP migration is compiled in soft link to the modeling algorithm, which permits to use any existing modeling algorithm.
- The problem in connection with the bifocal version of the AP migration is that the process is performed based on horizontal reflector approximation. Consequently, if the grid point is situated on a dipping reflector, the shift of amplitude distribution occurs in the migrated angle-dependent reflectivity gathers. To correct for this shift, the local dip-angle field is required. In this work, the local dip-angle field is estimated from the zero offset migrated section, which can be considered as a post processing step.
- The output of the bifocal version are rayparameter-dependent reflectivity gathers. In order to transform them to the angle-dependent reflectivity gathers, a postprocessing step must be applied. This postprocessing step requires a smoothed velocity field to avoid a dramatic shift of the event.
- For coarse migration grids, the positioning of reflectivity information around zero intercept time, resulting from a double complex cross-correlation step, to the migrated panel is performed based on a tapered window. The width of the window is defined based on the velocity field and the migration grid size. The smoothed velocity field is also required to produce a fine image. The tapering process may introduce interference effects at the lobe of wavelets. These effects can be avoided by defining a fine grid size, which means the imaging process will be more expensive. The fine grid size is more suitable for target oriented surveys.
- All required quantities for the amplitude preserving weight function are estimated from seismogram operators. Nevertheless, it will increase the cost of the migration process.
- The modeling algorithm is not designed to handle irregular source and receiver positions. Therefore, special seismic data acquisition (e.g., OBH and OBS data) should

be preprocessed in order to get the same level between source and receiver positions.

- Transmission loss effects are not taken into account in the focusing operators due to practical reasons. The downgoing and the upgoing operators are calculated based on the downgoing wave field propagation. In order to consider transmission loss effects, the upgoing operators must be estimated from the source at a depth point to the surface.

#### **6.4 Application of the AP Migration**

The main application of the developed method is to migrate surface reflection seismic data before stack. Based on the focusing formulation, the AP migration efficiently handles the sorted shot gather data set, which is available in format of the input data without preprocessing. This method is appropriate to the survey configuration where the number of shots is small compared to the offset. For target oriented surveys, the method can be used to image a target that is a subset of the whole volume without having to image everything above and below the target level. The flexibility of the method also permits the application to the seismic data collected with special technologies such as ocean bottom seismometer/hydrophone.

Migration examples on the simple generic models validate the AP migration and the application to the Marmousi model demonstrates its potential to image complex media. Furthermore, the application to the real seismic data set shows that the AP migration is able to provide significant information, which may be used as an input to AVA inversion. The presence of the BSR in seismic line OR89-02 has been clearly imaged and characterized with AVA attributes, which are estimated from the migrated angle-dependent reflectivity gather. In implementation, the AP migration can be incorporated as a tool package for reservoir characterization through the AVA analysis.

#### **6.5 Recommendation for Future Research**

Based on the advantages of the removal process, which is split in two focusing steps, the AP migration method can be integrated with the velocity analysis or the velocity model

estimation. This process can be obtained by applying the focusing operator updating in the intermediate step between the first focusing step and the second focusing step. In the course of this work, no attempt to implement the focusing operator updating has been made, as the aim of this method is not to produce the velocity model, but to recover correct relative amplitudes. Therefore, further development of the AP migration by involving the focusing operator updating will be an interesting theme.

Another aspect that should be given further attention is the modeling of focusing operators, which is calculated by using the band limited Green's function algorithm. So far the focusing operators are generated by one-way downward wave field propagation. In case the transmission loss factor is taken into account, the upgoing wave field propagation should be performed in the focusing operator modeling. This aspect needs further attention in order to arrive at a robust and practical procedure of the modeling program.

Finally, an extension to three-dimensional amplitude preserving migration should be made to handle three-dimensional seismic data.

## Bibliography

- Beacewell, R. N. (ed.) (1965). *The Fourier transform and its application*, New York, McGraw-Hill Book Co., Inc.
- Berkhout, A. J. (1982). *Seismic migration : Imaging of acoustic energy by wave field extrapolation*, Vol. 14A.
- Berkhout, A. J. (1992). Areal shot record technology, *Journal of Seismic Exploration* **1**: 251–264.
- Berkhout, A. J. (1997a). Pushing the limit of seismic imaging part I: Prestack migration in terms of double dynamic focusing, *Geophysics* **62**: 937–954.
- Berkhout, A. J. (1997b). Pushing the limit of seismic imaging part II: Integration of prestack migration velocity estimation, and AVO analysis, *Geophysics* **62**: 954–969.
- Bleistein, N., Cohen, J. K. and Hafin, F. G. (1987). Two and one-half dimensional born inversion with an arbitrary reference, *Geophysics* **52**: 26–36.
- Bohrmann, G., Trehu, A., Baldauf, J. and Richter, C. (2002). Drilling gas hydrates on hydrate ridge, Cascadia continental margin, *Technical report*, Ocean Drilling Program.
- Cambois, G. (1998). AVO attributes and noise: pitfalls of crossplotting, *SEG expanded abstracts*.
- Carcione, J. M. and Tinivella, U. (2000). Bottom-simulating reflectors: Seismic velocities and avo effects, *Geophysics* **65**: 54–67.
- Castagna, J. P. and Backus, M. M. (eds) (1993). *Offset-dependent reflectivity - Theory and Practice of AVO analysis*, Vol. 8, Society of Exploration Geophysicist, Tulsa.

- de Bruin, C. G. M., Wapenaar, C. P. A. and Berkhout, A. J. (1990). Angle dependent reflectivity by means of prestack migration, *Geophysics* **55**: 1223–1234.
- Ecker, C. (2001). *Seismic characterization of methane hydrate structures*, PhD thesis, Stanford University, Stanford.
- Ecker, C., Dvorkin, J. and Nur, A. (1998). Sediments with gas hydrates: Internal structure from seismic avo, *Geophysics* **63**: 1659–1669.
- Flueh, E. R. and Fisher, M. A. (eds) (1996). *Cruise Report SO 108 ORWELL*, Vol. 49, GEOMAR.
- Geoltrain, S. and Brac, J. (1993). Can we image complex structure with first-arrival traveltimes?, *Geophysics* **58**: 564–575.
- Gray, S. H. (1997). True-amplitude seismic migration: A comparison of three approaches, *Geophysics* **62**: 929–936.
- Hanitzsch, C., Schleicher, J. and Hubral, P. (1994). True amplitude migration of 2d synthetic data, *Geophysical Prospecting* **42**: 445–462.
- Hoffmann, H. J. (1995). *Objektoriente Analyse und migration diffrakter Wellenfelder unter Verwendung der Strahlenmethode und der edge wave theory*, PhD thesis, Kiel University, Kiel.
- Hubral, P. (2001). True love for true amplitudes, 1970-1980, *European Association of Geoscientists and Engineers Perspective* pp. 67–69.
- Hubral, P., Tygel, M. and Zien, H. (1991). Three-dimensional true-amplitude zero-offset migration, *Geophysics* **56**: 18–26.
- Hyndman, R. and Davis, E. (1992). A mechanism for the formation of methane hydrate and seafloor bottom simulating reflectors by vertical fluid expulsion, *J. Geophysical Research* **97**: 6683–6698.
- Jones E., J., W. (1999). *Marine Geophysics*, John–Wiley and Sons, New York.
- Kessinger, W. (2002). Overview of seismic exploration. Documentation accompanying Overview of Seismic exploration.  
**URL:** [http://walter.kessinger.com/work/seisx\\_introduction.html](http://walter.kessinger.com/work/seisx_introduction.html)

- Klaeschen, D., Kopf, A., Arsenault, M. and Bialas, J. (eds) (2001). *Cruise Report SO 150 HYDGAS*, GEOMAR.
- LeBras, R. and Clayton, R. (1988). An iterative inversion of back scattered acoustic wave, *Geophysics* **53**: 501–508.
- MacKay, M. E. (1992). Landward vergence and oblique structural trends in the Oregon margin accretionary prism: Implication and effect on fluid flow, *Earth and Planetary Science Letters* **109**: 477–491.
- Nichols, D. (1994). *Imaging complex structures using band limited Green's function*, PhD thesis, Stanford University, Stanford.
- Ostrander, W. J. (1984). Plane-wave reflection coefficients for gas sand at normal angles of incidence, *Geophysics* **49**: 1637–1649.
- Rabbel, W. (1987). *Seismische Erkundung oberflaechennaher Stoerzonen: strahlentheoretische Grundlagen und Feldbeispiele*, PhD thesis, University of Kiel, Kiel.
- Ricker, N. (1940). The form and nature of seismic wavelets and the structure of seismograms, *Geophysics* **5**: 348–366.
- Shipley, T. H., Houston, M. H., Buffer, R. T., Shaub, F. J., McMillen, K. J., Ladd, J. W. and Worzel, J. L. (1979). Seismic evidence of widespread possible gas hydrate horizons on continental slopes and rises, *American Association of Petroleum Geologists Bulletin* **63**: 2204–2213.
- Shuey, R. T. (1985). A simplification of the Zoeppritz equations, *Geophysics* **50**: 609–614.
- Taner, M. T., Koehler, F. and Sheriff, R. E. (1979). Complex seismic trace analysis, *Geophysics* **44**: 1041–1063.
- Tarantola, A. (1984). Inversion of seismic data in the acoustic approximation, *Geophysics* **49**: 1256–1266.
- Trehu, A. M. and Flueh, E. R. (2001). Estimating the thickness of the free gas zone beneath Hydrate Ridge, Oregon continental margin, from seismic velocities and attenuation, *Geophysical Research* **106**: 2035–2045.

- Trehu, A. M., Torres, M. E., More, G. F., Suess, E. and Bohrmann, G. (1999). Temporal and spatial evolution of a gas hydrate-bearing accretionary ridge on the Oregon continental margin, *Geology* **27**: 939–942.
- van Barneveld, I. B. (1998). *Multivalued focusing operators*, Master's thesis, Delft University of Technology, Netherlands.
- van Trier, J. and Symes, W. W. (1991). Upwind finite-difference calculation of traveltimes, *Geophysics* **58**: 812–821.
- Červény, V. and Soares, J. E. P. (1992). Fresnel volume ray tracing, *Geophysics* **57**: 902–915.
- Versteeg, R. (1993). Sensitivity of prestack depth migration to the velocity model, *Geophysics* **58**: 873–882.
- Vidale, J. (1988). Finite-difference calculation of traveltimes, *Bull. Seism. Soc. Am.* **78**: 2062–2076.
- Wapenaar, C. P. A. and Grimbergen, J. L. T. (1996). Reciprocity theorems for one-way wavefields, *Geophy. J. Int.* **127**: 177–196.
- Yilmaz, O. (1992). *Seismic Data Processing*, Vol. 5, Society of Exploration Geophysicists, Tulsa.
- Yuan, T., Spence, G. D. and Hyndman, R. D. (1994). Seismic velocities and inferred porosities in the accretionary wedge sediments at the Cascadia margin, *Geophysics. Rest.* **99**: 4413–4427.

## Appendix A

### The Fourier Transform

In order to speed up the computation during the migration process, the input data set and the focusing operator are transformed from time domain to the frequency domain. It is clear that the convolution and cross-correlation theorem describes the most important relationship between the time and frequency domains. A convolution operation in the time domain is equivalent to a multiplication operation in the frequency domain. This multiplication operation reduces the computation time. Therefore, the cross-correlation process in the AP migration method are performed in the frequency domain. This appendix describes the theory of the Fourier transform.

The Fourier integral is defined by the expression

$$H(f) = \int_{-\infty}^{\infty} h(t)e^{-j2\pi ft} dt \quad (\text{A.1})$$

where  $H(f)$  defines the Fourier transform of  $h(t)$ , if the integral exists for every value of the parameter  $f$ . In general, the Fourier transform is a complex quantity:

$$H(f) = R(f) + jI(f) = |H(f)|e^{j\theta(f)} \quad (\text{A.2})$$

Here  $R(f)$  is the real part of the Fourier transform,  $I(f)$  is the imaginary part of the Fourier transform.  $|H(f)|$  is the amplitude or Fourier spectrum of  $h(t)$  and is given by

$$|H(f)| = \sqrt{R^2(f) + I^2(f)} \quad (\text{A.3})$$

and  $\theta(f)$  is the phase of the Fourier transform and is given by



$$\theta(f) = \tan^{-1} \left[ \frac{I(f)}{R^2(f)} \right] \quad (\text{A.4})$$

The inverse Fourier transform is defined as

$$h(t) = \int_{-\infty}^{\infty} H(f) e^{j2\pi ft} dt \quad (\text{A.5})$$

Equation (A.5) allows the determination of a function of time from its Fourier transform. If the functions  $h(t)$  and  $H(f)$  are related by equation (B.1) and (A.5), the two functions are termed a Fourier transform pair and the relationship is indicated by:

$$h(t) \iff H(f) \quad (\text{A.6})$$

## Appendix B

### The Ricker Wavelet

The construction of the focusing operators used for the AP migration is carried out by convolving the three outputs of band limited Green's function (traveltimes, amplitude, and phase) with a Ricker wavelet. This appendix describes the concept of a Ricker wavelet. Ricker wavelets are ideal pulse shapes often used in seismic data displays. The seismic data is usually filtered so that the recorded pulses are transformed to the ideal Ricker wavelet shape. A sharp wavelet increases the resolution of the seismic display but requires a broad range of frequencies. A broad Ricker wavelet is composed of only a narrow range of frequencies. In the time domain, a zero phase Ricker wavelet with its peak at  $t=0$  is given by (Ricker, 1940):

$$w(t) = A_i[1 - 2(\pi v_m t)^2]e^{-(\pi v_m t)^2} \quad (\text{B.1})$$

Here  $A_i$  is the peak of the wavelet and  $v_m$  is the maximum frequency of the amplitude spectrum of the wavelet (central frequency). The central frequency is an important parameter, because of the special properties of this type of wavelet. Its behavior in the time and the frequency domain are completely determined by the central frequency. Figure B.1 shows the Ricker wavelet with a central frequency of 25 Hz.

Again, to speed up the construction of the focusing operators, the convolution process is performed in the frequency domain. The convolution theorem describes the most important relationship between the time and frequency domains. A convolution operation in the time domain is equivalent to a multiplication operation in the frequency domain.

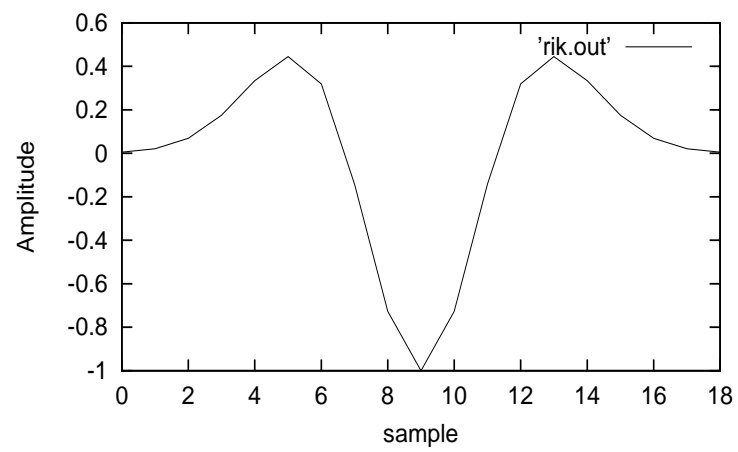


**Figure B.1.** The Ricker wavelet with a central frequency of 25 Hz.

## Appendix C

### Processing of Complex Seismic Trace

In the migration process, the AP migration treats the input data (seismic trace) as a complex seismic trace. The use of the complex trace is needed to reconstitute the shape of the source pulse. This is the part of phase shift compensation to the migration result. Moreover, the use of the complex trace provides migrated complex reflection coefficients (the real, the imaginary, and the envelope). The envelope proves that the position reflector is correctly imaged whereas the real part only is used for interpretation.

The following is a detailed description of the complex seismic trace. The basic definition of complex trace is

$$F(t) = f(t) + jf^*(t). \quad (\text{C.1})$$

Here,  $f(t)$  is a seismic trace, it is a real part of an analytical signal or complex trace.  $f^*(t)$  is the conjugate or imaginary part, which is uniquely determinable from  $f(t)$ . The imaginary component can be obtained by a Hilbert transformation that changes cosine into sine according to Taner et al. (1979) as:

$$h(t) * \cos\theta(t) = \sin\theta(t) \quad (\text{C.2})$$

where  $h(t)$  is the Hilbert transform operator. The real trace can be expressed in terms of time dependent amplitude  $A(t)$  and time dependent phase  $\theta(t)$  as:

$$f(t) = A(t)\cos\theta(t) \quad (\text{C.3})$$

and the imaginary trace then is

$$f(t) = A(t)\sin\theta(t) \quad (\text{C.4})$$

so the complex trace is

$$F(t) = f(t) + f^*(t) = A(t)e^{j\theta(t)} \quad (\text{C.5})$$

If  $f(t)$  and  $f^*(t)$  are known, the quantities called seismic attributes, reflection strength ( $A(t)$ ), instantaneous phase ( $\theta(t)$ ) and instantaneous frequency ( $\omega(t)$ ) can be obtained (Beacewell, 1965).

$$\begin{aligned} A(t) &= [f^2(t) + f^{*2}(t)]^{1/2} = |F(t)| \\ \theta(t) &= \tan^{-1} f^*(t)/f(t) \\ \frac{d\theta(t)}{dt} &= \omega(t) \end{aligned} \quad (\text{C.6})$$

### C.1 The Quadrature Trace

The quadrature or conjugate trace can be calculated from the real trace or vice versa by using the Hilbert transform in the digital convolution form as (Taner et al., 1979)

$$\begin{aligned} f^*(t) &= \frac{1}{\pi} \sum_{n=-\infty}^{\infty} f(t - n\Delta t) \frac{1 - e^{j\pi n}}{n} \quad n \neq 0 \\ f^*(t) &= \frac{2}{\pi} \sum_{n=-\infty}^{\infty} f(t - n\Delta t) \frac{\sin^2(\pi n/2)}{n} \quad n \neq 0 \end{aligned} \quad (\text{C.7})$$

Here,  $\Delta t$  is the sample interval. The inverse convolution is merely negative.

$$f(t) = \frac{2}{\pi} \sum_{n=-\infty}^{\infty} f^*(t - n\Delta t) \frac{\sin^2(\pi n/2)}{n} \quad n \neq 0 \quad (\text{C.8})$$

### C.2 Cross-correlation

The cross-correlation of two analytic traces,  $F_1(t)$  and  $F_2(t)$ , is

$$z(\tau) = \int_{-\infty}^{\infty} F_1(t) \overline{F_2(t + \tau)} dt \iff F_2(f) \overline{F_1(f)} \quad (\text{C.9})$$

Here the overline indicates the complex conjugate.

## Appendix D

# Radon Transform

In the bifocal version of the AP migration, the grid point's rayparameter-dependent reflection coefficients are obtained by Radon transforming or locally slant-stacking the double cross-correlation output (multitrace output) at zero intercept time, which is shown in Figure 4.2d. In addition, the rayparameter domain is transformed to the angle domain based on the interval velocity at each grid point. This appendix briefly discuss the concept of the Radon transform.

The Radon transform (RT) is a mathematical technique developed by J. Radon in 1917 that transforms map events from time-space domain to the tau-rayparameter ( $\tau-p$ ) domain. This transformation is also called the slant stack, because it describes the stacking along lines under different angles in the time-spacing recording. The local slant-stack is performed firstly by applying a linear moveout (LMO) correction to the multitrace output as follows (Yilmaz, 1992):

$$\tau = t - px \tag{D.1}$$

where  $p$  is the rayparameter,  $x$  is the offset,  $t$  is two way travelttime, and  $\tau$  is the linearly moveout time. After LMO, a reflection event with slope  $p$  on input data is flat. Next, the data are summed over the offset axis to obtain:

$$S(p, \tau) = \sum_x P(x, \tau + px) \tag{D.2}$$

Here,  $S(p, \tau)$  represents wave propagation with rayparameter of horizontal slowness

$$p = \frac{\sin \phi(z)}{v(z)} \quad (\text{D.3})$$

where  $\phi(z)$  is the propagation angle and  $v(z)$  is the interval velocity at depth  $z$ .

By repeating the LMO for various values of  $p$  and performing the staking, the complete slant-stack gather or  $p$  gather, which consists of all dip components in the original data, is constructed. Note that the resulting  $p$ -gather represents rayparameter-dependent reflection coefficients for one grid-point in the subsurface. Thereafter, the amplitudes of this  $p$ -gather around zero intercept time is positioned in the corresponding grid-point's depth in the rayparameter-dependent reflection coefficients gather. Repeating the same procedure for all grid-points in the same a lateral distance, the complete rayparameter-dependent reflection coefficients gather of that lateral distance is constructed.

In this work, the parameters involved in slant-stack processing are defined as follows:

- The number of rayparameter ( $n_p$ ) is equal to the number of trace input ( $n_x$ ). This parameter selection provides a good result.
- The rayparameter range ( $p_{min}, p_{max}$ ) is consistent with marine CMP data in the symmetric spread,  $p_{min} = (-1/1500)s/m$ ,  $p_{max} = (1/1500)s/m$ .
- The rayparameter increment is defined as  $(p_{max} - p_{min})/n_x$ .



## ACKNOWLEDGEMENTS

I owe much help, support, and inspiration of many people for realizing this dissertation. I would like to use this page to thank all those people who gave the contribution in completing this dissertation.

- First of all, I am especially grateful to Prof. Dr. Ernst Flueh as first supervisor who encouraged my effort from the beginning and developed my confidence to finish this work.
- I wish to express my sincere appreciation and gratitude to Dr. Dirk Klaeschen as second supervisor, who guided this work and helped whenever I was in need. He has provided for insightful discussion, collaboration, and excellent technical assistance.
- I appreciate the contribution given by Prof. Dr. Wolfgang Rabbel as second referee. I acknowledge his correction and suggestion for improving this dissertation.
- Special thanks to Dr. Heidrun Kopp, who provided proofreading during the writing of this dissertation. She showed immense tolerance and patience in reading and giving correction on the writing.
- I also thank Prof. Jason Phipps Morgan and Prof. Timothy Reston as head of Marine Geodynamics department. They have provided for an optimum working environment at the Institute.
- The discussions and cooperations with all of my colleagues have contributed substantially to this work. In particular I must thank to Arnim Berhorst, Joerg Petersen, Cord Papenberg, Joerg Bialas, Thomas Leythae, Cesar Ranero, Frank Lohmann, Anne Krabbenhoeft, Monika Bereitzke, Mathias Zilmer, Frederik Tilman, Silke Schenck, Willi Weinrebe, Ruediger Kunze, Gerd Mach, Martin Kordowski, Apweiler, and many others.
- I acknowledge the financial support from Deutscher Akademischer Austauschdienst (DAAD) and the research facilities from Research Center for Marine Geosciences (GEOMAR).

- I am grateful to Dave Nichols for the band limited Green's function method and to the Institute Français du Pétrole for the Marmousi data set. I am also grateful to Seismic Unix and SEP open source software, which are helpful for the purpose of the image display.
- Finally, I would like to express my deepest gratitude for the constant support and understanding that I received from my daughter Amanda Rifqa, my wife Marida Yulita and my parents during the past years.

## Curriculum Vitae

Name : Abd Haris

Date of Birth : September 21, 1970

Place of Birth : Pematang, Indonesia

Sex : Male

Nationality : Indonesia

Marital Status : Married, One Daughter

Office Address : GEOMAR (Research Center for Marine Geosciences) Wischhoff Strasse 1-3 Kiel, 24148  
Phone:341-6002337, Fax:341-6002292

Home Address : Augustenstrasse 32, Kiel, 24143  
Phone:341-673935

Email : aharis@geomar.de

1976 - 1982 : Elementary School, Pematang, Indonesia

1982 - 1985 : Junior High School, Pematang, Indonesia

1985 - 1988 : Senior High School, Pematang, Indonesia

1988 - 1992 : Under Graduate Program at Department of Physics, University of Indonesia, Jakarta, Indonesia

1993 - 1995 : Graduate Program at Department of Physics, University of Indonesia, Jakarta, Indonesia

1996 - 1999 : Research Assistant at Department of Geophysics, University of Indonesia

1997 - 1999 : Seismic Consultant (Data Quality Control), ARCO Oil Company, West Irian, Indonesia.

Since Dec. 1999 : Doctorate Program at GEOMAR, University of Kiel, Kiel, Germany